

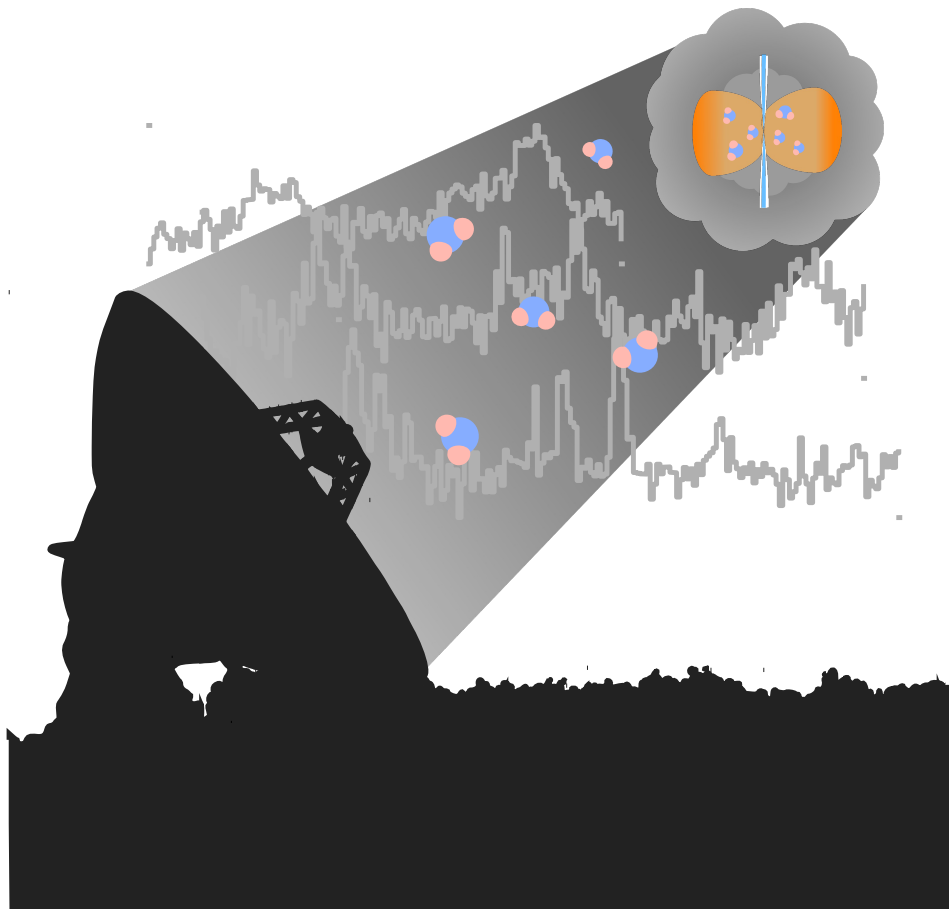


Ph.D.-Afhandling

Magnus Vilhelm Persson

Observations of Warm Water in Young Solar-System Analogs

Origin, abundances and deuterium fractionation



Vejleder: Jes Kristian Jørgensen

Afleveret den: 05/04/13

OBSERVATIONS OF WARM WATER IN
YOUNG SOLAR-SYSTEM ANALOGS

Origin, abundances and deuterium fractionation

A Dissertation Submitted in Partial Fulfillment of the
Requirements for the Degree of Philosophiæ Doctor.

Author:
Magnus Vilhelm Persson

Supervisor:
Associate Professor
Jes Kristian Jørgensen

PhD School of The Faculty of Science
Copenhagen University

Title : Observations of Warm Water in Young Solar-System Analogs – Origin, abundances and deuterium fractionation

Submitted : 2013-04-05

Author : Magnus Vilhelm Persson

Academic advisor : Associate Professor Jes Kristian Jørgensen

Department : Centre for Star and Planet Formation (StarPlan), Natural History Museum of Denmark, Copenhagen University

Subject description : Low-mass stars form when gravitationally unstable clouds of gas and dust collapse under their own weight. After several millions of years, planets have emerged around the newborn star. In our solar system, at least one planet harbors life and its surface is covered in water. Most of this water was formed early in the protostellar evolution, before the collapse of the cloud. Following the trail of water through the different stages of star formation is an integral task in astronomy and astrochemistry.
The aim of this thesis is to investigate the origin of warm water emission lines in deeply-embedded low-mass protostars. The relative abundances of different isotopologues of water can be used to infer the amount of processing that water goes through before being incorporated into comets and asteroids. The amount of water relative to other species can shed light on their inter-dependence.

Thesis committee : Associate Professor Uffe Gråe Jørgensen (Chair), Professor Paola Caselli and Doctor Mario Tafalla

Pentru soția mea
For my wife

Acknowledgments

I would like to express my deep gratitude to associate professor Jes Kristian Jørgensen, my research supervisor, for his patient guidance, useful critiques of this research work and for encouraging learning and independence in my work. I would also like to especially thank Johan Lindberg, for his friendship, advice and assistance throughout my time as a PhD student. My grateful thanks are also extended to Susanne Wampfler for her comments and help on the early draft of the thesis. I thank Søren Frimann, Julie Maria Lykke for their help with the Danish translation of the abstract. I thank all my colleagues at the Centre for Star and Planet Formation in Copenhagen: Odysseas Dionatos, Audrey Coutens, Christian Brinch, Suzanne Bisschop, Lene Bentzen and the rest of the members.

I also wish to thank professor Ewine van Dishoeck for her comments and help on all of the articles, and for her irresistible offer to come and work with her in Leiden after this PhD thesis. I am grateful to the IRAM staff, in particular Arancha Castro-Carrizo and Chin Shin Chang, for their help with the observations and reduction of much of the data in this thesis.

Finally, I wish to thank my family for their unhesitating support and encouragement. I feel especially grateful to my wife for coming with me on this journey.

Abstract

English

In star formation, water is an essential molecule. It affects the oxygen based chemistry, the physical conditions and energy balance in the protostellar envelope, and it is associated with the emergence of life as we know it. Ground based observations of water are hampered by the high amount of water vapor in Earth's atmosphere. Many of the lines that are observable from the ground are masing in star forming regions, making it hard to deduce abundances. The few lines that are observable, and shown not be masing are isotopologues, like HDO and D₂O, making the estimates of the main isotopologue form of water difficult. A solution to this has been to send up space based observatories, which observe outside of the atmosphere free from disturbances. Because of the small telescope sizes, these observations are of low resolution, making it hard to separate the different source components of the water emission. An alternative is to target H₂¹⁸O that can be observed toward protostars from the ground at high resolution, and is not masing in protostars under the conditions found in typical star forming regions. This isotopologue has the potential of revealing the spatial distribution of water in protostars.

In this thesis observations of the H₂¹⁸O, and HDO isotopologues are presented toward four sources in a small survey conducted with several interferometric telescopes. H₂¹⁸O is compared to the other molecules detected, i.e. CH₃OCH₃ (dimethyl ether), C₂H₅CN (ethyl cyanide) and SO₂ (sulfur dioxide). The amount of warm water is deduced and its origin is observationally constrained. With both isotopologues observed, the HDO/H₂O ratio is deduced. This ratio is then compared to other sources, e.g., comets and the Earth's ocean, to gain understanding of the origin of the water in our own solar system. The emission line fluxes are modeled with radiative transfer tools and compared to other results of water abundances in the same source.

The observed water emission, both H₂¹⁸O and HDO is compact for all observed sources and traces the emission on $R \approx 150$ AU scales or less. In one source the water is seen in absorption, with a inverse P-Cygni spectral profile - an indication of infalling motions. The similar line characteristics of water and the other detected molecules in the frequency band, together with the absorption toward one source, shows that these water lines are not masing. Under the assumption of local thermal equilibrium (LTE) and a excitation temperature derived from two observed HDO lines toward one source, abundances are derived, and a corresponding HDO/H₂O ratio. This method gives a partially model independent estimate of the amount of water deuterium fractionation in protostars. From non-LTE radiative transfer modeling of spherically symmetric models we show that while the HDO line is becoming marginally optically thick, the H₂¹⁸O line is optically thin. The modeling results are useful to assess the validity of LTE and optical thickness. However, for deriving fractional abundances, the LTE approximation and

modeling gives results that agree within the uncertainties. The other molecules detected in the observations of the H_2^{18}O show similar line widths to water. The abundances of dimethyl ether (CH_3OCH_3) and sulfur dioxide (SO_2) in relation to water (H_2O) are roughly equal between the individual sources. The ethyl cyanide ($\text{C}_2\text{H}_5\text{CN}$) on the other hand, is not. This indicates that similar chemical processes are at work for dimethyl ether, sulfur dioxide and water.

Danish

Vand er et vigtigt molekyle i stjernedannelse. Det påvirker iltbaseret kemi, de fysiske forhold og energibalancen i protostjernens envelope og, det er forbundet med fremkomsten af liv, som vi kender det. Jordbaserede observationer af vand hæmmes af den store mængde af vanddamp i Jordens atmosfære. Mange af de linjer, som er observerbare fra Jorden, er masing i stjernedannende områder, hvilket gør det svært at udlede tætheden. De få emissionslinjer som er observerbare, og som ikke maser, er isotopologer, f.eks. HDO og D_2O , hvilket gør estimater af den vigtigste isotopolog af vand vanskelig. En løsning på dette har været at opsende rumbaserede teleskoper, så man undgår atmosfæriske forstyrrelser. Den begrænsede størrelse af disse teleskoper medfører at observationerne er af lav opløsning hvilket gør det svært at separere de forskellige komponenter i vandets emission. Alternativt kan man observere H_2^{18}O i høj opløsning fra Jorden, da denne isotopolog ikke maser i protostjerner under de betingelser, der typisk findes i stjernedannende regioner. Dermed har H_2^{18}O potentiale til at afsløre den rumlige fordeling af vand i protostjerner.

I denne afhandling præsenteres observationer af H_2^{18}O og HDO isotopologer i fire kilder i en lille undersøgelse foretaget med flere forskellige interferometriske teleskoper. H_2^{18}O er sammenlignet med de andre detekterede molekyler, dvs CH_3OCH_3 (dimetyleter), $\text{C}_2\text{H}_5\text{CN}$ (etylcyanid) og SO_2 (svovldioxid). Mængden af varmt vand udledes og dens oprindelse er begrænset gennem observationer. HDO/ H_2O -forholdet kan udledes med begge isotopologer observeret. Dette forhold bliver så sammenlignet med andre kilder, f.eks. kometer i vores Solsystem og Jorden, for at opnå forståelse af oprindelsen af vandet i vores eget Solsystem. Intensiteter af de observerede linjer er modelleret med værktøjer for strålingstransport og bliver sammenlignet med andre resultater af vandmængder i den samme kilde.

Den observerede vand-emission, både H_2^{18}O og HDO er kompakt for alle observerede kilder og kan spore emission på $R \approx 150$ AU skalaer eller mindre. I en kilde ses vandet i absorption med en invers P-Cygni spektralprofil - et tegn på indfaldende bevægelser. De tilsvarende linjekarakteristika af vand og de andre detekterede molekyler i frekvensbåndet, sammen med absorption mod den ene kilde viser, at disse vandlinjer ikke maser. Under antagelse af lokal termisk ligevægt (LTE) og en eksitationstemperatur udledt fra to observerede HDO linjer mod en kilde, afledes både mængderne og et tilsvarende HDO/ H_2O -forhold. Denne metode giver en delvis modeluafhængig vurdering af mæng-

den af vand-deuterium fraktionering i protostjerner. Fra ikke-LTE strålingstransport af sfærisk symmetriske modeller viser vi, at mens HDO-linjen bliver marginalt optisk tyk, er H_2^{18}O -linjen optisk tynd. Modelresultaterne er nyttige til at vurdere gyldigheden af LTE og optisk tykkelse.

Men for udledning af den fraktionelle mængde giver LTE-antagelsen og modelleringen resultater, der stemmer overens indenfor usikkerheden. De andre observerede molekyler udover H_2^{18}O udviser lignende linjetykkelser som vand. Mængderne af dimetyleter (CH_3OCH_3) og svovldioxid (SO_2) i forhold til vand (H_2O) er sammenlignelige mellem de enkelte kilder - i modsætning til etylcyanid ($\text{C}_2\text{H}_5\text{CN}$), som ikke er. Dette indikerer, at tilsvarende kemiske processer påvirker dimetyleter, svovldioxid og vand.

CONTENTS

Acknowledgments	I
Abstract	II
English	II
Danish	III
Figures	IX
Tables	IX

INTRODUCTION

1 Scientific Background	3
1.1 Low-mass star formation	3
1.1.1 Introduction	3
The collapse	4
The protostar and its disk	5
The bipolar jet/outflow	6
The later stages	6
1.2 Water and star formation	7
1.2.1 The role of water in star-formation	9
1.2.2 Water formation	10
Low temperature gas phase chemistry	10
Grain surface formation	10
High temperature gas phase chemistry	13
Excitation	13
1.2.3 Observations	13
1.2.4 Deuteration	15
1.3 This thesis	16
2 Methods	19
2.1 Radio interferometric observations	19
2.1.1 Observations	20
2.1.2 Telescope arrays	22

CONTENTS

2.1.3	Calibration	24
2.1.4	Imaging	25
2.1.5	Analysis	26
2.2	Line radiative transfer modeling	27
2.2.1	General	27
2.2.2	Radiative transfer in theory	28
2.2.3	Escape probability	31
2.2.4	Local thermal equilibrium	32
2.2.5	Random walk and lambda iteration	32
3	The Research	35
3.1	List of publications	35
3.2	Results and Conclusions	35
3.2.1	Paper I	35
3.2.2	Paper II	36
3.2.3	Paper III	37
3.3	Outlook	38

PUBLICATIONS

Subarcsecond resolution observations of warm water in three protostars	43	
4.4	Introduction	43
4.5	Observations	45
4.6	Results	46
4.7	Analysis and discussion	50
4.7.1	Water on small scales	50
4.7.2	Water associated with the outflow in IRAS2A	51
4.7.3	Constraints on geometry and dynamics	52
4.7.4	Non-masing origin of H ₂ ¹⁸ O emission	54
4.7.5	Column densities and abundances determinations	54
	Water column density and mass	54
	Other molecules	55
	Effect of excitation temperature	56
4.7.6	Formation of molecules in the protostellar environment	58
4.8	Summary and Outlook	59
4.9	Tables	60
Warm water deuterium fractionation in IRAS 16293-2422	63	
4.10	Introduction	63
4.11	Observations	64

4.12	Results	65
4.13	Discussion	67
	4.13.1 Spectra and integrated intensity	67
	4.13.2 Temperature and deuteration of water vapor	67
4.14	Tables	70
The water deuterium fractionation on solar-system scales in three deeply-embedded low-mass protostars		71
4.15	Introduction	72
4.16	Observations	73
4.17	Results	74
4.18	Analysis	75
	4.18.1 Spectra and maps	75
	4.18.2 Column densities, excitation temperature and the HDO/H ₂ O ratio	78
	4.18.3 Radiative transfer modeling	78
4.19	Discussion and Conclusions	80
4.20	Summary and Outlook	80
4.21	Tables	82

List of Figures

1.1	The different stages of low-mass star formation	8
1.2	Overview over the different water formation routes.	11
1.3	Contributions of three different channels to water formation.	12
1.4	Atmospheric transmission curve at PdBI	14
2.1	Schematic drawing of a two element interferometer.	21
2.2	The ALMA telescope at the Chajnantor plateau.	23
2.3	The Plateau de Bure Interferometer	23
4.1	H ₂ ¹⁸ O spectra for IRAS2A, IRAS4A-NW and IRAS4B	47
4.2	Integrated intensity and velocity maps for the water lines in IRAS2A and IRAS4A	48
4.3	Positions of the lines relative to the continuum peak.	48
4.4	H ₂ ¹⁸ O continuum subtracted channel map for IRAS2A	51
4.5	IRAS2A off-position spectra	52
4.6	Schematic drawing of a disk dominated by inward motions rather than rotation in different observation geometries	53
4.7	Gas phase water fraction and the column density ratios	56
4.8	Ratio between molecules and water, and the column densities, both as a function of temperature	57
4.9	Ratio between CH ₃ OCH ₃ and C ₂ H ₅ CN in IRAS2A	58
4.10	Spectra of the targeted water lines toward IRAS 16293-2422.	66
4.11	Integrated intensity maps for the targeted water lines toward IRAS 16293-2422	67
4.12	Continuum subtracted spectra of the H ₂ ¹⁸ O 3 _{1,3} – 2 _{2,0} and HDO 3 _{1,2} – 2 _{2,1} lines toward the three sources.	76
4.13	Continuum subtracted spectra of the HDO 3 _{1,2} – 2 _{2,1} and 2 _{1,1} – 2 _{1,2} lines toward IRAS2A.	76
4.14	Integrated intensity maps for the HDO 3 _{1,1} – 3 _{3,1} and H ₂ ¹⁸ O 3 _{1,3} – 2 _{2,1} lines.	77
4.15	Integrated intensity maps for the 3 _{1,2} – 2 _{2,1} and 2 _{1,1} – 2 _{1,2} transition of HDO toward IRAS2A.	77
4.16	The variation of the water deuterium fractionation (HDO/H ₂ O) as a function of excitation temperature.	79

4.17	Values of the HDO/H ₂ O ratio, for different objects.	81
------	--	----

List of Tables

4.1	Parameters from the observations.	46
4.2	Parameters from the continuum fitting.	46
4.3	Parameters for the lines	49
4.4	Derived properties of the detected species	55
4.5	Tabulated data for the different lines detected from JPL and CDMS. . .	60
4.6	Position and FWHM of the detected lines	61
4.7	Parameters from fits to the integrated maps and spectra.	68
4.8	Parameters from the molecular line catalogs for the observed lines . . .	70
4.11	Results from fits to the spectra and the (u,v) -plane.	75
4.12	The HDO/H ₂ O abundance ratios for different objects.	82
4.13	Molecular data for the different lines.	83

LIST OF TABLES

INTRODUCTION

Scientific Background

1.1 Low-mass star formation

Clouds in the interstellar medium collapse to form stars and in the process a protoplanetary disk is formed. Water is formed in cold denser regions in the interstellar medium (ISM). It is an integral part of the chemical and physical evolution of the forming stars (see e.g., van Dishoeck & Blake 1998; van Dishoeck et al. 2011). Material, including this water, is transported from the circumstellar envelope to the disk, where planets are later formed (e.g., Visser et al. 2009, 2011). Also, water present in smaller solar system bodies, i.e., comets and asteroids, is thought to have been a source for Earth's water reservoir, delivered in the early solar system (Delsemme 1992, 1998). On Earth, water is necessary for the emergence and continuation of life as we know it. Thus studying the evolution of water, and its isotopologues during the entire star- and planet-forming process is an important task for the understanding of our own origins. To be able to understand these mechanisms and processes we must first look at the current star formation paradigm. In this section, the current idealized scenario of low-mass ($< 2 M_{\odot}$) star formation is presented.

1.1.1 Introduction

The typical particle density in the interstellar medium (ISM) is very low, on the order of 1 particle per cubic centimeter. This is much lower density than the best artificial vacuum created in laboratories on Earth. Even so, the ISM plays a pivotal role in the chemical evolution of our Galaxy. The ISM is where the star and planet formation takes place in the universe, at the same time the constituents of the ISM is the left over material from previous generations of stars.

The ISM consists mostly of gas (99% of mass), with small amounts (1%) of silicate and carbonaceous dust grains. The most abundant element in the ISM gas is hydrogen,

the second is helium with about 9.5% that of hydrogen. After this the abundances of elements relative to hydrogen drops (Przybilla et al. 2008, and references therein). The abundances of oxygen and carbon are both on the order of several 0.01%. Nitrogen, magnesium, silicon and iron are even lower, around 0.006% and below. As a consequence of these abundances the most common molecular species are H₂, CO, H₂O, and O₂. There is a large molecular diversity in the ISM, in fact, around 180 molecular species¹ have been detected in the interstellar medium or circumstellar shells.

Most of the molecular gas is localized to giant molecular clouds (GMC). Density fluctuations create a complex internal structure of GMCs. Recent observations with the *Herschel* Space Observatory have revealed a strong filamentary structure of molecular clouds (Arzoumanian et al. 2011; Peretto et al. 2012). The density fluctuations are attributed to supersonic turbulence, magnetic fields and thermal instabilities. Some of the resulting density fluctuations exceed the critical mass and density of gravitational stability, these are called pre-stellar cores. The gravitationally unstable pre-stellar core will start to collapse to form a star.

The collapse

A spherical slowly rotating cloud core of gas and dust with a mass exceeding the critical mass collapses under its own weight. However, when magnetic fields are present, the collapse can be delayed due to the process of ambipolar diffusion (e.g., Shu et al. 1987). The collapsing cloud core is cold ($T \sim 10$ K), and optically thin at millimeter wavelengths, allowing radiation to escape and temperature to stay constant. The collapse proceeds almost isothermal and on a free-fall timescale (i.e., $t_{ff} = \sqrt{3\pi/(32G\rho)}$). While the radiative cooling continues, the contraction continues. When the density reaches about $10^{-13} - 10^{-12}$ g cm⁻³, the central regions become optically thick. At this point the collapse proceeds adiabatically, with increasing temperature as an effect (Bate 2010). At densities of $\sim 10^{-9} - 10^{-8}$ g cm⁻³ the collapsing core becomes thermally supported and the “first core” is formed (Larson 1969). For high rotation rates, this core is oblate enough to be classified as a disk, thus forming the disk before the star (Bate 1998; Machida et al. 2010). While material falls on to this newly formed hydrostatic core, the temperature continues to increase. When the temperature reaches ~ 2000 K, molecular hydrogen (H₂) dissociates absorbing much of the thermal energy, which causes a break in the pressure equilibrium. This initiates a second collapse that continues until all the molecular hydrogen is dissociated. When this stops a second hydrostatic core is formed. This core continues to contract on a Kelvin-Helmholtz timescale², radiating half of the thermal energy away. This second core is part of what is generally referred to as a protostar. Recently, three-dimensional radiative magnetohydrodynamic simulations of protostellar collapse concur with these evolutionary steps (Tomida et al. 2013).

¹e.g., <http://www.astro.uni-koeln.de/cdms/molecules>

²The time it takes to radiate away the thermal energy gained from contraction

A deeply-embedded protostar is only visible in the infrared and at longer wavelengths (basically undetectable $\lambda \lesssim 10 \mu\text{m}$). Most of the mass is contained in the envelope, rather than in the central protostar. Its spectral energy distribution (SED) is characterized by the cold dust in the ambient envelope which peaks at roughly $100 \mu\text{m}$. This type of source is generally classified as a Class 0 source. Most of the structure can be approximately described with a spherically symmetric envelope (on scales $> 300 \text{ AU}$). The inner regions ($< 100 \text{ AU}$) are heated by the central source to temperatures in excess of 100 K , and densities in the range 10^{7-8} cm^{-3} . This region, where the ices have evaporated and complex organic molecules are detected are referred to as “hot corino” (hot core for massive stars) (Bottinelli et al. 2004b). Many of the released molecules were trapped in the ice during the formation of the ice layers on the dust grains, and some are precursor molecules to even more complex species (e.g., Jørgensen et al. 2012). A substantial part of the accretion is believed to take place during this stage. Furthermore, observations show highly collimated outflows in these sources, and the envelope extends to tens of thousands of AU.

During the main collapse(s) described above the cloud increases its rotational speed due to conservation of angular momentum. Eventually, this rotation causes a flattened circumstellar disk to form (Terebey et al. 1984). The typical early solar-like protostar has a mass of about $10^{-2} M_{\odot}$, thus it has to gain most of its mass after the main collapse. This happens with the help of the circumstellar disk, it accretes material from the surrounding envelope and transports it to the central protostar. While the cloud core contracts by a factor of about one million in radius during the collapse, the angular momentum has to be transported away for the cloud to continue to contract. This is accomplished by the ejection of a bipolar outflow. The exact launching mechanism is still unknown. Observations show that protostars have complex, non-spherically symmetric structures, even on larger ($> 1000 \text{ AU}$) scales (Tobin et al. 2010). However, the general, approximated star formation scenario is that of a collapsing spherical cloud core. The general evolution of a low-mass protostar is shown in Figure 1.1.

The protostar and its disk

Throughout the protostellar phase, the circumstellar disk accretes matter from the surrounding envelope and transports it to the central protostar. When matter reaches the inner edge of the disk, closest to the protostar, parts of it accretes onto the protostar and the rest is ejected, perpendicular to the disk, along open magnetic field lines, carrying away angular momentum. This ejection of matter forms a bipolar outflow. The disk has a large radial extent in the Class I/II stages (several hundreds, perhaps thousands of AU) and the scale-height increases rapidly with radius. The disk decreases in mass, extent and height with time. Most of the mass is accreted over periods of less than about 500 000 years (Class 0+I stage, Evans et al. 2009). However, the exact details of the accretion process are still unknown. The increasing mass of the disk accreted from

the surrounding envelope is thought to initiate a periodic disk instability that causes a short burst of high accretion rate onto the central protostar, and a period of extra high luminosity of the whole system. This is believed to be the rare FU Orionis events that has been observed in a handful of sources (Hartmann & Kenyon 1996).

After the main collapse phase has passed, the SED is composed of thermal dust emission from the disk peaking at about 8 μm , and the emission from the cold dust in the large envelope remains. This phase is referred to as the Class I stage. How early the disk is formed, what physical structure this early disk has and when the planet formation process starts is not currently known.

It is during the early protostellar stages that the initial conditions for the later astrochemical evolution are established (Visser et al. 2009). Because of poor resolution, and the optically opaque structures, the physical parameters on 100 AU scales are poorly constrained in general, but high resolution millimeter wavelength observations reveal the beginning complexity (Class 0/I, Jørgensen et al. 2005; Chiang et al. 2008). Since it is on the smaller scales that much of the chemistry takes place, it is important to constrain the physical structure of these regions.

The bipolar jet/outflow

The bipolar jet transfers energy to the surrounding medium, entrains material and accelerates it to speeds of tens of kilometers per second. For low-mass sources the jet can have a launching speed ranging between 10 – 100 km s^{-1} , sizes extending between 0.1 – 1 pc and typical momentum rates of $10^{-5} M_{\odot} \text{ km s}^{-1} \text{ yr}^{-1}$ (see e.g., Tafalla et al. (2004) and the review by Arce et al. (2007)). Interactions between the jet and the surrounding medium induce supersonic shock fronts. The cooling regions of these radiate strongly. These regions were first discovered in the optical as Herbig-Haro objects (Herbig 1951; Haro 1952).

While some of the matter is expelled in the outflow some of it is accreted onto the central object. Most of the accretion takes place in the early stages, i.e., Class 0/I, and the collimation of the outflow decreases during the protostellar evolution and aids in the dispersion of the envelope. The connection between the outflow and the accretion was first made from an observed correlation between forbidden line luminosities with accretion luminosities derived from the optical or UV emission in excess of photospheric radiation (optical/UV continuum veiling, Hartigan et al. 1995).

The later stages

When large parts of the thick surrounding envelope have dissipated, the central source can be observed at shorter wavelengths, i.e. infrared. The outflow and accretion continues at a diminished rate, with a flatter disk. While the final mass of the protostar has been accreted, its contraction continues, releasing gravitational energy. The SED is

characterized by a black-body spectrum peaking at a few μm , with thermal dust emission from mid-IR to submm wavelengths from the protoplanetary disk. The protostellar system is now in the Class II stage of its evolution. Stars in these stages of formation are sometimes referred to as T Tauri stars, from the prototype object discovered in the Taurus star forming region. The disk is likely in vertical hydrostatic equilibrium at all radii, which was first described by (Shakura & Sunyaev 1973) with an increase of the disk scale height as a power law - more commonly referred to as a flared disk. Dust growth through various processes causes the larger dust grains to decouple from the gas and settle toward the mid-plane of the disk (Beckwith & Sargent 1991; Miyake & Nakagawa 1993; D'Alessio et al. 1999, 2001). The growth continues, through processes not fully understood, and planetesimals, and eventually planets are formed. Over time the surrounding envelope is dispersed; the material is entrained in the outflow, accreted to the star/disk system or photo-evaporated by the increasingly more massive protostar. Grain growth and the dissipation of the disk causes the disk component of the SED to decrease in intensity, and the disk to become optically thin. The object is now referred to as a Class III source. With time the disk is cleared of gas through various processes. The removal of gas from the upper layer of the disk via photo-ionization has been shown to clear the disk over time scales of 10^5 years. Protoplanetary disks have median lifetime of about 3 million years from formation, and all disks have dissipated after 10 Myr (Williams & Cieza 2011).

As the protostellar system evolves, the SED changes so that first the envelope contribution decreases and the central protostar and the accretion disk takes over and finally a stellar black body is left. When the density and temperature in the central source increase enough so that nuclear burning is initiated, roughly a few million years into the pre-main sequence phase, the star settles as a main sequence star. It is in this stage that our own Sun currently is in.

1.2 Water and star formation

Water is an essential molecule for the emergence and continuation of life as we know it on Earth. Even so, there are many unanswered questions about water and its relation to star and planet formation. How common is water in the different protostellar structures and how can water be transported to the surface of a planet? What is the relation between water and other molecular species? Where and how does water form during the protostellar evolution? These are all questions that astronomy and astrochemistry are trying to answer, not only for the understanding of our own origins but also for probing the star and planet formation process as a whole. For a recent general review on the topic of astrochemistry see Caselli & Ceccarelli (2012).

Clouds in the interstellar medium collapse to form stars and in the process a protostellar disk is formed. Material is transported from the circumstellar envelope

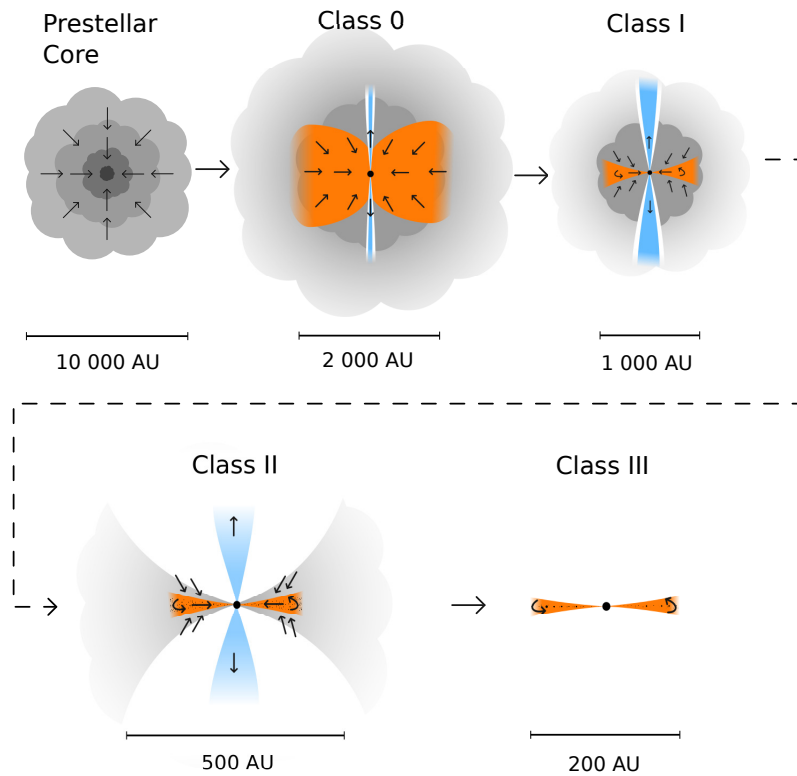


Figure 1.1: Schematic drawing of the different stages of low-mass star formation.

through the disk, where planets are later formed, to the star forming in the center (e.g., Visser et al. 2009). Water is thought to form early in the protostellar evolution, and frozen onto the surface of dust grains (Tielens & Hagen 1982). These grains are present when the solar system bodies are formed from the material in the protoplanetary disk. During massive episodes of bombardment, water incorporated in smaller solar system bodies, i.e., comets and asteroids, is thought to have brought a fraction of Earth’s water reservoir (see review by Morbidelli et al. 2000). However, how much water did smaller solar system bodies bring to Earth? How much chemical processing did water go through before and after being incorporated into comets and asteroids? What other species does the water ice contain? In addition to these questions, water fills many other important functions in regions of star and planet formation. To answer these questions and to understand the observations, we must first look at how we believe water is formed, its excitation and its deuteration patterns. This section gives an introduction to this, and also gives an overview of the latest results from observations and modeling

of water in star forming regions.

1.2.1 The role of water in star-formation

After H_2 , carbon monoxide is generally the most abundant gaseous molecule, with a fractional abundance of 10^{-4} . Significantly larger species than CO can have fractional abundances down to 10^{-11} (in relation to H_2). The fraction of oxygen contained in water in star forming regions can often approach and sometime surpass that of CO ($\sim 20\%$ Whittet 1993), especially in ices and shocked regions (e.g., Herczeg et al. 2012; Pontoppidan et al. 2004). Indeed water is a significant reservoir of oxygen in protostellar envelopes and it has an impact on the chemistry of all other oxygen-containing species (see e.g., Herbst & van Dishoeck 2009; Charnley et al. 1992, and references therein). Water is also one of the major coolants in warm gas, thus influencing the energy balance (Ceccarelli et al. 1996; Neufeld & Kaufman 1993). Liseau et al. (1996) found that water contributed about $\sim 30\%$ of the cooling in the low-mass Herbig-Haro (outflow shock) object HH54, a value confirmed in other shocks (e.g., Nisini et al. 2010). Other important coolants include O, OH and CO. Water is the major constituent of the ice in the grain mantles in cold outer regions of protostellar envelopes and dense mid-planes of circumstellar disks (Gibb et al. 2004; Boogert et al. 2008). After water, CO_2 (20%) and CO (5%) are the most abundant. With water ice on the grain surface, the sticking between grains increases, aiding the process of grain growth in cold regions.

Water has an evaporation temperature of about 100 K (Fraser et al. 2001). While the gas phase water abundance is low in cold and quiescent regions (e.g., Bergin & Snell 2002), it jumps several orders of magnitude in regions of increased temperature (e.g., Harwit et al. 1998). This property of water makes it an excellent probe of the warmer structures in the early protostellar evolution. The inner regions of protostars is an environment where the temperatures is raised above 100 K. It is this evaporated, warm, gas that is relevant for this thesis work. In the ice mantles, water has the possibility to trap other molecules, such as methanol (CH_3OH), ammonia (NH_3) and possibly dimethyl ether (CH_3OCH_3), which are released back into the gas when the water evaporates (Gibb et al. 2004; Boogert et al. 2008). Thus studying where, when and how the water forms and is released into gas phase, and its related species is also important for the understanding of other molecules seen in the protostellar environment.

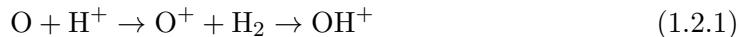
The deuterated isotopologues of water (HDO and D_2O) are important for studying the temperature history of the cloud and the conditions during the grain surface formation of water. The relation between the deuterated species and “normal” water (H_2O) and that measured in solar system bodies gives clues on the evolution during the entire star formation process. Comparing the ratio to what is seen in other sources, such as the Earth’s oceans and solar system bodies increases the understanding of the amount of processing of water that takes place during the evolution of the protostar.

1.2.2 Water formation

As described in Sect. 1.1.1, the different phases a forming star goes through during its formation creates many different environments, with varying temperature and density structures. Temperatures between 10 and 2000 K, densities of 10^4 to $> 10^{10} \text{ cm}^{-3}$ and gas-to-dust ratios significantly different from the ISM value of 100 are not uncommon throughout the evolution. Of course, the water and consequently the water related chemistry change with these conditions. While the presence of water in star forming regions has been confirmed by numerous observations (see Section 1.2.3), the chemical origin of water is not yet completely understood. For a short review on the water chemistry in star forming regions, see e.g., van Dishoeck et al. (2011).

Low temperature gas phase chemistry

Generally, neutral-neutral reactions have much larger activation energy barriers than those involving ions. They consequently are slow at the low temperatures seen in the early evolutionary stages of star formation. When an ion is involved in the reaction, the neutral species is polarized. Thus at low temperature it is possible to form H_2O through these kind of reactions. Two possible ion-molecule reaction routes to form H_2O starts with the formation of OH^+ (Dalgarno & Black 1976; Herbst & Klemperer 1973)



With OH^+ the chemistry moves toward water through a series of hydrogen atom transfer reactions (hydrogen atom abstractions).



The hydronium ion (H_3O^+) can, through dissociative recombination with an electron form either H_2O or OH . At low temperature water is mainly destroyed by photo-dissociation through far-UV photons, and reactions with C^+ , H_3^+ , HCO^+ and other ions. This reaction network which includes pure gas-phase chemistry, and scales with cosmic-ionization rate has a steady state H_2O abundance at low temperatures of 10^{-7} relative to H_2 (e.g., Woodall et al. 2007).

Grain surface formation

Recent observations do not support the simple ion-molecule gas phase chemistry described above. Observations of O_2 in these cold environments show very low abundances (e.g., Bergin et al. 2000) contrary to what is needed for high yields from the gas phase

reaction network. Furthermore, observations of absorption lines at 3 μm of solid H_2O toward protostars derive abundances as high as 10^{-4} , relative to H_2 (e.g., Pontoppidan et al. 2004). These abundances are 3 – 4 orders of magnitude higher than what is expected from pure gas-phase chemistry. Therefore new advances have been made in the laboratory to investigate the feasibility and rates of the grain surface chemistry in producing water at low temperatures (e.g., Ioppolo et al. 2008, 2010). It was re-

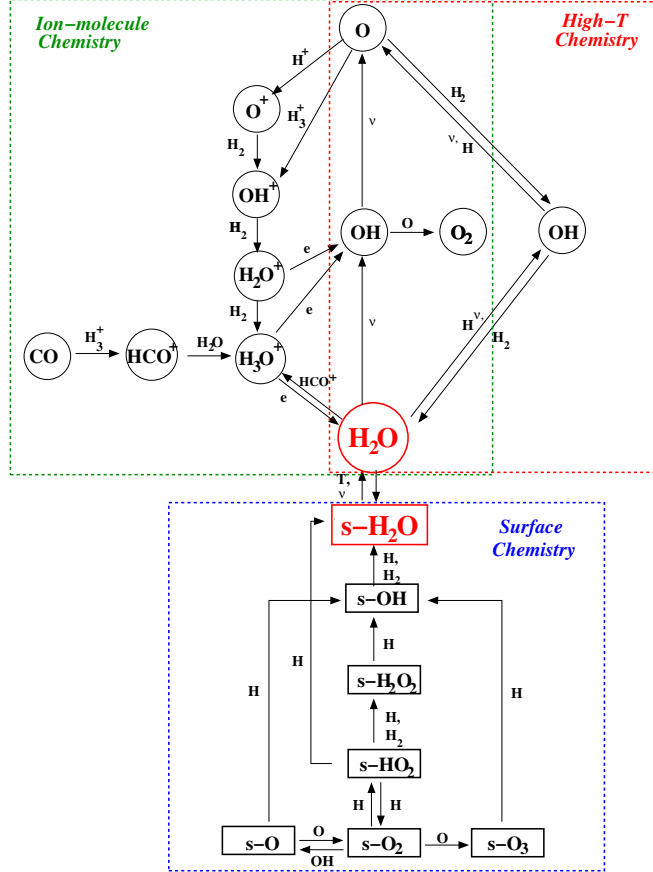


Figure 1.2: Overview over the different water formation routes in the low and high temperature gas phase, and the surface formation route. From van Dishoeck et al. (2011).

alized that grain surface reactions involving accreted O and H could also form water (Tielens & Hagen 1982). The surface formation of water becomes important when the visual extinction in the cloud becomes higher than $A_V \approx 5$ magnitudes. This happens before the cloud core starts the collapse (Whittet 2003) - as illustrated by the recent detection of water vapor toward the pre-stellar core L1544 with the *Herschel* Space Observatory (Caselli et al. 2012). To reach the high amount of water vapor observed in L1544 ($> 1.0 \times 10^{13} \text{ cm}^{-2}$), the working theory is that the icy mantles are irradiated by

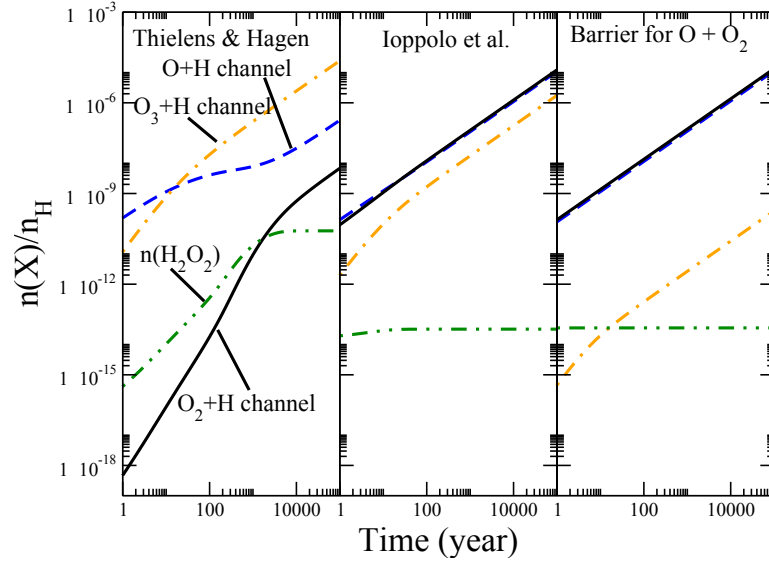


Figure 1.3: Contributions of three different channels to water formation. The right panel shows new results of the barrier for the $O + O_2$ reaction. Figure from Ioppolo et al. (2008).

far-UV photons produced by H_2 molecules that are struck by galactic cosmic rays, thus photo-evaporating the water in the ice into the gas phase. This, and other non-thermal processes to desorb the water ice formed through surface reactions, are covered in the overview by Hollenbach et al. (2009). The relevant routes for formation of water are shown in Figure 1.2.

As can be seen there are several routes for surface formation of water. In the original grain surface reaction network by Tielens & Hagen (1982) with three paths to water, the ozone route was assumed to be the most efficient. Ioppolo et al. (2008) showed that the path



is also important. The formation of H_2O_2 proceeds with a reaction barrier significantly lower than previously believed (see Figure 1.3). Furthermore, it was shown that the reaction barrier for the ozone route is higher. Thus, several routes of water surface formation have to be taken into account.

High temperature gas phase chemistry

When the grains containing the water ice formed in the early pre-stellar stages are heated above ~ 100 K, the H_2O evaporates into the gas phase (Fraser et al. 2001). With it other molecules trapped in the ice is also released. When the gas temperature reaches 230 K, whatever oxygen is left is efficiently driven into water through the following reactions (Charnley 1997).



These temperatures are reached within the few tens of AU close to the low-mass protostar, and in outflow shocks.

Excitation

Water is a complex species in terms of its excitation, it is an asymmetric top and the rotational spectra have to be fitted numerically. The water molecule has a set of rotational energy levels characterized by the quantum numbers $J_{K_A K_C}$. Furthermore, the energy levels are grouped into ortho ($K_A + K_C = \text{odd}$) and para ($K_A + K_C = \text{even}$) ladders because of nuclear spin statistics of the two hydrogen atoms. Ortho- and para- H_2 are the important collision partners, and at low J the cross section for collisions with ortho- H_2 are significantly larger than with para- H_2 . The main isotopologue of water has high line opacities, making it difficult to extract reliable abundances, thus other isotopologues have to be used. Furthermore, many of the transitions exhibit inverted populations to varying degrees, and in some cases the lines are masing. Examples of water lines that show maser emission toward star forming regions are the 22 and 183 GHz lines (Cernicharo et al. 1994; Szymczak et al. 2005; Elitzur 1992). All these properties makes water hard to analyze, e.g., when doing radiative transfer modeling extra care have to be taken to make sure that the models converge properly.

1.2.3 Observations

Ground based observations of water lines are limited by the large amounts of water vapor in the Earth's atmosphere that absorb many of the lines otherwise observable. The atmospheric transmission curve at Plateau de Bure Interferometer site is seen in Figure 1.4. The different lines show the transmission at varying degree of precipitable water vapor (PWV) in the atmosphere. The drops in the transmission is mainly because of water, and increasing the observation frequency and PWV will lower the transmission. For this reason, most observations of thermally excited water has come from space based observatories where the atmosphere is not an issue.

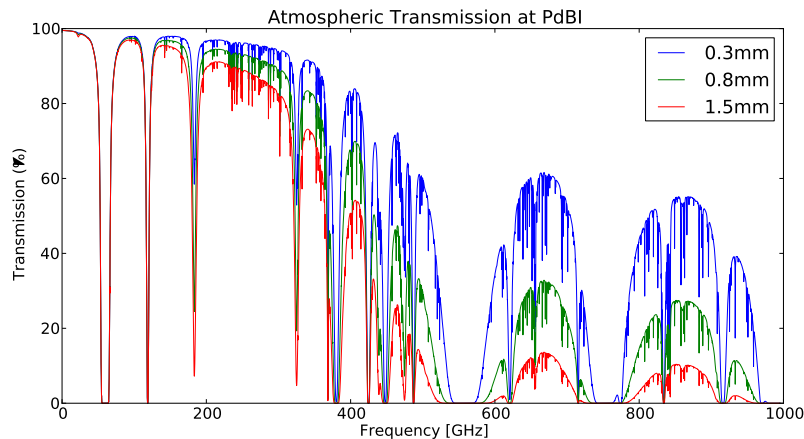


Figure 1.4: The atmospheric transmission for the Plateau de Bure Interferometer site at 2500 m altitude for 0.3, 0.8 and 1.5 mm of precipitable water vapor (PWV).

In the nineties, the *Infrared Space Observatory* (Kessler et al. 1996), operating in the mid- to far-IR, surveyed several protostellar outflows and protostars. The interpretation of the numerous detections of water emission (70% of the sources surveyed) in deeply-embedded low-mass protostars differed. Their origin were either the warm inner regions, where the ices evaporate (Ceccarelli et al. 1999), or in shocks associated with the outflow impacting the envelope (Nisini 2003). As also mentioned before, ISO managed to characterize the ice composition in star forming regions. After ISO, *SWAS* (Submillimeter Wave Astronomy Satellite Melnick et al. 2000) and *Odin* (Nordh et al. 2003) took over and, with its different frequency coverages, provided constraints on the abundance and kinematics of water in the cold outflow components (e.g., Bjerkeli et al. 2009). However, the spatial resolution of these early space telescopes were lacking, making them more sensitive to the large-scale emission in the outflow and extended envelope, and not the gas on smaller scales. The lack of resolution did not either make it possible to study any variations in abundances and intensities along the outflows.

In the field of star formation *Herschel* has brought a wealth of new results. Many of the breakthroughs were made in observations of large scale extended emission. The spectra of several deeply-embedded protostars show complex profiles that were traced to different parts of the protostellar structure (e.g., van Dishoeck et al. 2011; Kristensen et al. 2012). It was also discovered that the origin of water in shocks is likely different from what was previously thought. Tafalla et al. (2013) suggests that water traces the outflow gas at higher temperature, hundreds of kelvins. This means that the water abundance is lower in shocks. Recently the first detection of water vapor in a pre-stellar core was made by Caselli et al. (2012).

The few observable lines from the ground of water are usually masing (see Sect. 2.2.1).

Observations of water masers go back as far as 40 years (Cheung et al. 1969), and are routinely observed toward low-mass protostellar regions (Furuya et al. 2003; Cernicharo et al. 1994; Choi et al. 2012). While water masers are useful as signposts of star forming regions, they are variable in nature, and because of the inverted populations it is hard to deduce physical parameters (e.g., column density, Felli et al. 2007; Elitzur 1998). Water lines that are observable from the ground, and seen not to be masing, exist. The para- H_2^{18}O $3_{1,3} - 2_{2,0}$ line at 203.4 GHz has been observed toward star forming regions with high-mass protostars (Jacq et al. 1988; Gensheimer et al. 1996; van der Tak et al. 2006) and low-mass protostars (Jørgensen & van Dishoeck 2010b). Furthermore, several HDO lines exist, the $3_{1,3} - 3_{2,0}$ transition at 225.9 GHz and the $2_{1,1} - 2_{1,2}$ transition at 241.6 GHz are readily observed, and have been observed toward several low-mass protostars (e.g., Parise et al. 2005; Liu et al. 2011).

Furthermore Stark et al. (2004) observed several transitions of the stretching bands of OH and OD in water ice toward several pre-stellar cores. The double deuterated D_2O can also be observed in star forming regions; Butner et al. (2007) detected the fundamental transition $1_{1,0} - 1_{0,1}$ at 316.8 GHz toward the deeply embedded low-mass protostar IRAS 16293-2422 with the single dish telescope JCMT³. Water has been detected even earlier in the protostellar evolution when the temperature is so low that all the water is expected to be frozen onto the surface of the dust grains. Caselli et al. (2012) managed to detect the $1_{1,0} - 1_{0,1}$ transition of ortho- H_2O toward the pre-stellar core L1544. The emission line, showing an inverse P-Cygni profile (infall signature), can be explained if the water is being released into gas phase by far-UV photons. However, far-UV photons cannot penetrate deep into the protostellar envelope. This means that they are produced locally, probably by the excitation and de-excitation of galactic cosmic rays by H_2 molecules (Hollenbach et al. 2009).

1.2.4 Deuteration

The amount of deuteration in the water molecule is affected by the dominating formation mechanism. The deuterium fractionation in water is significantly lower than the deuteration in other species (e.g., Roberts et al. 2003; Cazaux et al. 2011; Taquet et al. 2013). Observational estimates toward objects in star forming regions support this (Gensheimer et al. 1996; Persson et al. 2007; Parise et al. 2005). The deuterium fractionation of water in comets and in the Earth's oceans ($\text{HDO}/\text{H}_2\text{O} = 3.113 \pm 0.002 \times 10^{-4}$, de Laeter et al. 2003) are often compared and used as an indicator of how much of Earth's water was delivered by comets. The $\text{HDO}/\text{H}_2\text{O}$ value in the protosolar nebula was measured by Geiss & Gloeckler (1998); Lellouch et al. (2001) to be 0.42×10^{-4} and in the local ISM it is determined to 0.4×10^{-4} (Prodanović et al. 2010a). Comparing the deuterium fractionation of water in protostars and these reservoirs has the poten-

³James Clerk Maxwell Telescope, on Hawaii

tial to shed light on the chemical evolution of water through all of the star formation stages. Unfortunately, determining the HDO/H₂O ratio in many of these reservoirs is not straightforward.

Up until recently, the HDO/H₂O ratio in comets was 6.4×10^{-4} (Jehin et al. 2009). All the comets that had been measured are long-period (> 200 years) comets believed to originate in the Oort cloud. This ratio is significantly above that of Earth's oceans, and based on this it was argued that only a fraction ($\leq 10\%$) of Earth's water could have come from comets (Morbidelli et al. 2000; Drake 2005). Then the Jupiter Family comet Hartley 2 (short period, Hartogh et al. 2011) and the Oort cloud comet Garrad (Bockelée-Morvan et al. 2012) were observed with the *Herschel* Space Observatory. The results showed a HDO/H₂O ratio of 3.2×10^{-4} for Hartley 2, and 4.12×10^{-4} , i.e., value significantly lower than previous estimates. The values are closer to that of Earth's oceans and implies that the analysis of how much of Earth's water was delivered by comets have to be revised.

In the warm gas of low-mass protostars, several attempts have been made, they range from values close to that of comets to a few percent (e.g., Stark et al. 2004; Parise et al. 2005; Liu et al. 2011). Most of the previous observations have used single dish, space based telescopes, mainly for the derivation of the H₂O abundance (see the next section). This results in large beam sizes, making it difficult to disentangle the large scale from the compact emission originating in the inner warm regions.

1.3 This thesis

The structure of warm ($T > 100$ K) inner ($R < 300$ AU) regions of deeply embedded low-mass protostars is not well constrained. Water that has been formed on the surface of dust grains in the cold shielded parts of early protostellar envelopes evaporate off the grains when the temperature exceeds 100 K. When frozen onto the dust grains, water locks up more complex (organic) molecules in its ice. These molecules are later released during the evaporation, water thus plays an integral part in the chemistry in these regions. Simple spherical, and more complex 3D models agree that the conditions for warm gas phase water are met in the inner regions. Resolved observations of this warm water in low-mass protostars are currently lacking, previous observations are of low resolution, probing large scales ($R > 10000$ AU) and usually from a multitude of telescopes with differing resolutions. This thesis presents high-resolution ($\sim 1''$), ground based observations of the H₂¹⁸O and HDO isotopologues of water toward several deeply-embedded (Class 0) low-mass protostars. The observations have the potential to shed light on the origin and abundance of the warm water emission lines seen in these sources.

The origin of Earth's water is unknown, observations and models do not agree fully. Usually the D/H ratio in water (HDO/H₂O) is compared between reservoirs

to deduce the source of Earth's water. Observations of comets and Earth's water indicate that some of the water was brought by impacting bodies in the early solar system. Observations exist for the protosolar nebula, and the local ISM, however, measurements of other stars that are currently forming disagree. Thus high resolution observations of water are needed to disentangle the different results.

The aim of the project is to constrain the origin and abundance of warm water in the inner regions of deeply-embedded low-mass protostars and deduce a HDO/H₂O ratio in the same region. Observations of both H₂¹⁸O and HDO have been made toward three sources in the NGC 1333 region (IRAS2A, IRAS4A and IRAS4B) and the prototypical low-mass protostellar binary IRAS 16293-2422 in ρ Ophiuchus. The other detected molecules can be compared to water, to assess their relation to the water that could have delivered them to the gas phase through evaporation. By measuring both H₂¹⁸O and HDO a HDO/H₂O ratio can be estimated.

Methods

Astronomers have a limited number of tools to analyze theories about the universe. The main tool is observations, high spatial and spectral resolution observations, with high sensitivity are generally sought after. To peer into the deep interior of the early stages of star formation we need to observe in the radio regime. As described previously, these objects emit at longer wavelengths roughly from 10 μm and a few cm. To attain high resolution, we connect several telescopes in what is called an interferometer. When the observations are done, radiative transfer modeling is a useful tool to interpret them. It can indicate if an observed line is becoming optically thick, given a physical parameter, and given the observed line flux it can derive the abundances of a certain molecule. In addition to this, non-LTE effects can be modeled and accounted for. It has the potential to differentiate between various source structures by comparing with the observed extended emission.

2.1 Radio interferometric observations

As mentioned above, in star formation, we need telescopes that observe at longer wavelengths to be able to peer into the deep interior of protostellar objects. The more conveniently located protostars are between 100 and 400 pc away. To observe the smaller scales (< 100 AU), needed to probe the region where water and complex organics are in gas phase, we need to at least have an angular resolution of about $1''$, or better. In the radio regime, and most other astronomical observations, the atmosphere plays a significant role in degrading the signal, thus high altitudes where there is less atmosphere to interfere are preferred locations for telescopes. This section gives an overview of how radio interferometric observations are conducted and what data analysis is done.

2.1.1 Observations

The resolution of an optical system is limited by diffraction, i.e., the effect that the finite aperture has on an incident wave. The resolution (in arcseconds) of a telescope is given by two things, the size (diameter) of the main aperture that collects the radiation (D m) and the frequency (ν GHz) or wavelength (λ mm) of the observed light

$$\theta \approx \frac{75440}{\nu D} \approx 252 \times \frac{\lambda}{D}. \quad (2.1.1)$$

The frequency that can be observed mainly depends on the transmission and typical conditions of the atmosphere at the location of the telescope and also on how smooth the surface of the reflector is. The reflecting surface of a telescope must be smooth to an accuracy of $1/\text{sth}$ of the wavelength that is being reflected. The early designs of single radio telescopes used in astronomical observations resulted in very low spatial resolutions (several degrees). It was quickly realized that many structures in the universe were smaller than the resolution achievable at the time. Today the typical resolution for single dish radio telescopes is roughly $10''$ or worse. For example, to get down to arcsecond resolution at a wavelength of 3 mm (100 GHz) the dish size needs to be larger than 750 m. The largest steerable radio telescopes today are about 100 m in diameter, and building dishes that are bigger than this is not technically feasible.

A more practical solution is to synthesize a large telescope by connecting many small (~ 10 m) telescopes together and placing them even further apart (up to several kilometers). Now the resolution is proportional to the distance between the telescopes. This type of instrument is called an interferometer. The simplest radio interferometer consists of two connected telescopes. The basic layout of this system is sketched in Figure 2.1. The antennae pair and the unique projected distance between them is referred to as a baseline. The emission that is detected and converted to an electrical signal at each telescope are multiplied and then integrated over a short time interval in what is referred to as the correlator. The radiation does not hit the telescopes at the same time, unless the source is exactly at zenith. To counteract this a time delay is added to the signal of the closest telescope.

The combined signal from the two telescopes is related to the sky brightness distribution, i.e. the structure of the emission seen from the source. This has the effect that the instantaneous observed combined signal is one component of the Fourier transform of the sky brightness distribution. The relationship, which is valid for partially coherent sources of radiation, is referred to as the van-Cittert-Zernicke theorem and was first discovered in the 1930's. The electronic output of each antenna and the correlator can be described in complex notation. To recover the phase and amplitude several other operations are carried out on the signals as well. Thus each telescope pair at a given baseline measures the amplitude and phase of one Fourier component, one visibility in the plane that is defined by the two coordinates u and v , commonly referred to

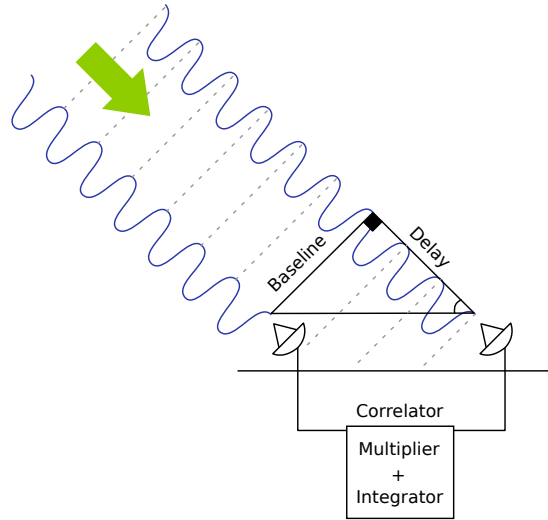


Figure 2.1: Schematic drawing of a two element interferometer.

as the (u, v) -plane. With many different baselines, and integrating when tracing the source over the sky, we acquire many Fourier components that describe the source. The (projected) baselines change as the telescopes track the source over the sky. Thus for each integration, and each telescope pair we get one Fourier component. Since the baseline is a unique vector, going from telescope 1 to 2, the negative baseline going from telescope 2 to 1 is also one point in the Fourier plane, basically the same but with the phase reversed.

Thus if we would have amplitude and phase information over the complete (u, v) -plane, we could recreate the true sky brightness distribution. The number of baselines for an interferometer with N_A antennae is given by $N_A(N_A - 1)$, including the reversed baseline in the counting. The amplitude and phase is recorded in slots of finite frequency width over a large frequency range in the correlator.

The number of slots, or channels, that needs to be correlated determines the frequency resolution. The spectral resolution is commonly given as

$$R_s = \frac{\lambda}{\Delta\lambda}. \quad (2.1.2)$$

In the infrared, some of the high resolution spectrographs can attain a resolution on the order of $R_s \sim 10^5$ (e.g., Ulrich Käuffl 2008). Since radio telescopes operate at longer wavelengths, it is easier to achieve higher spectral resolution, at 100 GHz the ALMA telescope (see below) will be able to observe at a spectral resolution as high as $R_s \sim 30 \times 10^6$ ¹. The correlation of all the spectral channels happens in real-time,

¹<http://almascience.eso.org/about-alma/alma-basics>

which puts constraints on the speed and capabilities of the electronics, bandwidth and computing power at the telescope.

The point sensitivity of an interferometer is given by

$$\Delta S = \frac{2k_B T_{\text{sys}}}{\eta_q \eta_a A \sqrt{N(N-1) \Delta\nu \Delta t}} = \frac{\mathcal{J} T_{\text{sys}}}{\eta_q \sqrt{N(N-1) \Delta\nu \Delta t}}, \quad (2.1.3)$$

where $\mathcal{J} = 2k_B/\eta_a A$ is the typical efficiency (Jy/K) for one antenna in the array, η_q the quantization efficiency (i.e., digital/analog conversion efficiency), A the area of each antenna, N the number of antennae, T_{sys} the instrumental noise (system temperature), $\Delta\nu$ the frequency resolution, and Δt the integration time.

2.1.2 Telescope arrays

In this thesis work, the three radio interferometric telescope arrays that have been used are the Atacama Large submm/Millimeter Array (ALMA), the Plateau de Bure Interferometer (PdBI) and the Submillimeter Array (SMA). In the section below, a short introduction to the general characteristics and capabilities of the telescopes is presented.

In the millimeter wavelength range, the most prominent radio interferometer is ALMA, the Atacama Large (sub)Millimeter Array. ALMA is the largest and most sensitive submm/mm telescope ever built. It is currently (2013) being constructed on the Chajnantor plateau in the Atacama desert in northern Chile at an altitude of 5 km (Andes mountains). When finished the 66 antennae (12 m diameter), with a maximum baseline of 16 km, will be able to attain sub-arcsecond ($\sim 0''.02$) resolution at a wavelength of 1 mm (i.e., ~ 300 GHz). It is a global partnership between Europe, North America, East Asia and the Republic of Chile. When finished and if all the receiver bands are built, it will cover frequencies from 31 GHz (Band 1) all the way up above 1 THz (Band 11). The 66 antennae will give a instantaneous uv-coverage (4290 baselines) and sensitivity enough for acquiring data in snap-shot mode, i.e., a significant reduction in per-source observation time.

The Plateau de Bure Interferometer (PdBI) is a six element interferometer in the French alps, at an altitude of 2550 meters. Each dish is 15 m in diameter, the four available receivers goes from 80 to 371 GHz and the maximum baseline is 760 m giving a resolution of $0''.3$ at 300 GHz/1 mm. The telescope is a collaboration between the French CNRS (Centre National de la Recherche Scientifique), German MPG (Max-Planck Gesellschaft) and the Spanish IGN (Instituto Geográfico Nacional). The array is currently being upgraded, and a seventh antenna will be added during 2013 as part of the Northern Extended Millimeter Array (NOEMA) project. When this project is completed it will, double the number of antennas, extend the East-West baseline to 1.6 km and increase the capabilities of the receiver bands. Since PdBI is located in Europe, it is one of the arrays available for observations of the northern hemisphere.



Figure 2.2: Picture showing the ALMA telescope currently under construction in the Chilean Andes. Credit: Clem & Adri Bacri-Normier (wingsforscience.com)/ESO.



Figure 2.3: The Plateau de Bure Interferometer at 2550 m altitude. Credit: IRAM

The Submillimeter Array (SMA) is a telescope array with 8 elements, each 6 m in diameter. It is located on Mauna Kea in Hawaii, at an altitude of 4080 meters. The receivers cover frequencies from 180 to 700 GHz. The maximum baseline is 508 m and the resulting maximum resolution is thus $0''.5$ at 300 GHz/1 mm. The SMA is a collaborative project of the Smithsonian Astrophysical Observatory (SAO) in the USA and the Academia Sinica Institute of Astronomy and Astrophysics (ASIAA) in Taiwan.

2.1.3 Calibration

In radio interferometry several instrumental and atmospheric effects need to be calibrated. In the electronics there are for example variable gains, pointing and focus of the telescopes and spectral response that need to be calibrated. The atmosphere introduces a time dependent phase shift and absorption that have to be corrected for. Some parameters are calibrated in real-time at the observatory, and some are calibrated afterwards.

The bandpass (amplitude and phase as a function of frequency) is calibrated by observations of a strong point source at the beginning of each project. Since the observed calibrator object is a point source, the phase is expected to be zero, and can thus be calibrated by fitting a polynomial to the phase as a function of frequency. The accuracy of the phase calibration affects the relative positional error of spectral features. Sources which are not point sources can be observed, but then there must exist an accurate model for the structure, which can be subtracted from the data and leave the atmospheric and other contributions. The bandpass amplitude with frequency is known for the observed calibrator, and is fitted in a similar manner. The solution to the bandpass is applied to the data. The amplitude calibration affects the ability to detect weak lines on a strong continuum.

The next step in the calibration procedure is to calibrate the phase and amplitude as a function of time. Several effects contribute to the variations of phase during the observations. Electronics, uncertainty in antenna positions and the atmosphere all cause variations in the phase with time. Some are short term variations, shorter than a minute and some are longer, up to 24 hours. To calibrate it, a point source is observed every few minutes. A function is fitted to the phase change with time, and applied to the data, if possible two calibrator sources are observed. For the really short variations, water vapor radiometers are usually used to apply a correction in real-time and later checked if it improves the data quality. Calibrating the amplitude with time is similar to the phase. It needs to be solved so that the efficiencies of each antenna can be derived, i.e., the temperature to flux conversion. By observing a point source, the temporal variation of the efficiencies can be solved and then applied to the data, just like the phase.

In the last step of the calibration, the absolute flux scale needs to be calibrated. Here all of the calibrators observed can be used for the solution. Each telescope efficiency

is calibrated to an absolute scale, by comparing the flux detected for the calibrators to their known flux. The absolute flux calibration is the dominating uncertainty in the finished dataset, with errors as high as 20%, but generally better for newer and upgraded facilities (e.g., PdBI, SMA, ALMA e.t.c.).

The calibrator sources needs to be nearby the target source to reduce slewing time and to make sure that similar atmospheric conditions apply. The calibrator source should also be of well defined structure, or a known point source. The bandpass calibrator should of course be as line-free, and have a flat spectrum if possible. Typical calibrators are planets, moons and quasars, all which are either of known structure or point sources. Quasar fluxes are known to be variable on the order of days, hence observatories monitor the change to be able to use them as calibrators.

After or during the calibration, the dataset is edited, and data that is of bad quality is removed or flagged (i.e., marked not to be used). When the calibration is done the continuum can be subtracted. The subtraction of continuum can be done either after the imaging, or directly in the (uv) -plane. The general approach is the same: find channels with no line emission, use those to form a continuum dataset and subtract this from the spectral cube. If done in the image plane, and the bandwidth is large, care has to be taken to account for the change in beam with frequency.

2.1.4 Imaging

The interferometer gives amplitude and phase information at a given time and baseline, this is one Fourier component of the source brightness. The point source response of the observations is the Fourier transform of a set of unity values at each observed (u, v) point, this is called the dirty beam. To image the observations, we need to perform Fourier transformations to the measured (u, v) points. Doing this is very computationally expensive, and therefor most uses a type of Fast Fourier Transform. For this to work, the data need to be interpolated on to a regularly spaced grid, and the spacing is chosen so that the synthesized beam is fully sampled (pixel size $\lesssim 1/3$ FWHM, Full Width at Half Maximum of the Gaussian beam). Once the FFT has been applied to the gridded data, an estimate of the sky brightness distribution is given, this map is called the dirty map. This is simply the true sky brightness convolved with the dirty beam, i.e., the point source response. This map usually have side lobes, i.e., areas where information is missing and other features that adds noise to the image. Techniques to perform deconvolution of the dirty map have been developed to improve the image quality. One example of such an algorithm is the CLEAN algorithm, it was first developed by Högbom (1974), with several variations proposed since then. The algorithm finds the highest value in the image and subtracts a small fraction of the point source convolved with the dirty beam, and the position and amplitude of the source is saved (a clean component). This finding and subtraction is repeated until residual is below a certain limit (e.g., RMS) or after a certain number of clean components have been recovered.

All the found components are then convolved with a Gaussian derived from a fit to the dirty beam, i.e., a clean beam and added up together with the residual cleaning map. The CLEAN algorithm assumes that the image is built up of point sources, thus it works less well for extended emission.

2.1.5 Analysis

The dataset after the deconvolution (e.i., CLEAN) has three dimensions, spatial coordinates (i.e., Right Ascension and Declination) and a spectral (velocity) axis. The intensity of each pixel is given in Jy beam^{-1} . In addition to doing analysis in the image plane, the data in the (u, v) -plane can also be analyzed.

The imaged data can be displayed and analyzed in various ways. However, the first step of the analysis is to estimate the noise. The root mean square (RMS) of the noise ($\text{RMS} = \sqrt{\langle M_{\text{noise}}^2 \rangle}$) gives an estimate of the error. When integrating the emission over several channels, the corresponding RMS, or sensitivity, is simply $\sigma = \sqrt{N} \times \text{RMS} \times \Delta\nu$. The variations in intensity along the spectral dimension in one pixel, the spectrum, is used to identify emission lines. After defining over which channels/frequencies an emission line is located, the image moments are calculated. Often a 1D Gaussian is fitted and the line is defined from the line center \pm the width of the line. The three first image moments are integrated intensity, velocity map and velocity dispersion map. The integrated intensity (zeroth order moment) is computed at the coordinate (α, δ) as

$$M_0 = I_{\text{TOT}}(\alpha, \delta) = \int_{i=x_1}^{x_2} I(\alpha, \delta, v_i) dv = \Delta v \sum_{i=x_1}^{x_2} I(\alpha, \delta, v_i) \quad (2.1.4)$$

where v_i is the coordinate along the third, velocity axis. The intensity weighted (velocity) map (first order moment) is

$$M_1 = \bar{v}(\alpha, \delta) = \frac{\sum_{i=x_1}^{x_2} v_i I(\alpha, \delta, v_i)}{\sum_{i=x_1}^{x_2} I(\alpha, \delta, v_i)} \quad (2.1.5)$$

and it shows if there are any velocity gradients when you compute it for the whole image. The intensity weighted dispersion map (second order moment)

$$I = \sigma_v(\alpha, \delta) = \sqrt{\frac{\sum_{i=x_1}^{x_2} I(\alpha, \delta, v_i) (v_i - \bar{v}(\alpha, \delta))^2}{\sum_{i=x_1}^{x_2} I(\alpha, \delta, v_i)}}. \quad (2.1.6)$$

It shows how the line width changes with position in the image. It is also possible to compare the location and spatial extent of emission lines with that of the continuum, this can yield insights into the origin of the emission.

To avoid the introduction of noise and errors that is related to the imaging (i.e. gridding, CLEANing e.t.c.), it is possible to fit simple source models directly in the (u, v) -plane (Gaussian, disk, torus, point etc.). A linear combination of several source models can be fitted as well, e.i., a binary system might be fitted with two point sources or two Gaussians. The integrated intensity (see above) can also be computed in the (u, v) -plane, and after fitting a Gaussian to the (u, v) -data the intensity is found.

2.2 Line radiative transfer modeling

With the observations finished, radiative transfer codes are usually employed to constrain the physical structure. Normally a density structure is input into a continuum radiative transfer solver. It computes the dust temperature self-consistently, given the stellar spectrum and the assumed density structure. The dust temperature, and density can then be input in to a line radiative transfer tool, given a molecular abundance. The line radiative transfer code will then compute the line fluxes that can be compared to the observations and the molecular abundance and or physical structure can be changed to fit the observations better. This is dependent on an a priori knowledge about the source structure.

This section provides a general overview of the fundamentals of line radiative transfer necessary for understanding the details of the papers in this thesis. The derivations and notation follow those of Rybicki & Lightman (2004).

2.2.1 General

Consider a system where molecules with a mean mass m move freely and interact with one another through elastic collisions where they exchange momentum and kinetic energy. The distribution of molecular speeds v (kinetic motion) at a temperature T_{kin} is described by the Maxwell-Boltzmann distribution

$$f(v) = \sqrt{\left(\frac{m}{2\pi k_{\text{B}} T_{\text{kin}}}\right)^3} 4\pi v^2 e^{(-mv^2/2k_{\text{B}} T_{\text{kin}})} \quad (2.2.1)$$

where k_{B} is the Boltzmann constant. The kinetic temperature here is the same that appears in the ideal gas law ($pV = RT$) to describe the temperature of a medium. The notion of molecules can be replaced by any type of particle in a system with the same premises.

In a two level system, the characteristic temperature that in thermodynamic equilibrium would produce the same population ratio is called excitation temperature (T_{ex}).

The ratio, i.e. the number of molecules in the upper energy level (u) in comparison to the number in a lower level (l), is described by the Boltzmann distribution

$$\frac{n_l}{n_u} = \frac{g_l}{g_u} e^{(h\nu/kT_{\text{ex}})} \quad (2.2.2)$$

where g_l is the statistical weight of the lower level and g_u for the upper, ν the frequency of the transition and h Planck's constant. The excitation temperature has no actual physical meaning except during thermodynamic equilibrium (when $T_{\text{ex}} = T_{\text{kin}}$). For a system with inverted levels, the excitation temperature is negative.

Radiation may be described by the Planck function

$$B_\nu(T_{\text{rad}}) = \frac{2h\nu^3}{c^2} \frac{1}{e^{(h\nu/k_B T_{\text{rad}})} - 1} \quad (2.2.3)$$

where c is the speed of light, and T_{rad} the radiation temperature. This is the temperature a black body of similar dimensions would have that radiated the same intensity at the same frequency.

When all of these different temperatures are the same, i.e., $T_{\text{kin}} = T_{\text{ex}} = T_{\text{rad}}$ we speak of thermodynamic equilibrium. The system can thus be described by one single temperature, and the different temperatures in the equations above can be replaced by this one single temperature T .

2.2.2 Radiative transfer in theory

A star like our Sun emits out roughly 10^{45} photons per second and following every photon's path in computer modeling is unpractical. Thus we need to develop theory and computer models that describe the important processes involved. The specific intensity I at frequency ν is defined as the radiation energy flowing through a surface per unit time per steradian in a specific frequency range as

$$I_\nu = \frac{dE}{d\nu dA dt d\Omega \cos\theta}. \quad (2.2.4)$$

Following this, I_ν stays constant in a medium that neither absorbs or emits radiation at the given frequency. With this definition we can add expressions for absorption and emission to compute a analytical intensity that depend on the physical structure. The fraction of emission that is absorbed in the volume element at position \vec{r} is denoted with the absorption coefficient $\alpha_\nu(\vec{r})$ and the emitted radiation at the same position with the emission coefficient $j_\nu(\vec{r})$. Here stimulated emission is included as a negative $\alpha_\nu(\vec{r})$. With this we can now describe what happens with radiation along a small distance ds as

$$\frac{dI_\nu}{ds} = -\alpha_\nu(\vec{r})I_\nu + j_\nu(\vec{r}). \quad (2.2.5)$$

Here the change in intensity I_ν along an incremental path element, ds is affected by absorption $\alpha_\nu I_\nu$ and emission j_ν . For convenience and clarity one often defines the optical depth as $\tau_\nu(s) = \int_0^s \alpha_\nu(s') ds'$ and the source function $S_\nu(\tau_\nu) = j_\nu(\vec{r})/\alpha_\nu(\vec{r})$ in which case the relation above becomes

$$\frac{dI_\nu}{d\tau_\nu} = -I_\nu + S_\nu(\tau_\nu). \quad (2.2.6)$$

This means that the change in intensity dI_ν along the optical depth $d\tau$ is the source function S_ν minus the specific intensity I_ν . The analytical solution to this equation is

$$I_\nu(\tau_\nu) = I_\nu(0) e^{-\tau_\nu} + \int_0^{\tau_\nu} S_\nu(\tau'_\nu) e^{-(\tau_\nu - \tau'_\nu)} d\tau'_\nu. \quad (2.2.7)$$

The first term, $I_\nu(0) e^{-\tau_\nu}$, describes how much of the background radiation that is able to get through the media, and the second term $\int_0^{\tau_\nu} S_\nu(\tau'_\nu) e^{-(\tau_\nu - \tau'_\nu)} d\tau'_\nu$ how much of the radiation emitted by the medium manages to escape.

The emission and absorption coefficients must include contributions from both the gas and the dust. For thermal dust continuum the coefficients are given by

$$j_{\nu,\text{dust}} = \alpha_{\nu,\text{dust}} B_\nu(T_{\text{dust}}) \quad (2.2.8)$$

$$\alpha_{\nu,\text{dust}} = \kappa_\nu \rho_{\text{dust}} \quad (2.2.9)$$

where ρ_{dust} is the dust mass density and κ_ν the dust opacity. The gas emission and absorption coefficients for a transition at frequency ν between an upper level, u and a lower level l is expressed as

$$j_{\nu,\text{gas}} = \frac{h\nu}{4\pi} \varphi_\nu n_u A_{ul} \quad (2.2.10)$$

$$\alpha_{\nu,\text{gas}} = \frac{h\nu}{4\pi} (n_l B_{lu} \psi_\nu - n_u B_{ul} \chi_\nu) \quad (2.2.11)$$

where n is the level populations. φ_ν denotes the normalized spontaneous emission, ψ_ν the absorption, and χ_ν the stimulated emission line profile functions. These are usually assumed to have a Gaussian shape, and they become identical if complete angular and frequency redistribution is assumed, i.e., any absorbed photon can be re-emitted at any line frequency and direction (independent of incident photon) so that the second equation above becomes

$$\alpha_{\nu,\text{gas}} = \frac{h\nu}{4\pi} (n_l B_{lu} - n_u B_{ul}) \psi_\nu \quad (2.2.12)$$

where ψ_ν is the common line shape.

As shown in the equations above, the emission and absorption depends on the Einstein coefficients for spontaneous emission (A_{ul}), absorption (B_{lu}) and stimulated/induced emission (B_{ul}). The relation between these Einstein coefficients are given by

$$A_{ul} = \frac{2h\nu^3}{c^2} B_{ul} \quad (2.2.13)$$

$$g_l B_{lu} = g_u B_{ul} \quad (2.2.14)$$

where g is the statistical weight of a energy level. Thus from a given level population of a molecule the radiative transfer equation can be used to calculate the intensity of a specific transition. However, the ambient radiation field affects the level populations, and the change in population of the i -th level is given by

$$\frac{dn_i}{dt} = \sum_{f \neq i}^N n_j P_{if} - n_i \sum_{f \neq i}^N P_{if}. \quad (2.2.15)$$

Here N is the number of levels considered. When the populations are in statistical equilibrium ($dn_i/dt = 0$), the populating and de-populating events per time interval are equal. Thus given all processes that populate and de-populate a level, the populations can be calculated. If the initial energy level is lower than the final ($E_i < E_f$) only absorption and collisional excitation is important, thus the rates P_{if} are given by

$$P_{if} = B_{if} \bar{J}_{if} + C_{if} \quad \text{if } E_i < E_f \quad (2.2.16)$$

where C_{if} is the collision rates and A and B the Einstein coefficients for the specific transitions. If on the other hand the initial energy level is higher ($E_i > E_f$) spontaneous emission, induced emission (i.e., stimulated emission, part of B_{if}) and collisions have to be accounted for.

$$P_{if} = A_{if} + B_{if} \bar{J}_{if} + C_{if} \quad \text{if } E_i > E_f \quad (2.2.17)$$

Here, \bar{J}_{ij} is the ambient radiation field - the specific intensity integrated over frequency and the entire sky.

$$\bar{J}_{if} = \frac{1}{4\pi} \int \int I_\nu d\nu d\Omega \quad (2.2.18)$$

The collision rates are given by the density of the collision partner n_{col} multiplied by the collisional rate coefficient (i.e., $C_{if} = n_{\text{col}} K_{if}$). The collisional rate coefficient is given by the

$$K_{if} = \left(\frac{8kT}{\pi\mu}\right)^{-1/2} \left(\frac{1}{kT}\right)^2 \int \sigma E e^{-E/kT} dE \quad (2.2.19)$$

where σ is the mean collision cross section, μ the reduced mass and E the collision energy in the center-of-mass system (Schöier et al. 2005). The inverse collision rate is given by

$$K_{if} = K_{fi} \frac{g_i}{g_f} e^{-h\nu/kT}. \quad (2.2.20)$$

This means that the level populations and the radiation field are coupled, and they have to be solved to get the line intensity of a given molecular transition. Because it is computationally heavy to do this, several methods to decouple the two processes are usually employed to solve the situation. Collisional rate coefficients is one of the large uncertainties in analysis of the molecular excitation. For collisions with H_2 , rates have only been measured for a few molecular species and the uncertainties may be larger than 20% in some cases. The collision rates together with most basic molecular data needed for the calculations (Einstein A-coefficients, statistical weights etc) are given in the LAMDA database (Schöier et al. 2005)².

2.2.3 Escape probability

One way to decouple the equations is to look at the fraction of photons that manage to escape from the cloud, we call this probability P_ν . If we ignore the background radiation field and the local continuum the intensity inside the cloud is $\bar{J}_\nu = S(1 - P_\nu)$, if $P_\nu = 0$ the average radiation field would equal the source function but some photons escape the region making them different. This simplification means that the level populations (Equation 2.2.15) are decoupled from the radiation field. Expressions of P for different geometries and optical depths have been derived. The escape probability should of course be unity for $\tau = 0$, and decrease with increasing optical depth. For a homogeneous spherical nebula, the expression for P was given by (Osterbrock 1989) as

$$P(\tau_R) = \frac{3}{4\tau_R} \left[1 - \frac{1}{2\tau_R^2} + \left(\frac{1}{\tau_R} + \frac{1}{2\tau_R^2} \right) e^{-2\tau_R} \right]. \quad (2.2.21)$$

Where τ_R is the optical radius of the cloud. Homogeneous means that the physical conditions are constant throughout the region, which means the excitation of the molecule is constant. The homogeneous region can thus be represented by a single

²<http://home.strw.leidenuniv.nl/~moldata/>

source function. A non-homogeneous region can be split up into cells that are assumed to be locally homogeneous, and coupled by various methods. The escape probability have been derived for other geometries as well, such as the plane-parallel homogeneous slab, and the so called Large Velocity Gradient approximation (LVG, Sobolev approximation, Sobolev 1960; de Jong et al. 1980). The assumed expression for the average radiation field and Equation 2.2.15 are then solved iteratively, and once converged the line intensity is determined from Equation 2.2.7. The software RADEX (van der Tak et al. 2007) is an example of a radiative transfer modeling tool that utilizes this simplification.

2.2.4 Local thermal equilibrium

If local thermodynamic equilibrium is assumed the level populations are given by Equation 2.2.2. This means that the temperature is

$$T_{\text{ex}} = -\frac{h\nu}{k_{\text{B}}} \left(\ln \frac{g_{\text{u}}n_{\text{u}}}{g_{\text{l}}n_{\text{l}}} \right)^{-1}. \quad (2.2.22)$$

The excitation temperature is specific to each transition, but equal to the ambient kinetic gas temperature in LTE. In the low density limit, the level populations will equilibrate with the radiation field (i.e., $T_{\text{ex}} \rightarrow T_{\text{rad}}$). Thus, the source function is $S_{\nu} = B_{\nu}(T_{\text{ex}})$. The density where spontaneous emission and collisional de-excitation is equally likely is called critical density, and is used as a indication if LTE is applicable or not. In the optically thin limit it is given by

$$n_{\text{crit}} = \frac{A_{\text{ul}}}{\sum_i K_{\text{ui}}}. \quad (2.2.23)$$

When the medium is optically thick one has to account for the number of photons that leave the region. Thus with the same notation of the escape probability introduced in the previous section we have

$$n_{\text{crit}}(\tau_{\nu}) = \frac{A_{\text{ul}}P_{\nu}}{\sum_i K_{\text{ui}}} \quad (2.2.24)$$

$$n_{\text{crit}}(\tau_{\nu}) \approx \frac{1}{\tau_{\nu}} n_{\text{crit}}. \quad (2.2.25)$$

2.2.5 Random walk and lambda iteration

One method to solve the radiative transfer problem is the iteration method called Lambda Iteration. It comprises of making an initial guess for the mean intensity (J_{ν}) and integrating the radiative transfer equation (Equation 2.2.6) along a large number

of rays. Enough rays need to be integrated so that for each point in the model an approximate estimate of the mean intensity can be computed from the level populations. This is repeated until the level populations and the radiation field agree, i.e. the solution has converged. The operation is written as

$$\bar{J}_{if} = \Lambda_{if} [S_{if}]. \quad (2.2.26)$$

The brackets show that the computation involves integrals of the entire model. Accelerated or Approximate Lambda Iteration uses another operator, which is an approximation of the full lambda operator and other methods to decrease the time it takes for the iteration to converge.

Instead of using a fixed set of rays, as in Lambda Iteration, one can use a set of random rays to solve the radiative transfer problem. The Monte Carlo Method uses this approach, and further improvements to this implementation exists to speed up the convergence. In this thesis, the 1D tool RATRAN, which uses this approach, is used to do the non-LTE radiative transfer. We compare this to LTE solutions in one of the sources and generally find that, given the uncertainties, the methods give similar results.

The Research

3.1 List of publications

The published publications included in this thesis are:

- “Subarcsecond resolution observations of warm water towards three deeply embedded low-mass protostars”, Persson, M. V., Jørgensen, J. K., van Dishoeck, E. F., 2012, *A&A*, 541, 39
- “Warm water deuterium fractionation in IRAS 16293-2422 - The high-resolution ALMA and SMA view”, Persson, M. V., Jørgensen, J. K., van Dishoeck, E. F., 2013, *A&A*, 549, L3

One manuscript that is to be submitted shortly is also included:

- “The water deuterium fractionation on solar-system scales in three deeply-embedded low-mass protostars”, Persson, M. V., Jørgensen, J. K., van Dishoeck, E. F., Harsono, D.

3.2 Results and Conclusions

This thesis presents ground based interferometric observations of water isotopologues toward embedded protostars with the aim of disentangle the origin of the warm water emission lines seen in low-mass protostars. Several lines of water were targeted in a small survey of deeply-embedded low-mass protostars.

3.2.1 Paper I

The first paper presents observations of the H_2^{18}O $3_{1,3} - 2_{2,0}$ transition at 203.4 GHz toward the deeply-embedded (Class 0) low-mass protostars IRAS2A and IRAS4A in the

NGC 1333 star forming complex in the Perseus region. This is combined with previous successful observations of IRAS4B, of the same water line, in the same complex using the same telescope, the PdBI Jørgensen & van Dishoeck (2010b). Water is detected toward IRAS2A and one component of the IRAS4A, adding to the previous detection of the same transition toward IRAS4B. The mapped emission is compact and traces warm water on scales $R < 50\text{-}200$ AU. The origin of the emission differs from that seen with both *Herschel* and *Spitzer*, where larger-scale emission (protostellar envelope, outflow shocks/cavity walls) is detected (e.g., Herczeg et al. 2012; Kristensen et al. 2012).

While IRAS4B shows narrow emission lines and a tentative velocity gradient, reported by Jørgensen & van Dishoeck (2010b), the other sources in NGC 1333 show broader lines and no velocity gradients. Additionally, IRAS4B is the only source of the three NGC 1333 sources detected in mid-infrared water lines by Watson et al. (2007). We propose that a disk-like structure dominated by inward motions as a solution to explain the observed line characteristics.

Toward IRAS2A, the H_2^{18}O emission is not only detected at the source position, but also in the blueshifted outflow. With lower resolution observations, this extended emission could not have been separated from the on-source emission. However, in the high-resolution observations this can be accounted for.

By assuming an excitation temperature of 170 K, same as assumed by Watson et al. (2007) and Jørgensen & van Dishoeck (2010b), and LTE abundances are derived. A comparison of the H_2^{18}O abundance and the other detected species shows some interesting results. The ratio between dimethyl ether and water, sulfur dioxide and water are roughly constant between the three sources IRAS2A, IRAS4A and IRAS4B. However, the ratio between ethyl cyanide and water does not show this same consistency. The ratio is much lower toward IRAS2A than the other sources. This shows that the formation mechanism for $\text{C}_2\text{H}_5\text{CN}$ is different from the other molecules, indicating that it is not trapped in the water ice mixture or related to the sublimation of water.

Based on the small species-to-species variations, in both line strength and line width, we argue that the H_2^{18}O line at 203.4 is not masing in these environments and on these scales.

3.2.2 Paper II

The second paper presents observations of water toward the deeply-embedded low-mass proto-binary system IRAS 16293-2422 in ρ Ophiuchus. The 203.4 GHz line of H_2^{18}O and the HDO $3_{1,2} - 2_{2,1}$ transition at 225 GHz were observed using the SMA, and ALMA Band 9 Science Verification data of the 692.1 GHz $5_{3,2} - 4_{4,1}$ transition of H_2^{18}O was also used.

The detected emission is compact, and toward one of the components of the binary system, source A, all lines are seen. Toward the other component, source B, only one line is detected, the 692 GHz H_2^{18}O line, and in absorption. The spectral line is slightly

red-shifted compared to the system velocity of source B, consistent with the picture of ongoing infall in this source (Jørgensen et al. 2012; Pineda et al. 2012). Integrating over a larger velocity interval reveals, in addition to the absorption, a blueshifted emission peak, offset $\sim 0''.2$ south of the absorption.

With two lines of H_2^{18}O observed, the excitation temperature (T_{ex}) can be estimated, if LTE is assumed. The derived excitation temperature for H_2^{18}O is $T_{\text{ex}} = 124 \pm 12$. With this estimate of the excitation temperature, the column densities are derived. From these a water deuterium fractionation ($\text{HDO}/\text{H}_2\text{O}$ ratio) is calculated, for source A of the IRAS 16293-2422 binary we get an $\text{HDO}/\text{H}_2\text{O}$ of $9.2 \pm 2.6 \times 10^{-4}$. Previous estimates based on models of single-dish observations (Parise et al. 2005; Coutens et al. 2012) derived a higher ratio, $\sim 0.3 \times 10^{-2}$. The deduced $\text{HDO}/\text{H}_2\text{O}$ ratio in this paper, in the warm gas of IRAS 16293-2422 is only slightly higher than found in Earth's oceans and by recent *Herschel* observations of comets.

The same argument for non masing as brought up in the previous paper can be applied to this dataset as well, with the addition of detecting the 692 GHz in absorption, which it would be hard to explain if it was indeed masing.

3.2.3 Paper III

The third paper, which will be submitted soon, presents observations of the $3_{1,2} - 2_{2,1}$ transition of HDO toward the same sources as in the first paper: IRAS2A, IRAS4A and IRAS4B. The HDO emission is mostly compact, with some extended emission which would be included in any lower resolution observations. The line widths and intensities agree for all the sources. In addition to the HDO line presented above, the $2_{1,1} - 2_{1,2}$ transition at 241.6 GHz of HDO (with a different E_{u}) was observed toward IRAS2A. Thus a T_{ex} can be estimated, and for IRAS2A we get $T_{\text{ex}} = 124 \pm 60$ K, which is not a unreasonable estimate for these sources and regions.

With an estimate of the excitation temperature, the abundances of HDO and a $\text{HDO}/\text{H}_2\text{O}$ ratio can be estimated using the results from Persson et al. (2012). The water deuterium fractionation deduced for IRAS2A: $7.4 \pm 2.1 \times 10^{-4}$, for IRAS4A-NW: $19.1 \pm 5.4 \times 10^{-4}$ and for IRAS4B: $5.9 \pm 1.7 \times 10^{-4}$, these values add to that previously derived for IRAS 16293-2422 from interferometric observations (Persson et al. 2013). These values are slightly higher than that found in Earth's oceans (3.1×10^{-4}), and shows that the water goes through small amounts of chemical processing, if the reservoirs are linked, before being incorporated into comets.

The results of Persson et al. (2013) was used in radiative transfer modeling of IRAS 16293-2422, where the model used by Coutens et al. (2012) were used to derive the abundances and $\text{HDO}/\text{H}_2\text{O}$ ratios. The modeling highlights the uncertainties involved in the derivation of the $\text{HDO}/\text{H}_2\text{O}$ ratio. The models can not give results of higher confidence than the LTE approximation made previously. Until the physical structure on small scales can be constrained, running radiative transfer modeling will

not yield a more accurate HDO/H₂O ratio in the warm gas in the inner region of deeply-embedded low-mass protostars.

3.3 Outlook

The observed patterns in the abundance ratios between water and dimethyl ether, ethyl cyanide and sulfur dioxide is an interesting aspect of the results. Since sulfur dioxide is traditionally a tracer of outflow emission (e.g., Bachiller & Perez Gutierrez 1997), one future project would be to observe the same lines of water and other species toward a outflow shock. Observations of complex organics in outflows show that shocks are causing complex organics to be released in the molecular outflow of protostars (e.g., Arce et al. 2008). The sputtering of water ice releases the molecules into the gas-phase, although water itself can be formed directly in the gas-phase (c.f. Sect. 1.2.2), thus changing the relative abundances. If shocks are the responsible mechanism for both the on-source emission as well as that of outflows, similarities in the two observations would be seen for the relevant species.

One possibility could be to observe D₂O to see how different the D/H value in D₂O/HDO is compared to in HDO/H₂O, and why. These ratios are affected by the different water formation scenarios described in Sect. 1.2.2 (see e.g., Butner et al. 2007). The D₂O line at 316 GHz was observed toward IRAS 16293-2422 by Butner et al. (2007) using the James Clerk Maxwell Telescope (15 m, JCMT) and the Caltech Submillimeter Observatory (10 m, CSO). This line is accessible at the PdBI, SMA and ALMA. However, the line is weak which translates into long integration times, at least at the PdBI and SMA telescopes. With ALMA, sufficient sensitivity could be reached very quickly (hours instead of days).

Another possible future project would be to observe more evolved sources, i.e., Class I sources. These are weaker at (sub)mm wavelengths than the Class 0 sources, but the lines should be observable towards luminous sources. Measuring the water content and isotopic composition could shed light on the evolutionary aspect on all of the problems stated in this thesis. Water has been observed in the infrared for Class I sources (e.g., Boogert et al. 2008), but this is mainly ices or shocked gas, interferometers have the possibility to map the warm emission present in the disk.

For Class 0 sources, the structure in the inner < 300 AU need to be constrained more to put stronger limits on the abundances and ratios. High resolution observations (<0''2, i.e., using ALMA) of these water lines, could shed light on the structure, because water is believed to have a significant abundance jump when the dust temperature reaches above 100 K (Fraser et al. 2001). Another way is using high-resolution continuum observations. These observations in combination with radiative transfer modeling with increasing geometric complexity could constrain the structure on small scales.

With high resolution observations of water, the radial dependence could be mapped.

Simulations of the formation of our own solar system shows gradients in the deuterium fractionation of species (e.g., Hersant et al. 2001; Kavelaars et al. 2011), and observations of water could test this, improving the understanding of the formation of our own solar system.

In summary, with high sensitivity and resolution, future observations of water and related species toward deeply-embedded low-mass protostars and its surrounding have the potential to shed light on many interesting aspects of star formation.

PUBLICATIONS

Paper I

Subarcsecond resolution observations of warm water toward three deeply embedded low-mass protostars*

M. V. Persson^{1,2}, J. K. Jørgensen^{2,1} and E. F. van Dishoeck^{3,4}

¹ Centre for Star and Planet Formation, Natural History Museum of Denmark, University of Copenhagen, Øster Voldgade 5-7, DK-1350, Copenhagen K, Denmark

² Niels Bohr Institute, University of Copenhagen, Juliane Maries Vej 30, DK-2100 Copenhagen Ø, Denmark

³ Leiden Observatory, Leiden University, P.O. Box 9513, NL-2300 RA Leiden, The Netherlands

⁴ Max-Planck Institute für extraterrestrische Physik (MPE), Giessenbachstrasse, 85748 Garching, Germany

Appeared in *Astronomy & Astrophysics* Year 2012, Volume 541

ABSTRACT

Context Water is present during all stages of star formation: as ice in the cold outer parts of protostellar envelopes and dense inner regions of circumstellar disks, and as gas in the envelopes close to the protostars, in the upper layers of circumstellar disks and in regions of powerful outflows and shocks. Because of its key importance in the understanding of its origin in our own solar system, following the evolution of water all the way to the planet-forming disk is a fundamental task in research in star formation and astrochemistry.

Aims In this paper we probe the mechanism regulating the warm gas-phase water abundance in the innermost hundred AU of deeply embedded (Class 0) low-mass protostars, and investigate its chemical relationship to other molecular species during these stages.

Methods Millimeter wavelength thermal emission from the para- H_2^{18}O $3_{1,3} - 2_{2,0}$ ($E_u=203.7$ K) line is imaged at high angular resolution ($0''.75$; 190 AU) with the IRAM Plateau de Bure Interferometer toward the deeply embedded low-mass protostars NGC 1333-IRAS2A and NGC 1333-IRAS4A.

Results Compact H_2^{18}O emission is detected toward IRAS2A and one of the components in the IRAS4A binary; in addition CH_3OCH_3 , $\text{C}_2\text{H}_5\text{CN}$, and SO_2 are detected. Extended water emission is seen toward IRAS2A, possibly associated with the outflow.

Conclusions The results complement a previous detection of the same transition toward NGC 1333-IRAS4B. The detections in all systems suggests that the presence of water on $\lesssim 100$ AU scales is a common phenomenon in embedded protostars and that the non-detections of hot water with *Spitzer* toward the two systems studied in this paper are likely due to geometry and high extinction at mid-infrared wavelengths. We present a scenario in which the origin of the emission from warm water is in a flattened disk-like structure dominated by inward motions rather than rotation. The gas-phase water abundance varies between the sources, but is generally much lower than a canonical abundance of 10^{-4} , suggesting that most water (>96%) is frozen out on dust grains at these scales. The derived abundances of CH_3OCH_3 and SO_2 relative to H_2^{18}O are comparable for all sources pointing toward similar chemical processes at work. In contrast, the $\text{C}_2\text{H}_5\text{CN}$ abundance relative to H_2^{18}O is significantly lower in IRAS2A, which could be due to different chemistry in the sources.

4.4 Introduction

Water is a key molecule in regions of star formation. In cold outer regions of protostellar envelopes and dense mid-planes of circumstellar disks, it is the most abundant molecule in the ices on dust

*Based on observations carried out with the IRAM Plateau de Bure Interferometer. IRAM is supported by INSU/CNRS(France), MPG (Germany) and IGN (Spain).

grains (e.g. Gibb et al. 2004; Boogert et al. 2008). In regions of increased temperatures (e.g., due to protostellar heating or active shocks) it desorbs and becomes an important coolant for gas (Ceccarelli et al. 1996; Neufeld & Kaufman 1993). As one of the major oxygen reservoirs it also influences the oxygen based chemistry (e.g. van Dishoeck & Blake 1998). This paper presents high-angular resolution observations ($0''.75$) at 203.4 GHz of the H_2^{18}O isotopologue toward two deeply embedded (Class 0) low-mass protostars using the Institut de Radioastronomie Millimétrique (IRAM) Plateau de Bure Interferometer (PdBI), one of the few water lines that can be routinely observed from Earth. The aim of the observations is to determine the origin of water emission lines in the inner 100 AU of these protostars.

The young, dust- and gas-enshrouded protostars provide an important laboratory for studies of the star formation process. On the one hand, they provide the link between the prestellar cores and the young stellar objects (YSOs) and on the other hand it is likely that during these stages the initial conditions for the later astrochemical evolution of the protostellar envelopes and disks are established (e.g., Visser et al. 2009). In the earliest stages most of the gas and dust is present on large scales in the protostellar envelopes where the temperatures are low (10–20 K) and most molecules, including water, are locked up as ice on grains. Nevertheless, space-based observations from *ISO*, *SWAS*, *Odin*, *Spitzer* and *Herschel* show that significant amounts of gas-phase water are present toward even deeply embedded protostars, pointing to significant heating and processing of water-ice covered grains (Nisini et al. 1999; Ceccarelli et al. 1999; Maret et al. 2002; Bergin et al. 2003; Franklin et al. 2008; Watson et al. 2007; van Dishoeck et al. 2011; Kristensen et al. 2010).

Exactly which mechanism regulates where and how the heating and evaporation of the water ice takes place is still debated. Proposed locations and mechanisms include the innermost envelope, heated to temperatures larger than 100 K by the radiation from the central protostar on scales $\lesssim 100$ AU (Ceccarelli et al. 1998; Maret et al. 2002), in shocks of the protostellar outflow (Nisini et al. 1999), or in the disk – heated either by shocks related to ongoing accretion onto the circumstellar disks or in their surface layers heated by the protostar (Watson et al. 2007; Jørgensen & van Dishoeck 2010b).

Recently, Watson et al. (2007) observed 30 Class 0 protostars, including the sources in this paper, with the infrared spectrograph (IRS) on board *Spitzer*. The protostar NGC 1333-IRAS4B (IRAS4B) showed a wealth of highly excited H_2O lines, and was the only source in the sample in which the water lines were detected. By modeling the spectra they concluded that because of the high inferred density and temperature of the water, it originates in the vicinity of the protostar, likely accretion shocks in the circumstellar disk. However, the *Spitzer* data, and similar observations from space, lack the spatial and spectral resolution to unambiguously associate the emission with the components in the protostellar systems – and can for the shorter wavelengths also be hampered by extinction by the dust in the protostellar envelopes and disks. Herczeg et al. (2012) analyzed the emission from warm water lines in maps toward IRAS4B obtained with the PACS instrument on the *Herschel Space Observatory*. The maps show that the bulk of the warm water emission has its origin in a outflow-driven shock offset by about $5''$ (1200 AU) from the central protostar. An excitation analysis of the emission furthermore shows that the temperature in the shocked region is about 1500 K, which can simultaneously explain both the far-IR (*Herschel*) and mid-IR (*Spitzer*) water lines.

Higher angular and spectral resolution is possible through interferometric observations of H_2^{18}O which has a few transitions that can be imaged from the ground (e.g. Jacq et al. 1988; Gensheimer et al. 1996; van der Tak et al. 2006). Jørgensen & van Dishoeck (2010b) report observations of IRAS4B with the PdBI. They detect the H_2^{18}O $3_{1,3} - 2_{2,0}$ line at 203.4 GHz, and also resolve a tentative velocity gradient in the very narrow line (~ 2 km s $^{-1}$ width at zero intensity), indicating an origin of the H_2^{18}O emission in a rotational structure. The H_2O column density is around 25 times higher than previously estimated from mid-IR observations by Watson et al. (2007), on similar size scales (inner 25 AU of the protostar).

This study presents similar high angular resolution H_2^{18}O millimeter wavelength observations for the sources NGC 1333-IRAS2A (IRAS2A) and NGC 1333-IRAS4A (IRAS4A), which are compared

to IRAS4B. The three sources are all deeply embedded Class 0 protostars in the nearby NGC 1333 region of the Perseus molecular cloud¹ identified through early infrared and (sub)millimeter wavelength observations (e.g., Jennings et al. 1987; Sandell et al. 1991). All sources were mapped by *Spitzer* (Jørgensen et al. 2006; Gutermuth et al. 2008), and were part of the high resolution ($\sim 1''$) PROSAC survey of Class 0/I sources using the Submillimeter Array (SMA; Jørgensen et al. (2007, 2009)). Their similar luminosities (20, 5.8^2 , $3.8 L_{\odot}$ for IRAS2A, IRAS4A and IRAS4B, respectively) and envelope masses ($1.0, 4.5^2, 2.9 M_{\odot}$, respectively) from those surveys, and thus presumably also similar evolutionary stages, make them ideal for studying and comparing deeply embedded young stellar objects in the same environment.

IRAS4A is a binary system with a $1''.8$ separation (Looney et al. 2000; Reipurth et al. 2002; Girart et al. 2006), associated with a larger scale jet and outflow (e.g. Blake et al. 1995; Jørgensen et al. 2007). The jet axis has been deduced from water maser observations associated to IRAS4A-NW to 2° in the plane of the sky and at a position angle (PA) of -50° (north through east, Marvel et al. 2008; Desmurs et al. 2006), almost perpendicular to the CO outflow axis (PA = $0^{\circ} - 45^{\circ}$; Blake et al. (1995); Jørgensen et al. (2007)). The mass of the NW source is estimated from modeling to $0.08 M_{\odot}$ (Choi et al. 2010), no estimate of the mass of the SE source exists. The envelope is dominated by inward motion, as evident from the inverse P-Cygni profiles in the spectra and modeling of gas kinematics (Di Francesco et al. 2001; Attard et al. 2009; Kristensen et al. 2010).

The other source, IRAS2A, shows two bipolar outflows, one shell-like directed N-S (PA $\approx +25^{\circ}$, Jørgensen et al. 2007) and the other a jet-like directed E-W (PA $\approx +105^{\circ}$, Liseau et al. 1988; Sandell et al. 1994; Jørgensen et al. 2004). Water maser emission has been detected toward IRAS2A, partly associated with the northern redshifted outflow (Furuya et al. 2003). One proposed solution to the presence of a quadrupolar outflow is that IRAS2A is a binary system with $0''.3$ (75 AU) separation (Jørgensen et al. 2004).

The paper is laid out as follows. Sect. 4.5 presents the interferometric observations of the three Class 0 sources that the paper is based upon. Sect. 4.6 presents the results from the analysis of the spectra and maps. Sect. 4.7 discusses the detection of water, and the column density estimates. Sect. 4.8 presents a summary of the important conclusions and suggests possible future work.

4.5 Observations

Three low-mass protostars, IRAS2A, IRAS4A-SE and -NW in the embedded cluster NGC 1333 in the Perseus molecular cloud were observed using the PdBI. IRAS2A and IRAS4A were observed in two configurations each: the B configuration on 6, 15 and 17 March 2010 and the C configuration on 9 December 2009. The sources were observed in track-sharing mode for a total of 12 hours in B configuration and about 8 hours in C configuration. Combining the observations in the different configurations, the data cover baselines from 15.4 to 452 m (10.5 to 307 k λ). The receivers were tuned to the para- H_2^{18}O $3_{1,3} - 2_{2,0}$ transition at 203.40752 GHz (1.47 mm) and the correlators were set up with one unit with a bandwidth of 40 MHz (53 km s^{-1}) centered on this frequency providing a spectral resolution on 460 channels of 0.087 MHz (0.115 km s^{-1}) width.

The data were calibrated and imaged using the CLIC and MAPPING packages, which are parts of the IRAM GILDAS software. The general calibration procedure was followed: regular observations of the nearby, strong quasar 0333+321 were used to calibrate the complex gains and bandpass, while MWC349, 0333+321 and 3C84 were observed to calibrate the absolute flux scale. Integrations with significantly deviating amplitudes/phases were flagged and the continuum was subtracted before Fourier transformation of the data. The resulting beam sizes using natural weighting, along with other data,

¹In this paper we adopt a distance of 250 pc to the Perseus molecular cloud (Enoch et al. 2006, and references therein).

²The luminosity and mass estimates for IRAS4A refer to the binary system.

are given in Table 4.1. The field of view is $25''$ (HPBW) at 1.45 mm and the continuum sensitivity is limited by the dynamical range of the interferometer while the line data RMS is given in Table 4.1. The uncertainty in fluxes is dominated by the flux calibration error, typically 20%.

Source	Beam ^a	PA	RMS ^b
IRAS2A	$0''.87 \times 0''.72$	63.5°	16.1
IRAS4A(-SE/NW)	$0''.86 \times 0''.70$	63.4°	16.5

(^a) Major \times minor axis. (^b) Units of mJy beam⁻¹ channel⁻¹

Table 4.1: Parameters from the observations.

4.6 Results

Continuum emission from the targeted sources (IRAS2A and the IRAS4A-NW and IRAS4A-SE binary) was detected at levels expected from previous high resolution millimeter wavelength continuum observations: parameters from elliptical Gaussian fits to the continuum emission for the sources are given in Table 4.2. The continuum emission toward the sources is resolved and the fluxes concur with the results of Jørgensen et al. (2007), assuming a power-law spectrum ($F_\nu \propto \nu^\alpha$) with $\alpha \sim 2.3$ – 2.7 , expected for thermal dust continuum emission.

	IRAS2A	IRAS4A-NW	IRAS4A-SE
Flux (\pm) ^a	0.24 (0.002) Jy	0.88 (0.025) Jy	1.46 (0.021) Jy
R.A (\pm) ^b	03:28:55.57 ($0''.004$)	03:29:10.44 ($0''.02$)	03:29:10.53 ($0''.005$)
Dec (\pm) ^b	31:14:37.03 ($0''.004$)	31:13:32.16 ($0''.02$)	31:13:30.92 ($0''.006$)
Extent ^c	$1''.1 \times 1''.0$ (23°)	$2''.0 \times 1''.2$ (-53°)	$1''.4 \times 1''.0$ (50°)

(^a) Statistical error from fit, the calibration dominates the uncertainty in the flux determination. (^b) J2000 epoch. Statistical error from fit. (^c) Major \times Minor axis and position angle for elliptical Gaussian profile in (u, v) plane. The statistical error of the extent is typically 0.5 – 3%.

Table 4.2: Parameters for the sources from elliptical Gaussian fits to their continuum emission. Errors given are the statistical errors from the fitting routine.

Figure 4.1 shows the spectrum toward the continuum peak of these sources, as well as IRAS4B (Jørgensen & van Dishoeck 2010b). A number of lines are detected toward IRAS2A and one component in the IRAS4A protobinary system, IRAS4A-NW. IRAS4A-SE in contrast does not show any emission lines in the high-resolution spectra, and it is therefore only listed in the table showing the characteristics of the continuum emission.

The Jet Propulsion Laboratory (JPL, Pickett et al. 1998) and the Cologne Database for Molecular Spectroscopy (CDMS, Müller et al. 2001) databases were queried through the Splatalogue interface to identify the lines. The line widths and strengths vary between the sources and because of the broader line widths some blending between the different CH_3OCH_3 lines occurs in both IRAS2A and IRAS4A-NW. As seen in Figure 4.1, several lines are detected: the target water line, SO_2 and several lines of CH_3OCH_3 . $\text{C}_2\text{H}_5\text{CN}$ is seen in IRAS 4A-NW and IRAS4B, but not in IRAS2A.

Particular interesting for this study is the assignment of the H_2^{18}O $3_{1,3} - 2_{2,0}$ transition ($E_u = 203.7$ K). No other lines fall within ± 1 km s⁻¹ of the H_2^{18}O $3_{1,3} - 2_{2,0}$ line listed in the spectral line catalogs. The lines that fall close (± 1 – 2 km s⁻¹) are $^{13}\text{CH}_2\text{CHCN}$, $^{13}\text{CH}_3\text{CH}_2\text{CN}$ and $(\text{CH}_3)_2\text{CO}$. Both the $^{13}\text{CH}_2\text{CHCN}$ and $^{13}\text{CH}_3\text{CH}_2\text{CN}$ isotopologues have other transitions which would have been detected, whereas a possible transition of $(\text{CH}_3)_2\text{CO}$ has a too low intrinsic line strength to be plausible.

In Figure 4.2 the integrated intensity (zeroth order moment) and velocity (first order moment) maps for the H_2^{18}O transition are shown for the observed sources. For IRAS2A the calculations were made over the velocity interval from 4.4 to 11.4 km s^{-1} and for IRAS4A-NW from 4.7 to 9.6 km s^{-1} . The integrated intensity maps for IRAS2A show some extended emission, whereas for IRAS4A-NW the emission is compact around the continuum peak with a slight elongation in the north-south direction. The velocity maps for both IRAS2A and IRAS4A (right hand panels in Figure 4.2) show no obvious spatial gradients in velocity, neither on source nor along the outflow in IRAS2A.

For estimates of the physical conditions in the gas, circular Gaussian profiles were fitted to the emission of each line in the (u, v) -plane. The fits were performed to the line intensities typically integrated over the line widths ($v_{\text{lsr}} \pm \text{FWHM}$) and are given in Table 4.3. Table 4.5 lists the molecular parameters adopted in this paper of the target line $\text{H}_2^{18}\text{O } 3_{1,3} - 2_{2,0}$, and other detected lines, while Table 4.6. lists the position, FWHM and integration interval for the different lines.

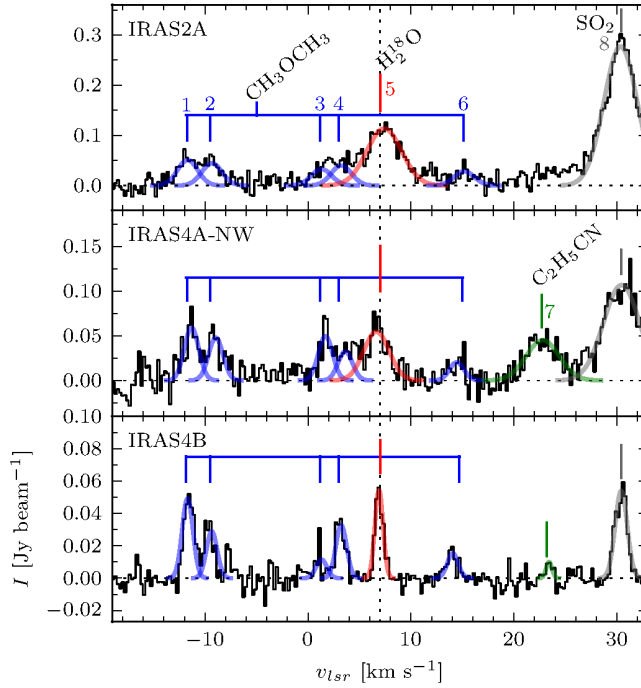


Figure 4.1: Spectra extracted in a pixel toward the continuum peak positions for IRAS2A, IRAS4A-NW and IRAS4B. The identified lines are marked, including the targeted $\text{H}_2^{18}\text{O } 3_{1,3} - 2_{2,0}$ line. Parameters from the fits are tabulated in Table 4.6.2. The numbers above the lines and the colors correspond to the numbers (emission lines) and colors in Figure 4.3, Table 4.3, Table 4.5 and Table 4.6.2. The spectra have been binned to a width of 0.23 km s^{-1} (i.e., 2 channels per bin), and Gaussian profiles have been fitted to the identified lines. The systemic velocity of the H_2^{18}O line is marked by the vertical dotted line at $v_{\text{lsr}} = 7.0 \text{ km s}^{-1}$. Note the difference in scale of the y -axis for the spectra.

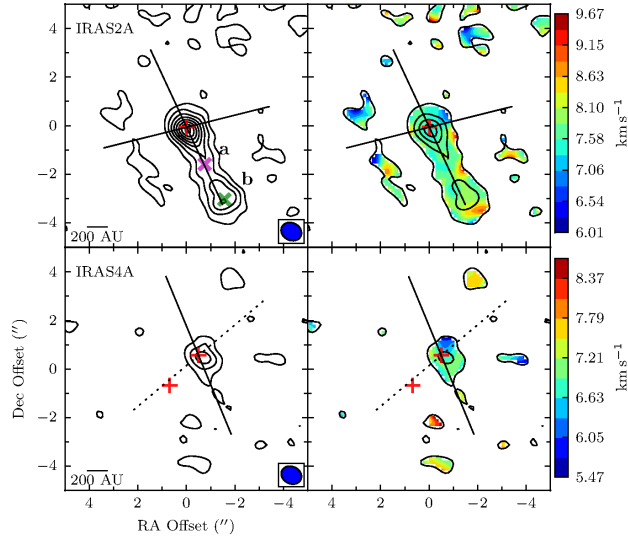


Figure 4.2: Integrated intensity (left) and velocity (right) maps for the H_2^{18}O $3_{1,3} - 2_{2,0}$ line in IRAS2A (from 4.4 to 11.4 km s^{-1}) and IRAS4A (from 4.7 to 9.6 km s^{-1}). Contours show integrated intensity and are in steps of 4σ for the intensity map, 8σ for the velocity map, and start at 3σ . The position of the continuum emission is marked by a red plus sign, an outflow by the solid line and maser emission by the dashed line. Positions where spectra have been extracted in IRAS2A along the outflow are marked with letters **a** and **b** and crosses with magenta and green colors in the integrated intensity map.

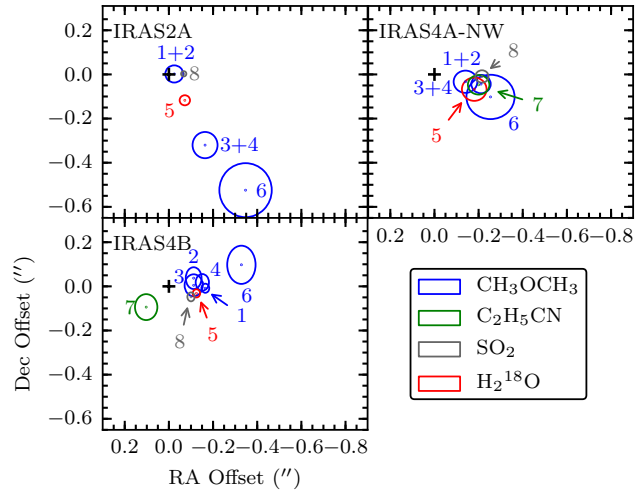


Figure 4.3: Positions of the lines from circular Gaussian fits in the (uv) -plane to the integrated line emission. The positions are plotted relative to the continuum peak position (cross) and the error in position for the lines is roughly the extent of the cross while the extent of the ellipses shows the error in position for the lines. Ellipses with the same colors represent the same molecule, while the numbers refer to a certain molecule and transition which has the same number in Figure 4.1, Table 4.3, Table 4.5 and Table 4.6.2. Many of the detected lines are systematically offset from the continuum peak.

No.	Molecule	Transition	IRAS2A			IRAS4A-NW		
			Flux ^a (Jy km s ⁻¹)	Offset ^b (")	Size ^c (")	Flux ^a (Jy km s ⁻¹)	Offset ^b (")	Size ^c (")
1	CH ₃ OCH ₃	3 _{3,0} - 2 _{2,1} EE	0.47 ^d	-0.02; -0.002	0.70 ± 0.09	0.44 ^d	-0.21; -0.04	0.70 ± 0.09
2	CH ₃ OCH ₃	3 _{3,0} - 2 _{2,1} AA	- ^d	-; -	-	- ^d	-; -	-
3	CH ₃ OCH ₃	3 _{3,0} - 2 _{2,1} AE	0.81 ^e	-0.16; -0.32	1.45 ± 0.10	0.26 ^e	-0.14; -0.03	0.57 ± 0.12
4	CH ₃ OCH ₃	3 _{3,1} - 2 _{2,1} EE	- ^e	-; -	-	- ^e	-; -	-
5	H ₂ ¹⁸ O	3 _{1,3} - 2 _{2,0}	0.98	-0.07; -0.12	0.83 ± 0.05	0.27	-0.18; -0.07	0.61 ± 0.12
6	CH ₃ OCH ₃	3 _{3,1} - 2 _{2,1} EA	0.30	-0.35; -0.52	1.23 ± 0.22	0.06	-0.25; -0.10	0.44 ± 0.26
7	C ₂ H ₅ CN	23 _{2,22} - 22 _{2,21}	< 0.04 ^f	-; -	-	0.27	-0.20; -0.05	0.37 ± 0.11
8	SO ₂	12 _{0,12} - 11 _{1,11}	2.73	-0.07; +0.003	1.00 ± 0.02	1.22	-0.22; -0.01	0.88 ± 0.05

(^a) Flux from fitting circular Gaussian to integrated line emission in (u, v) plane. The typical statistical error is 0.01 Jy km s⁻¹, but the calibration uncertainty is roughly 20%.

(^b) Offset from position of continuum fitted elliptical Gaussian. Used in Figure 4.3 to plot the positions of the lines.

(^c) FWHM from Gaussian fit in the (u, v) plane.

(^{d,e}) Blended pair, values given for the combined integrated emission.

(^f) Upper limit estimate.

Table 4.3: Parameters for the lines detected in the sources from circular Gaussian fits to the integrated line maps. Molecule specific data are tabulated in Table 4.5 and the integration interval (in km s⁻¹) in Table 4.6.2 in the appendix.

4.7 Analysis and discussion

The detected water lines provide important constraints on the physical and chemical structure of the deeply embedded low-mass protostars, which we discuss in this section. The first part of the discussion (Sect. 4.7.1–4.7.3) focuses on the detection of warm water on scales comparable to the protostellar disk and the extended emission found in the outflow toward IRAS2A. The implications for the geometry and dynamics are also discussed. The second part (Sect. 4.7.4–4.7.6) discusses excitation conditions in the water emitting gas and the column densities and relative abundances of water and other species detected on small scales.

4.7.1 Water on small scales

The key result from the presented observations is the detection of compact H_2^{18}O in IRAS2A and IRAS4A-NW, adding to the discovery toward IRAS4B (Jørgensen & van Dishoeck 2010b). Together, the observations demonstrate the presence of water emission on 100 AU scales – much smaller than probed by the recent *Herschel* (Kristensen et al. 2010) and *ISO* (Nisini et al. 1999) observations.

It is particularly noteworthy that the water emission is present in all these systems – and the integrated emission (spatially and spectrally) is in fact stronger in both IRAS4A and IRAS2A than in IRAS4B. This is in contrast to the space observations where the *Herschel* HIFI data show equally strong or stronger emission lines in IRAS4B than the other sources (Kristensen et al. 2010) and the *Spitzer* data only show detections in IRAS4B (Watson et al. 2007).

The extent of the emission estimated from the sizes of the circular Gaussian fits in the (u, v) plane (Table 4.3) differ between the sources: for IRAS2A emission from the different species is generally more extended ($0''.70$ and $1''.45$; 87–181 AU radii) than in IRAS4A-NW ($0''.37$ and $0''.88$; 46–110 AU radii). Still, for both sources (as well as IRAS4B), these results show that the bulk of the emission is truly coming from the inner 50–100 AU of the protostellar systems.

The positions of the emission differ slightly: Figure 4.3 shows the peak positions of Gaussian fits in the (u, v) -plane to the integrated intensity of the detected lines relative to the continuum position for the two sources, IRAS2A and IRAS4A-NW, from this paper as well as IRAS4B. The size of the ellipses show the statistical uncertainty in the Gaussian fits, and the numbers correspond to those in Figure 4.1, Table 4.3, Table 4.5 and Table 4.6.2 identifying each line. The position of the lines in the different sources show a systematic offset, in IRAS4A-NW and IRAS4B the lines are all (except $\text{C}_2\text{H}_5\text{CN}$ in IRAS4B) offset about $0''.2$ west of the continuum peak. When fitting the weak line of CH_3OCH_3 (line 6) in IRAS2A, an extra Gaussian was added, centered on the stronger extended emission to minimize its affect on the fit of the line. The offsets are smaller than the beam, but still significant given the signal-to-noise of the data. That the shifts are physical is further strengthened by the observation that they are similar for the observed species toward each source.

Chandler et al. (2005) detect similar offsets in the line emission of complex organic molecules relative to the continuum source toward IRAS 16293-2422 combining high-resolution SMA observations with archival VLA data. They argue that an outflow shock eastward of one component in the protostellar binary (“source A”) is responsible for enhancing the abundances, and sputtering the ices off the grains. Because the offsets seen here are not aligned with any larger scale outflow, and because a tentative velocity gradient perpendicular to the outflow is seen toward IRAS4B (Jørgensen & van Dishoeck 2010b), we argue that the lines detected here do not have their origin in the outflow. The line widths of $1.6 - 4.1 \text{ km s}^{-1}$ observed in these data (Sect. 4.7.4) are also significantly less than the outflow widths seen in *Herschel*-HIFI spectra (Kristensen et al. 2010).

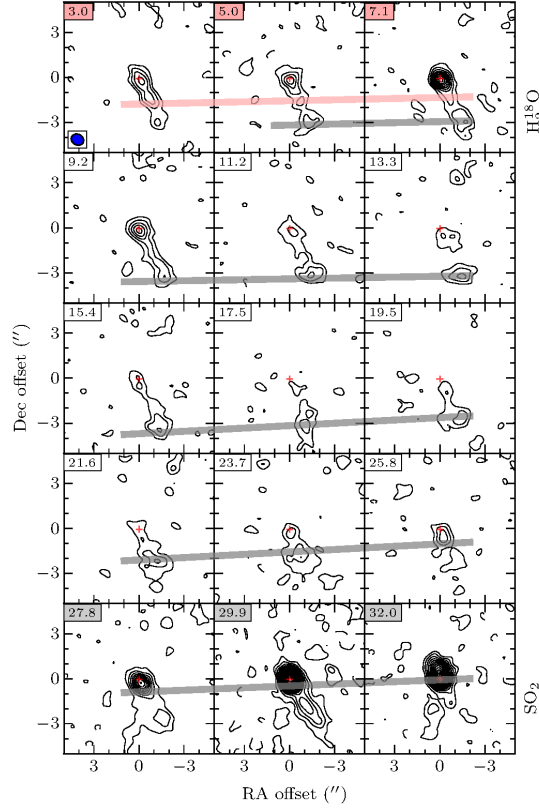


Figure 4.4: Continuum subtracted channel map between 2 and 33 km s⁻¹ for IRAS2A, velocity in km s⁻¹ given in each frame, channel width is 2.1 km s⁻¹. Contours in steps of 3 σ (24 mJy beam⁻¹ km s⁻¹) from a 3 σ level. The beam size is given in the lower left corner of the first frame. Gray and red broad lines trace the different outflow components of SO₂ and H₂¹⁸O, respectively .

4.7.2 Water associated with the outflow in IRAS2A

Whereas the bulk of the H₂¹⁸O emission toward the three sources is associated with the central protostellar component, some extended emission at the velocity of the H₂¹⁸O line is seen extending toward the southwest in the integrated intensity map for IRAS2A (Figure 4.2). Previous observations of IRAS2A have shown that it is oriented such that the outflow lobe extending in the SW direction is blueshifted (Jørgensen et al. 2004, 2007).

To investigate this emission further, continuum subtracted channel maps between 2 and 33 km s⁻¹, integrated in steps of 2.1 km s⁻¹, are shown in Figure 4.4. Starting at the higher velocities, corresponding to SO₂ emission in Figure 4.1, strong on-source emission is seen, but also the extended outflow emission. The gray lines trace the rough position of the peak outflow emission in the frames 5.0 to 32.0 km s⁻¹, corresponding to a linear velocity gradient characteristic for outflow affected material: the peak of the emission in each frame moves further away along the outflow when moving to more blue-shifted velocities. At 19.5 km s⁻¹ the knot identified as SO₂ has moved about 3'' away from the central source. The knot persists at this position (3''~4'' away) almost throughout the rest of the maps and at a velocity of 5.0–7.1 km s⁻¹ it weakens. At 9.2 km s⁻¹ emission is seen to emerge close to the protostar, which is

identified as H_2^{18}O . It strengthens slightly and moves away from the source with lower velocities. Just as with the SO_2 emission it can be traced, although over a smaller number of channels and spatial extent (red line). The outflow water emission is extended and weak, but shows that water is present in the outflow of IRAS2A.

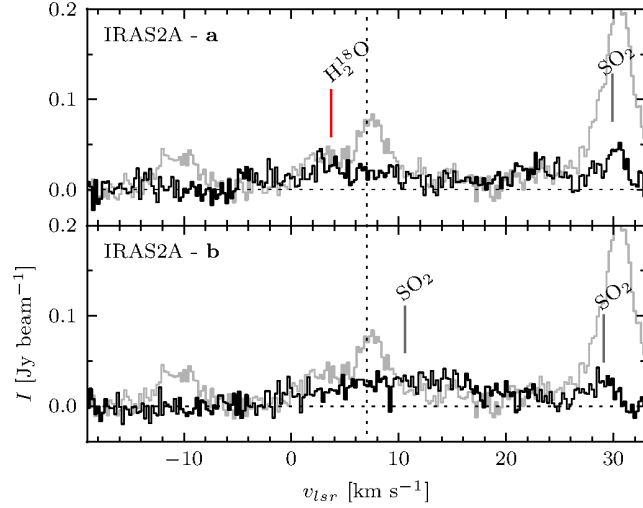


Figure 4.5: IRAS2A off-position spectra, averaged over $1'' \times 1''$ regions around the positions marked with **a** and **b** in Figure 4.2 in the blueshifted outflow from the imaged data. The spectra have been rebinned to twice the velocity resolution (width of 0.23 km s^{-1}). The systemic velocity of the H_2^{18}O line is drawn with a vertical dotted line at $v_{\text{lsr}} = 7 \text{ km s}^{-1}$, and the gray outline in the background is the on-source spectrum averaged in a region of the same size as the other spectra.

The detection of extended outflow H_2^{18}O and SO_2 emission is further strengthened when looking at spectra at different positions in the outflow. Spectra extracted at two positions (averaged over $1'' \times 1''$ regions) from the low surface brightness material in the outflow are shown in Figure 4.5. In Figure 4.2 the positions are marked with **a** (magenta cross) and **b** (green cross). Outflow position **a** shows one SO_2 component with a weak blue tail and a broad H_2^{18}O component that is blueshifted $4\text{--}6 \text{ km s}^{-1}$ from the rest velocity. This blueshift coincides with the velocity of the CH_3OCH_3 lines 3 and 4, but the absence of the CH_3OCH_3 lines 1 and 2, which are detected in the on-source spectra, shows that it is indeed H_2^{18}O . At position **b** only SO_2 with a broad blueshifted component and a narrow component is visible.

Thus the extended outflow emission seen toward IRAS2A in Figure 4.2 is at least partly blueshifted H_2^{18}O in the inner part, close to the source and SO_2 in the outermost part of the outflow.

4.7.3 Constraints on geometry and dynamics

Watson et al. (2007) suggested that the difference between IRAS4A and IRAS4B could be attributed to either hot water only being detectable during a short phase of the life cycle of YSOs or alternatively a particularly favorable line of sight in that system. Because of the lower dust opacity, protostellar envelopes are optically thin at submillimeter wavelengths, which allows detections of the water emission lines from the smallest scales toward the center of the protostars. The detections toward three of three targeted sources (Jørgensen & van Dishoeck 2010b, and this paper) therefore argue against the first of these suggestions.

The detected velocity gradient in IRAS4B – which is absent in the other sources (Figure 4.2) – may be a geometrical effect. A simple solution could be that the sources without a velocity gradient are observed close to face-on. This would require that IRAS4B with its detected velocity gradient is observed edge-on, however. This is not supported by observations of the outflows (Jørgensen et al. 2007): all three sources show well-separated red and blue outflow cones suggesting at least some inclination of the outflows relative to the line-of-sight. Also, of the three sources, IRAS4B in fact shows the most compact outflow: if one assumes similar extents of the outflows this would suggest that IRAS4B rather than the other sources are seen more close to face-on.

Another way to deduce the inclination of the outflow with respect to the plane of the sky is through observations of maser spots in the outflows of the sources, although they do not seem to agree with observations of the larger scale outflow in many cases. Marvel et al. (2008) conclude that in IRAS4A-NW, the maser emission cannot be directly associated with the large scale outflow. For IRAS4B the masers have been associated with the outflow (Marvel et al. 2008; Desmurs et al. 2009), but the position angle of the “maser outflow” still differs from that of the CO outflow by some 20–30°.

We propose that the compact H_2^{18}O emission has its origin in a flattened disk-like structure where inward motions is still dominating the dynamics, and where the viewing angle defines the observational characteristics (Figure 4.6 for a schematic drawing). In fact, Brinch et al. (2009) suggest, based on modeling of submillimeter observations, that IRAS2A indeed has such a structure on a few 100 AU scales. Observing a source with this structure at different viewing angles would potentially produce the observed differences.

In the proposed solution, IRAS4B is viewed at an angle, closer to face-on, causing the mid-IR emission observed by *Spitzer* to escape from the envelope through the cavities produced by the outflow, where the optical depth along the line of sight is lower in agreement with the suggestion by Watson et al. (2007) (case A in Figure 4.6). In IRAS2A and IRAS4A-NW, the viewing angle is closer to edge-on, causing mid-IR emission to be blocked by the optically thick envelope (case B in Figure 4.6).

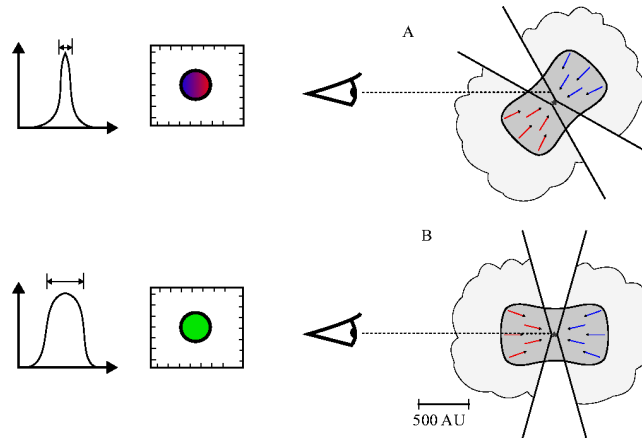


Figure 4.6: Schematic drawing of a disk dominated by inward motions rather than rotation in different observation geometries. In *case A* (IRAS4B), the observed line is narrow and a small velocity gradient is seen. In *case B* (IRAS2A and IRAS4A-NW), the observed line is broader and no velocity gradient is observed.

This solution could also explain the velocity gradient observed toward IRAS4B and the broader line widths toward IRAS2A and IRAS4A-NW. In disks dominated by inward motions rather than rotation, the systems viewed at an angle exhibit narrow lines and a velocity gradient (case A in Figure 4.6), while systems viewed edge on show broader lines and no velocity gradient (case B in Figure 4.6). The

dynamical structure of the disk would move toward a rotationally supported disk on a local dynamical time-scale, which is a few $\times 10^3$ yr at a radius of 110 AU (Brinch et al. 2009).

4.7.4 Non-masing origin of H_2^{18}O emission

We now turn the attention to chemical implications of the presented data: the subsequent analysis of the data focuses on the abundance and excitation of water and other species detected in the spectra.

The primary concern about the H_2^{18}O analysis in this context is whether the H_2^{18}O line could be masing. Many lines of water observable from the ground are seen to be masing, as is the case for the same transition studied here ($3_{1,3} - 2_{2,0}$) but in the main isotopologue, H_2^{16}O (Cernicharo et al. 1994). Several observables argue against that the H_2^{18}O $3_{1,3} - 2_{2,0}$ line is masing in the sources investigated here.

First, the line widths observed in the central beam toward the continuum peak are comparable for all the detected species in each of the sources, as was also seen in IRAS4B (Jørgensen & van Dishoeck 2010b,a). Although the mean line width is somewhat broader in IRAS2A and IRAS4A-NW compared to IRAS4B they are still significantly more narrow toward the central source ($< 5 \text{ km s}^{-1}$) than in the broad outflow components seen in the *Herschel* data ($> 5 \text{ km s}^{-1}$) toward these sources (Kristensen et al. 2010). For IRAS2A, the mean FWHM and standard deviation of the fitted lines is $2.8 \pm 0.7 \text{ km s}^{-1}$, for IRAS4A-NW $2.4 \pm 1.0 \text{ km s}^{-1}$, and for IRAS4B $1.1 \pm 0.2 \text{ km s}^{-1}$. In addition to this, the variations in intensities between the different lines in each source are smaller than the variations in line intensity between the sources.

In IRAS2A, Furuya et al. (2003) report that maser emission at 22 GHz is highly variable and has a velocity of 7.2 km s^{-1} , i.e. marginally red-shifted. For IRAS4A, Furuya et al. (2003) and Marvel et al. (2008) show that the strongest maser component lies at $\sim 10 \text{ km s}^{-1}$ where we do not detect any strong H_2^{18}O millimeter emission.

Taken together, these arguments suggest that the H_2^{18}O emission detected toward the central positions of the sources is not masing, but instead is thermal emission with the same origin as the other detected species.

4.7.5 Column densities and abundances determinations

Having established that the H_2^{18}O line is unlikely to be masing, the column densities for each species can be determined and compared directly. The emission from the different molecules is assumed to be optically thin and to uniformly fill the beam (valid since the deconvolved size in Table 4.3 is comparable to the beam size). The excitation is taken to be characterized by a single excitation temperature T_{ex} , which does not have to be equal to the kinetic temperature.

Water column density and mass

Table 4.4 summarizes the inferred column densities of the various molecules assuming $T_{\text{ex}}=170 \text{ K}$. The gas-phase H_2O abundance and mass are calculated with an isotopic abundance ratio of $^{16}\text{O}/^{18}\text{O}$ of 560 in the local interstellar medium (Wilson & Rood 1994). The masses of gas phase H_2O in the sources are given in the bottom of Table 4.4, in units of Solar and Earth masses, along with the fraction of gas phase water relative to H_2 . As pointed out by Jørgensen & van Dishoeck (2010b), in IRAS4B, the derived column density of H_2O is almost 25 times higher than deduced by Watson et al. (2007). The deduced mass of the gas phase water in IRAS2A is roughly six times higher than in IRAS4A-NW and 90 times higher than in IRAS4B. Thus, water is present in the inner parts of all of the sources and the non-detection in IRAS4A and IRAS2A at mid-infrared wavelengths is due to the high opacity of the envelope combined with a strong outflow contribution to H_2^{16}O lines in IRAS4B (see also Herczeg et al. 2012).

	IRAS2A	IRAS4A-NW	IRAS4B
$N_{\text{CH}_3\text{OCH}_3}^a$	1.2×10^{17b}	6.8×10^{16}	5.6×10^{16}
$N_{\text{H}_2^{18}\text{O}}^a$	2.9×10^{16}	7.9×10^{15}	3.9×10^{15}
$N_{\text{C}_2\text{H}_5\text{CN}}^a$	$< 1.4 \times 10^{14}$	1.1×10^{15}	2.8×10^{14}
$N_{\text{SO}_2}^a$	1.8×10^{16}	8.2×10^{15}	1.3×10^{15}
$M_{\text{H}_2\text{O}} (M_\odot)$	1.8×10^{-6}	2.7×10^{-7}	1.5×10^{-8}
$M_{\text{H}_2\text{O}} (M_\oplus)$	0.61	0.09	0.006
$X (=N_{\text{H}_2\text{O}}/N_{\text{H}_2})$	4.2×10^{-6}	1.4×10^{-7}	7.8×10^{-9}

(*a*) In cm^{-2} assuming $T_{\text{ex}}=170$ K. The typical error is a combination of the assumption of the excitation temperature and the flux calibration uncertainty ($\sim 20\%$). The determined column density varies with T_{ex} in the interval 100–200 K differently for each molecule, see Figure 4.8 and the discussion in Sect. 4.7.5. (*b*) Using only lines 1, 2, 3 and 4.

Table 4.4: Derived properties of the detected species over the deconvolved sizes of the lines for all sources in the project.

The ratio of H_2O gas phase abundance to the total H_2 abundance (derived from continuum observations (Jørgensen et al. 2009)) in Figure 4.7 shows that the fractional abundance of gas phase water in IRAS2A is much higher than in IRAS4A-NW and IRAS4B. Still, the gas-phase water likely accounts for only a small fraction of the total amount of water (gas+ice) on those scales. Typical H_2O to H_2 abundance ratios of $10^{-5} - 10^{-4}$ have been deduced in shocked regions close to protostars (Harwit et al. 1998; Nisini et al. 1999), and in ices in the cold outer parts of protostellar envelopes (Pontoppidan et al. 2004). In shocks, high temperature gas-phase reactions drive much of the oxygen into water (Draine et al. 1983). In more quiescent regions the ice is expected to evaporate off the grains when heated to temperatures above 100 K in close proximity to the central source (Fraser et al. 2001). The fact that our inferred abundance ratios are generally much lower than 10^{-4} suggests that a large fraction of the dust mass in the inner ~ 100 AU has a temperature below 100 K, with the fraction varying from source to source. In colder regions, most of the water gas originates from UV photodesorption of ices. Assuming a total H_2O to H_2 abundance ratio of 10^{-4} (gas+ice), the fraction of water in the gas phase is 4% for IRAS2A, 0.1% for IRAS4A-NW and 0.01% for IRAS4B of the total water content (gas+ice). This difference could be due, for example, to varying intensities of the UV radiation from the newly formed stars and geometry causing differences in the relative amounts of material heated above the temperature where water ice mantles are evaporated. Toward the more evolved Class II source TW Hydra, Hogerheijde et al. (2011) deduce a gas phase water to total hydrogen abundance of 2.4×10^{-8} using *Herschel*. This value is of the same order of magnitude as our results, and places TW Hydra just above IRAS4B in Figure 4.7.

Other molecules

In the right plot of Figure 4.7, the abundances of the detected molecules relative to H_2O are presented. The CH_3OCH_3 and SO_2 content relative to H_2^{18}O is roughly comparable between the different sources. This suggests that for CH_3OCH_3 , SO_2 and H_2^{18}O (and thus H_2O) similar chemical processes are at work in the three sources. $\text{C}_2\text{H}_5\text{CN}$ is the least abundant of the molecules for all the sources. In IRAS2A the high abundance of water is contrasted by the relatively low abundance of $\text{C}_2\text{H}_5\text{CN}$, for which only an upper limit is deduced. This relatively low abundance in IRAS2A is robust even when much lower excitation temperatures are assumed (see Sect. 4.7.5).

It is also evident from Figure 4.7 and Table 4.4 that the $\text{CH}_3\text{OCH}_3/\text{C}_2\text{H}_5\text{CN}$ column density ratio varies significantly between the sources. This ratio is 10^3 for IRAS2A, 60 for IRAS4A-NW and 200

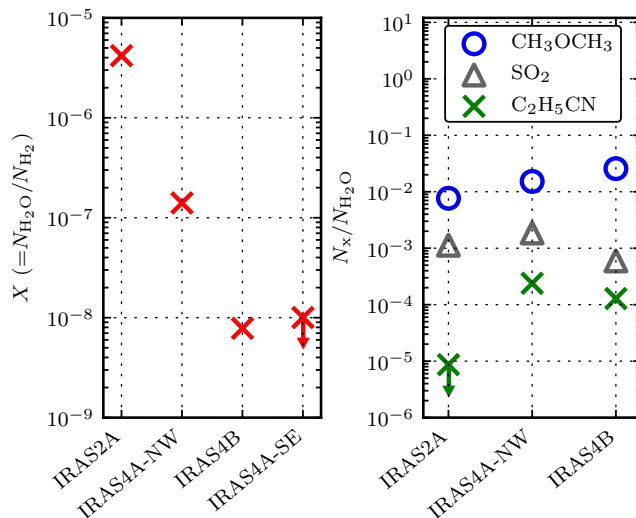


Figure 4.7: *Left:* Fraction of gas phase water relative to H₂ (from the continuum observations of Jørgensen et al. 2009) for the different sources, including an upper limit estimate for IRAS4A-SE. *Right:* Ratio of the column density of the molecules relative to water. The C₂H₅CN value for IRAS2A is an upper limit.

for IRAS4B assuming $T_{\text{ex}}=170$ K. The differences in relative abundances of N and O-bearing complex organics have been interpreted as an indicator for different physical parameters (Rodgers & Charnley 2001) and different initial grain surface composition (Charnley et al. 1992; Bottinelli et al. 2004a). Caselli et al. (1993) argue that the (dust) temperature history of the cloud, in particular whether it was cold enough to freeze out CO, is an important factor for the resulting ratio.

Effect of excitation temperature

The results presented in previous sections assume an excitation temperature of 170 K for all species. In this section we demonstrate that all our conclusions are robust over a wide range of assumed temperatures. The adopted $T_{\text{ex}}=170$ K is the same as found from the model fit to the mid-infrared water lines observed by *Spitzer* (Watson et al. 2007) and allows for easy comparison to this paper and Jørgensen & van Dishoeck (2010b).

Although the origin of the mid-infrared and millimeter lines are likely not the same, this temperature is a reasonable first guess appropriate of the conditions in the inner 150 AU of protostellar systems. From modeling of dust continuum observations, the density in the inner envelope/disk is found to be high, at least 10^7 cm⁻³, and the dust temperature is thought to be at least 90 K for a fraction of the material (e.g., Jørgensen et al. 2002, 2004). This is also the temperature at which water is liberated from the grains; any gas-phase water detected in the high excitation line observed here ($E_u \approx 200$ K) likely originates from the warmer regions (Sect. 4.7.5).

The current observations and literature data do not provide enough information on the line emission at these scales to constrain the excitation temperature directly. For none of the detected species are there more than two previous measurements and those detections either have large uncertainties due to their weakness (Jørgensen et al. 2005) or are sensitive to larger scale emission including outflow and envelope because of the large beam (Bottinelli et al. 2004a, 2007; Wakelam et al. 2005). For the deeply embedded low-mass protostar IRAS 16293-2422, Bisschop et al. (2008) derive rotational temperatures between 200–400 K from several compact emission lines of complex molecules using SMA

data. Furthermore, for the outflow toward IRAS4B Herczeg et al. (2012) deduce $T_{\text{ex}}=110\text{--}220$ K with recent *Herschel* PACS data.

Figure 4.8 explores what happens with the column densities at significantly different excitation temperatures than those assumed here. It shows two different plots for the three sources. The plots in the top row show the ratio between the column density of the various molecules and that of water, whereas the plots in the bottom row show the column densities themselves, all as functions of excitation temperature. The ratios ($N_X/N_{\text{H}_2\text{O}}$) do not change significantly between 100 and 275 K. The gray area in the lower plots shows the range of excitation temperatures for which the column density of water is the same in the three sources. Only if the excitation temperature in IRAS4A-NW and IRAS4B is lower than 50 K can all sources have comparable water column densities based on the observed intensities.

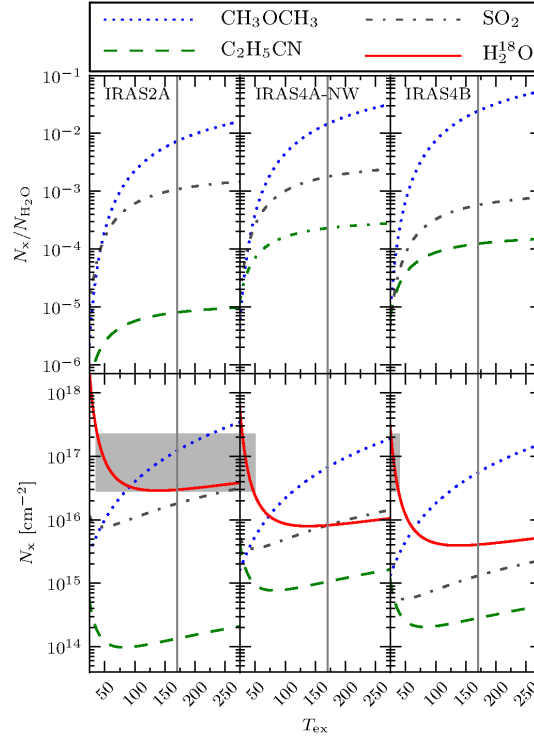


Figure 4.8: Plots showing (*upper*) the ratio between the detected molecules and water (H_2O), assuming that the species have the same T_{ex} and (*lower*) the column density of all the detected lines (including H_2^{18}O). The colors and line style indicate the different molecules, the gray vertical line mark $T_{\text{ex}}=170$ K and the gray area in each plot indicate the temperatures where the column density of H_2^{18}O is the same for the sources.

The different molecules could of course each have different excitation temperatures. Specifically, can different excitation temperatures be the cause of the large range in inferred $\text{CH}_3\text{OCH}_3/\text{C}_2\text{H}_5\text{CN}$ column density ratios? Figure 4.9 shows this ratio and the individual column densities for excitation temperatures from 25 to 275 K for IRAS2A. The corresponding plots for the other two sources show similar trends (see also Figure 4.8). The temperature does not affect the column density estimate for $\text{C}_2\text{H}_5\text{CN}$ significantly, showing that our upper limit estimate is rather robust, and that the differences in this ratio between the sources cannot be attributed to differences in the excitation of $\text{C}_2\text{H}_5\text{CN}$ alone. On the other hand, changing the excitation temperature for CH_3OCH_3 affects the column density and

the ratio to a greater extent. This difference in behavior with T_{ex} for the two molecules is caused by the transitions' upper energy levels (E_u); 18 K for CH_3OCH_3 versus 122 K for $\text{C}_2\text{H}_5\text{CN}$. For CH_3OCH_3 , its lower value of E_u causes the column density estimate to decline more rapidly with T_{ex} than for $\text{C}_2\text{H}_5\text{CN}$: the contribution from the exponent in the Boltzmann distribution ($\exp(-E_u/kT_{\text{ex}})$) does not compensate for the fall that the partition function (proportional to T_{ex}^b , where $b>0$) introduces. In the temperature range 40 to 250 K the $\text{CH}_3\text{OCH}_3/\text{C}_2\text{H}_5\text{CN}$ column density ratio varies with a factor of about 30. Looking only at the $\text{CH}_3\text{OCH}_3/\text{C}_2\text{H}_5\text{CN}$ column density ratio, the excitation temperature for IRAS2A has to be $T_{\text{ex}}=45$ K, and for IRAS4B $T_{\text{ex}}=85$ K, to match that of IRAS4A-NW.

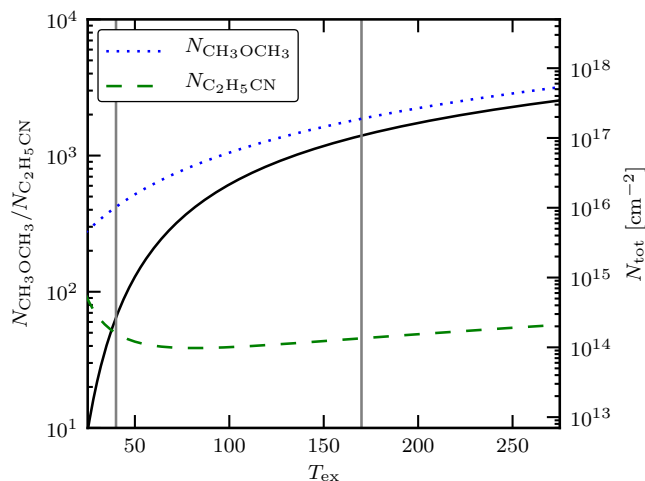


Figure 4.9: Plot of the ratio between CH_3OCH_3 and $\text{C}_2\text{H}_5\text{CN}$ in IRAS2A (left y -axis, filled line), and the column densities derived for those molecules (right y -axis, dashed/dash dotted line) for temperatures between 25 and 275 K. The vertical lines show $T=40$ and 170 K.

As argued above based on the physical characteristics of the sources, values of T_{ex} significantly below 100 K and large differences in T_{ex} between molecules and sources are not expected on the scales probed here. Also, the agreement in widths, extent and positions between the lines argues against this. If the temperature is allowed to vary in the range 100-250 K the conclusions drawn in this paper are unchanged.

4.7.6 Formation of molecules in the protostellar environment

The simultaneous observations of water and the complex molecules can also be used to shed new light onto where and how the formation of various molecules takes place in the protostellar environment. The basic scenario is that many of the complex organic molecules are formed as a result of grain-surface reactions during the collapse of the protostellar envelopes as material is heated slowly (see Herbst & van Dishoeck 2009, for a review).

Garrod & Herbst (2006) use a gas-grain network of reactions to investigate the formation of certain complex organic molecules in hot cores and corinos during the warm-up and evaporative stages. The results show that the chemistry occurs both on grain surfaces and in the gas phase, with the two phases being strongly coupled with each other. Large abundances of complex organic molecules are present at the end of this warm-up stage, and show that a period of $10^4 - 10^5$ years is vital for the formation of complex molecules.

A key question is thus whether the material in these low-mass protostars spends enough time at moderate temperatures of 20–40 K to form complex organic molecules during the collapse of the cloud and formation of the disk. A parcel of material originating in the cold core will pass through the warm inner envelope during the collapse and be incorporated into the disk before being accreted onto the star. Depending on its precise origin, the material can follow many different routes, but exploration of a variety of collapse models shows that most parcels indeed spend the required period at moderate temperatures to form the complex organics, either in the inner envelope or in the disk (Visser et al. 2009). Some of the routes result in the material being directly exposed to UV radiation near the outflow cavity walls (Visser et al. 2011). After evaporation, gas-phase temperatures in the hot core are generally too low (i.e., $T \lesssim 230$ K, $R \gtrsim 20$ AU, Larson 1972; Jørgensen et al. 2002) for any significant gas-phase formation of water to take place. The fact that we observe narrow emission lines of complex molecules on small scales confirms that some fraction of the collapsing cloud has spent enough time under conditions that lead to the formation of complex species that will enter the disk.

4.8 Summary and Outlook

We have presented subarcsecond resolution observations of the H_2^{18}O $3_{1,3} - 2_{2,0}$ transition at 203.4 GHz toward a small selection of deeply embedded protostars in the NGC 1333 region. In addition to the targeted H_2^{18}O molecule, SO_2 and complex organic molecules are seen.

- Water is successfully detected toward IRAS2A and one component of the IRAS4A binary. These data add to the previous detection of the $3_{1,3} - 2_{2,0}$ transition of H_2^{18}O toward IRAS4B by Jørgensen & van Dishoeck (2010b). The origin of the emission differs from that seen with both *Herschel* and *Spitzer*, where larger-scale emission (protostellar envelope, outflow shocks/cavity walls) is detected.
- The gas-phase water abundance is significantly lower than a canonical abundance of 10^{-4} , suggesting that most water is frozen out on dust grains at these scales. The fraction of water in the gas phase is 4% for IRAS2A, 0.1% for IRAS4A-NW and 0.01% for IRAS4B of the total water content (gas+ice).
- IRAS2A shows H_2^{18}O emission not only at the source position, but also in the blueshifted outflow. In IRAS4A we only detect water toward IRAS4A-NW. None of the lines presented for the other sources are detected toward IRAS4A-SE.
- Based on the small species-to-species variations, in both line strength and line width, we argue that the H_2^{18}O $3_{1,3} - 2_{2,0}$ emission line is not masing in these environments and on these scales.
- While IRAS4B shows narrow emission lines and a tentative velocity gradient, reported by Jørgensen & van Dishoeck (2010b), the other sources show broader lines and no velocity gradients. Additionally, IRAS4B is the only source of the three detected in mid-infrared water lines by Watson et al. (2007). We propose that a disk-like structure dominated by inward motions rather than rotation with different orientations with respect to the observer could explain the observed line characteristics.
- The abundances of the detected molecules differ between the sources: the abundance of $\text{C}_2\text{H}_5\text{CN}$ with respect to water, compared to both SO_2 and CH_3OCH_3 , is much lower in IRAS2A than the other sources. This shows that the formation mechanism for $\text{C}_2\text{H}_5\text{CN}$ is different from the other molecules, indicating that it is not trapped in the water ice mixture or related to the sublimation of water.

The detections of H_2^{18}O emission from the ground show good promise for using H_2^{18}O as a probe of the inner regions of protostars and for studying the formation of complex organic molecules in the water-rich grain ice mantles. Higher resolution observations, using the PdBI in the most extended

configuration, or with the Atacama Large Millimeter/submillimeter Array (ALMA) band 5 could be used to reveal the kinematical structure on 10–100 AU scales and the dynamics of the forming disks. Observations of higher excited lines of H_2^{18}O and the complex organics in other ALMA bands (e.g., band 8) could provide a better handle on the excitation conditions of water on a few hundred AU scales in the centers of protostellar envelopes. Finally, observing more protostellar sources in the H_2^{18}O $3_{1,3} - 2_{2,0}$ transition would provide a better statistical sample for comparisons and conclusions.

We wish to thank the IRAM staff, in particular Arancha Castro-Carrizo, for her help with the observations and reduction of the data. The research at Centre for Star and Planet Formation is supported by the Danish National Research Foundation and the University of Copenhagen's programme of excellence. This research was furthermore supported by a Junior Group Leader Fellowship from the Lundbeck Foundation to JKJ and by a grant from Instrumentcenter for Danish Astrophysics. This work has benefited from research funding from the European Community's sixth Framework Programme under RadioNet R113CT 2003 5058187. Astrochemistry in Leiden is supported by a Spinoza grant from the Netherlands Organization for Scientific Research (NWO) and NOVA, by NWO grant 614.001.008 and by EU FP7 grant 238258.

4.9 Tables

No.	Molecule	Transition	Rest Freq. (GHz)	E_u (K)	$\log A_{ij}$ ($\log s^{-1}$)
1	CH_3OCH_3	$3_{3,0} - 2_{2,1}$ EE	203.4203	18.1	-4.61
2	CH_3OCH_3	$3_{3,0} - 2_{2,1}$ AA	203.4187	18.1	-4.23
3	CH_3OCH_3	$3_{3,0} - 2_{2,1}$ AE	203.4114	18.1	-4.23
4	CH_3OCH_3	$3_{3,1} - 2_{2,1}$ EE	203.4101	18.1	-4.46
5	H_2^{18}O	$3_{1,3} - 2_{2,0}$	203.4075	203.7	-5.32
6	CH_3OCH_3	$3_{3,1} - 2_{2,1}$ EA	203.4028	18.1	-4.39
7	$\text{C}_2\text{H}_5\text{CN}$	$23_{2,22} - 22_{2,21}$	203.3966	122.3	-3.15
8	SO_2	$12_{0,12} - 11_{1,11}$	203.3916	70.1	-4.07

Table 4.5: Tabulated data for the different lines detected from JPL (Pickett et al. 1998) and CDMS (Müller et al. 2001).

No.	Molecule	IRAS2A			IRAS4A-NW		
		Position (km s ⁻¹)	Width (km s ⁻¹)	Interval ^a (km s ⁻¹)	Position (km s ⁻¹)	Width (km s ⁻¹)	Interval ^a (km s ⁻¹)
1	CH ₃ OCH ₃	-11.7 ± 0.1	2.3 ± 0.1	-14.0 - -7.0	-11.3 ± 0.1	1.6 ± 0.1	-13.0 - -7.3
2	CH ₃ OCH ₃	-9.3 ± 0.1	2.3 ± 0.1	-	-9.0 ± 0.1	1.6 ± 0.1	-
3	CH ₃ OCH ₃	+1.3 ± 0.1	2.3 ± 0.1	-1.0 - +4.4	+1.7 ± 0.1	1.6 ± 0.1	0.0 - +4.7
4	CH ₃ OCH ₃	+3.2 ± 0.1	2.3 ± 0.1	-	+3.6 ± 0.1	1.6 ± 0.1	-
5	H ₂ ¹⁸ O	+7.4 ± 0.1	4.0 ± 0.1	+4.4 - +11.4	+6.6 ± 0.1	2.9 ± 0.3	+4.7 - +9.6
6	CH ₃ OCH ₃	+15.2 ± 0.2	2.3 ± 0.1	+12.9 - +17.5	+14.4 ± 0.1	1.6 ± 0.1	+12.0 - +15.2
7	C ₂ H ₅ CN	-	-	-	+22.8 ± 0.2	3.8 ± 0.4	+19.0 - +26.9
8	SO ₂	+30.4 ± 0.1	3.8 ± 0.1	+26.6 - +33.9	+30.4 ± 0.1	4.1 ± 0.2	+26.9 - +34.6

^(a) Interval over which the integrated line intensity (Table 4.3) is estimated.

Table 4.6: Position and FWHM of the detected lines from Gaussian fits to the spectra.

Paper II

Warm water deuterium fractionation in IRAS 16293-2422 – The high-resolution ALMA and SMA view

M. V. Persson^{1,2}, J. K. Jørgensen^{2,1} and E. F. van Dishoeck^{3,4}

¹ Centre for Star and Planet Formation, Natural History Museum of Denmark, University of Copenhagen, Øster Voldgade 5-7, DK-1350, Copenhagen K, Denmark

² Niels Bohr Institute, University of Copenhagen, Juliane Maries Vej 30, DK-2100 Copenhagen Ø, Denmark

³ Leiden Observatory, Leiden University, P.O. Box 9513, NL-2300 RA Leiden, The Netherlands

⁴ Max-Planck Institute für extraterrestrische Physik (MPE), Giessenbachstrasse, 85748 Garching, Germany

Appeared in *Astronomy & Astrophysics* Year 2013, Volume 549

ABSTRACT

Context Measuring the water deuterium fractionation in the inner warm regions of low-mass protostars has so far been hampered by poor angular resolution obtainable with single-dish ground- and space-based telescopes. Observations of water isotopologues using (sub)millimeter wavelength interferometers have the potential to shed light on this matter.

Aims To measure the water deuterium fractionation in the warm gas of the deeply-embedded protostellar binary IRAS 16293-2422.

Methods Observations toward IRAS 16293-2422 of the $5_{3,2} - 4_{4,1}$ transition of H_2^{18}O at 692.07914 GHz from Atacama Large Millimeter/submillimeter Array (ALMA) as well as the $3_{1,3} - 2_{2,0}$ of H_2^{18}O at 203.40752 GHz and the $3_{1,2} - 2_{2,1}$ transition of HDO at 225.89672 GHz from the Submillimeter Array (SMA) are presented.

Results The 692 GHz H_2^{18}O line is seen toward both components of the binary protostar. Toward one of the components, “source B”, the line is seen in absorption toward the continuum, slightly red-shifted from the systemic velocity, whereas emission is seen off-source at the systemic velocity. Toward the other component, “source A”, the two HDO and H_2^{18}O lines are detected as well with the SMA. From the H_2^{18}O transitions the excitation temperature is estimated at 124 ± 12 K. The calculated HDO/ H_2O ratio is $(9.2 \pm 2.6) \times 10^{-4}$ – significantly lower than previous estimates in the warm gas close to the source. It is also lower by a factor of ~ 5 than the ratio deduced in the outer envelope.

Conclusions Our observations reveal the physical and chemical structure of water vapor close to the protostars on solar-system scales. The red-shifted absorption detected toward source B is indicative of infall. The excitation temperature is consistent with the picture of water ice evaporation close to the protostar. The low HDO/ H_2O ratio deduced here suggests that the differences between the inner regions of the protostars and the Earth’s oceans and comets are smaller than previously thought.

4.10 Introduction

Water plays an essential role for life as we know it, but its origin on Earth is still unclear: was water accreted during the early stages of Earth’s formation, or brought by smaller solar system bodies such as comets at later times? To deduce the origin of Earth’s water and the amount of chemical processing it has experienced, one option is to measure the water deuterium fractionation (HDO/ H_2O) during different stages in the evolution of protostars and compare it to what we measure in Earth’s oceans and comets.

Generally the HDO/ H_2O ratio in Earth’s oceans of 3×10^{-4} (e.g., Lécuyer et al. 1998) and Oort cloud comets of 8.2×10^{-4} (Villanueva et al. 2009) are found to be enhanced above the D/ H^3 ratio in the

³A HDO/ H_2O ratio of “ x ” corresponds to a D/H ratio of “ $x/2$ ”.

protosolar nebula $\sim 1.5 \times 10^{-5}$ (Linsky 2003; Geiss & Gloeckler 1998) due to deuterium fractionation processes. The factor of 2 higher abundance ratio in the Oort cloud comets than in Earth’s oceans has previously been taken as an indication that only a small fraction of Earth’s water was delivered by comets. Recently however, a HDO/H₂O ratio of 3.2×10^{-4} was measured for the Jupiter class comet Hartley 2 with the *Herschel* Space Observatory (Hartogh et al. 2011) and 4.2×10^{-4} for the Oort cloud comet Garradd (Bockelée-Morvan et al. 2012), indicating values closer to those of Earth’s water.

Attempts at measuring the water deuterium fractionation in protostars have resulted in different conclusions. Parise et al. (2003) used ground-based infrared observations of the stretching bands of OH and OD in water ice in the outer parts of envelopes and found *upper limits* ranging from 0.5% to 2% for the HDO/H₂O ratios in four embedded low-mass protostars. In the gas-phase it is possible to detect lines of HDO, but such studies differ on the interpretation with HDO/H₂O ratios in protostars ranging from cometary values (Stark et al. 2004), to a few % (Parise et al. 2005; Liu et al. 2011). Even more recently, Coutens et al. (2012) deduced a HDO/H₂O ratio in IRAS 16293-2422 of 3.4×10^{-2} in the inner parts and 0.5×10^{-2} in the outer envelope by modeling a large range of lines observed with *Herschel*.

One problem with previous measurements of HDO/H₂O is the relatively large beam size of single-dish ground- and space-based telescopes. Spherically symmetric power-law models of protostellar envelopes have usually been employed to interpret the observations. While such models are appropriate to interpret continuum and line emission on larger scales (>300 AU), they are not suited to unambiguously analyze the observed compact components since there are clear indications that they are not an accurate representation of the conditions on small scales (e.g., Jørgensen et al. 2005; Chiang et al. 2012). Estimates of abundance ratios on these smaller scales are thus subject to significant uncertainties due to extrapolations of the underlying physical structures.

High angular resolution millimeter wavelength aperture synthesis observations offer a possibility to circumvent this issue. Recently Jørgensen & van Dishoeck (2010b) detected the water isotopologue H₂¹⁸O toward the deeply embedded protostar NGC-1333 IRAS4B on scales of <50 AU using the IRAM Plateau de Bure Interferometer (PdBI), which combined with an upper limit on the HDO column density from the SMA resulted in a 3σ upper limit to the HDO/H₂O abundance ratio of 6×10^{-4} . To follow-up these results we initiated an extended survey of the H₂¹⁸O and HDO emission on arcsecond scales using the IRAM PdBI and SMA (Persson et al. 2012).

IRAS 16293-2422 is a Class 0 protostellar binary (sep $\sim 5''$, 600 AU) located 120 pc away in the LDN 1689N cloud in the ρ Ophiucus star-forming region (Knude & Hog 1998; Loinard et al. 2008). With a rich spectrum at (sub)millimeter wavelengths (Blake et al. 1994; van Dishoeck et al. 1995; Cazaux et al. 2003; Chandler et al. 2005; Caux et al. 2011; Jørgensen et al. 2011) it has been one of the prime targets for studies of astrochemistry during the star-formation process, revealing the presence of a range of complex organic species (Bottinelli et al. 2004b; Kuan et al. 2004; Bisschop et al. 2008) and prebiotic molecules (Jørgensen et al. 2012) on (sub)arcsecond scales.

In this letter we present, for the first time, *high-resolution* ground-based observations of several isotopologues of water toward IRAS 16293-2422 with both the ALMA ($\sim 0''.2$; 24 AU) and the SMA ($\sim 2''.3$; 276 AU). We derive direct, model-independent estimates of the water excitation temperature and use it to calculate the column density and the HDO/H₂O ratio in the warm inner envelope.

4.11 Observations

Observations of the deeply-embedded low-mass protostellar binary IRAS 16293-2422 were carried out at 690 GHz with ALMA and 230 GHz with the SMA, targeting the $5_{3,2} - 4_{4,1}$ (692.07914 GHz) and $3_{1,3} - 2_{2,0}$ (203.40752 GHz) transitions of H₂¹⁸O and the $3_{1,2} - 2_{2,1}$ (225.89672 GHz) transition of HDO (see Table 4.8 in the appendix/electronic version). In the tables, the 203 GHz observations are indicated with “1”, 225 GHz observations with “2” and 692 GHz with “3” (see Table 4.7 and Table 4.8)

The ALMA observations of IRAS 16293-2422 were conducted as part of the ALMA Science Verification (SV) program: IRAS 16293-2422 was observed with 13 antennas on April 16 and 17, 2012 in a seven pointing mosaic centered at $\alpha = 16^{\text{h}}32^{\text{m}}22^{\text{s}}.7$, $\delta = -24^{\circ}28'32''.5$ (J2000). The observations cover projected baselines from 26 to 402 m (62 to 945 $\text{k}\lambda$). One of the basebands was centered at 691.299 GHz with a bandwidth of 1.875 GHz and a spectral resolution of 0.923 MHz (0.4 km s^{-1}), a setup that covers the H_2^{18}O $5_{3,2} - 4_{4,1}$ line at 692.07914 GHz. Calibration observations include the quasars 1924-292 and 3c279 for the bandpass, the asteroid Juno for the amplitude, and the quasars 1625-254 and nrao530 for the phase. The science verification data are available as calibrated uv -data sets, which were used in our analysis. The calibrated data were imaged using the CASA software package (McMullin et al. 2007).

The lower-lying excited H_2^{18}O $3_{1,3} - 2_{2,0}$ transition at 203.4075 GHz was observed with the SMA on May 1, 2011 in the compact configuration with seven antennas. This configuration resulted in projected baselines between 9 and 69 meters (6 to 47 $\text{k}\lambda$). The passband was calibrated by observations of the quasar 3c279 while the absolute flux and complex gains were calibrated by observing Titan and the quasars 3c279, 1517-243 and 1626-298. The raw data calibration followed the standard recipes using the MIR package (Qi 2008) and then MIRIAD (Sault et al. 1995) was used to subtract the continuum from the data to create continuum-free line maps.

Finally, we utilized SMA observations of the HDO $3_{1,2} - 2_{2,1}$ line at 225.89672 GHz (Jørgensen et al. 2011): those observations have a spectral resolution of 0.41 MHz (0.54 km s^{-1}) and cover the projected baselines between 8.6 – 119.6 m (6.5 – 90 $\text{k}\lambda$). For further information about those observations we refer to Jørgensen et al. (2011). The resulting beam size, field of view, velocity resolution and RMS of the various line data are summarized in Table 4.8 in the appendix/electronic version.

4.12 Results

Figure 4.10 shows the spectra around the water lines toward the continuum peaks with Gaussian fits. Source A is in itself a binary (Chandler et al. 2005) and we here refer to the components as A1 (the Northeast component) and A2 (the Southwest component) and the lower resolution single component as A. Both H_2^{18}O lines are clearly detected toward source A in emission, while only the 692 GHz H_2^{18}O line is seen toward source B in absorption. The H_2^{18}O emission is clearly associated with peak A1 in the 692 GHz data. The H_2^{18}O 692 GHz absorption line toward the continuum peak of source B is narrow and marginally red-shifted; the absorption is not due to the broad outflow seen in some lines (Jørgensen et al. 2011).

This weak absorption feature is not seen in the SMA data but the high sensitivity of ALMA combined with the stronger continuum at high frequencies is enough to detect it. The lines were identified using the JPL and CDMS catalogs through the Splatalogue compilation (Pickett et al. 1998; Müller et al. 2001).

The Splatalogue compilation shows no other possible line candidates at least $\pm 1 \text{ km s}^{-1}$ from the line peak positions of the H_2^{18}O line at 203 GHz and the HDO line at 225 GHz. Lines that fall within $\pm 2 - 3 \text{ km s}^{-1}$ exist, but are of too low intrinsic line strengths or lack additional components that should have been detected at other velocity offsets e.g., $(\text{CH}_3)_2\text{CO}$, $^{13}\text{CH}_3\text{CH}_2\text{CN}$ or C_6H . At 203.403 and 203.410 GHz (i.e., about 10 and -3 km s^{-1}) lies CH_3OCH_3 $3_{3,1} - 2_{2,1}\text{EA/EE}$, which is accounted for when fitting the 203 GHz line. These lines are narrow enough to avoid any significant interference with H_2^{18}O (see top most plot in Fig. 4.10).

For the H_2^{18}O ALMA data at 692 GHz the line identification in source A is complicated by the fact that the source is resolved and shows a systematic velocity pattern in other lines (Pineda et al. 2012). The line toward the continuum position of source A is red-shifted by about 2 km s^{-1} from the systemic v_{LSR} of 3.2 km s^{-1} , similar to lines from other species (see Fig. 4.10, panel four). The third spectrum from the top in Fig. 4.10 shows the spectrum after smoothing with a Gaussian kernel of $1''$ size. The Gaussian fit to these data peaks closer to $v_{LSR}=3.2 \text{ km s}^{-1}$, indicative indeed of resolved

velocity structure. Outflow emission (c.f., Loinard et al. 2013), as also seen in H_2O masers on small scales (Alves et al. 2012), could explain this velocity shift, but it is not possible to deduce its importance from the current data.

However, another possibility is that line blending causes the shift. Toward source B, the off position spectrum shows two emission lines, the second line at $\sim 6 \text{ km s}^{-1}$ is unidentified (bottom spectrum Fig.4.10). The H_2^{18}O line at 692 GHz toward source A may therefore also be affected by line blending. However, the unambiguous detection of the 692 GHz line toward source B and the SMA observations of water toward source A suggest that at least half of the 692 GHz feature toward source A is indeed due to the H_2^{18}O line.

Table 4.7 lists parameters from Gaussian fits to the image and uv -plane of the line emission. The integrated intensity maps for the detected water lines are shown in Fig. 4.11.

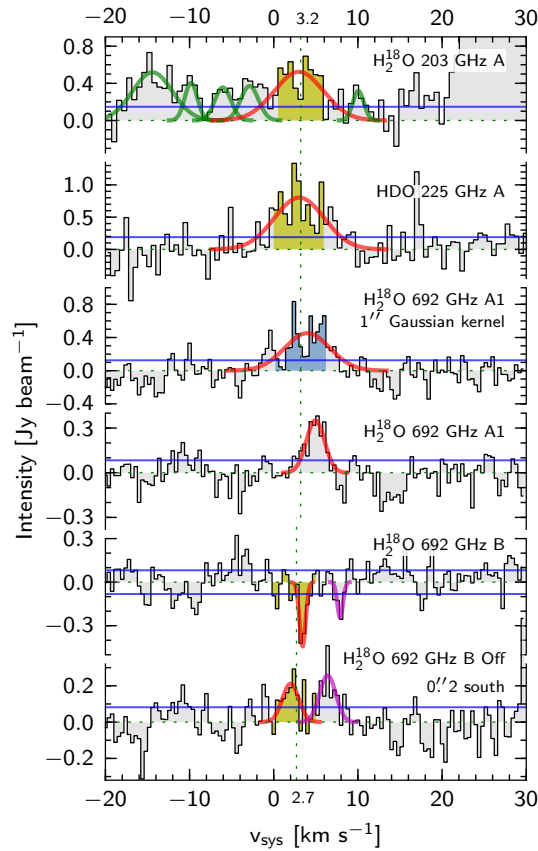


Figure 4.10: Spectra of the targeted water lines toward both IRAS 16293-2422 A and B. The 203 GHz H_2^{18}O line spectrum (top) was binned to twice the resolution for clarity. The 1D Gaussian fits (red: H_2^{18}O ; green: CH_3OCH_3 ; magenta: Unidentified) and the RMS (blue) are plotted. Shaded areas show the interval over which the integrated intensities have been calculated (yellow and blue). The dotted green vertical lines shows $v_{\text{LSR}} = 3.2$ and 2.7 km s^{-1} for source A and B respectively. The third spectrum from the top (blue fill) is from data smoothed with a $1''$ Gaussian kernel.

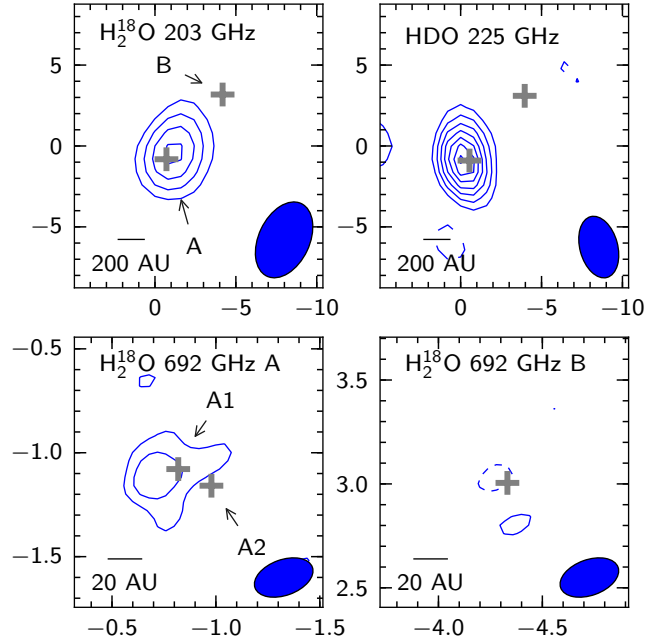


Figure 4.11: Integrated intensity maps for all observed water lines calculated from channels ± 3 from the systemic velocity, deduced from previous observations (Jørgensen et al. 2011). The absorption line toward source B was integrated in the interval $0 - 5 \text{ km s}^{-1}$. Note the different spatial scales of the top vs the bottom panels. The beam is shown in the lower right corner and the gray crosses show the position of continuum peaks from elliptical Gaussian fits. Units on the axes are offset in arcseconds from the phase center of the 203 GHz observations. Contours are in steps of 2σ starting at 3σ , dashed contours represent negative values.

4.13 Discussion

4.13.1 Spectra and integrated intensity

The different water lines toward source A show similar characteristics. The peak positions and line widths of the Gaussian fits to the 203 GHz H_2^{18}O and 225 GHz HDO lines are similar and agree with previous studies of other molecules toward IRAS 16293-2422 e.g., Bisschop et al. (2008); Jørgensen et al. (2011); Jørgensen et al. (2012); Pineda et al. (2012) (see Table 4.7). The mapped emission is compact and traces the warm water on scales $R < 200 \text{ AU}$.

Toward source B, the 692 GHz H_2^{18}O line is detected in absorption. The spectral line is slightly red-shifted compared with $v_{\text{LSR}} = 2.7 \text{ km s}^{-1}$ of source B, consistent with the picture of ongoing infall in this source (Jørgensen et al. 2012; Pineda et al. 2012). Integrating over a larger velocity interval reveals, in addition to the absorption, a blue-shifted emission peak, offset $\sim 0''.2$ south of the absorption (see Fig. 4.10 and 4.11).

4.13.2 Temperature and deuteration of water vapor

To calculate the excitation temperature and column densities toward source A we assume LTE conditions and that the emission at 203 and 225 GHz has the same extent as in the 692 GHz observations (see Table 4.7). Scaling the 203 GHz H_2^{18}O intensities to the 692 GHz source size gives an excitation

Line Id	Size ["]	Intensity [Jy km s ⁻¹]	Line width [km s ⁻¹]
1 (A)	1.7 ± 0.7	3.9 ± 1.4	6.9 ± 1.5
2 (A)	1.1 ± 0.4	8.9 ± 1.8	7.0 ± 0.7
3 (A1)	0.2 × 0.4 (13°)	3.4 ± 0.6	6.3 ± 0.7
3 (B)	Point fit	-0.43 ± 0.07	0.9 ± 0.2

Notes. The column “Line Id” gives the source indicated in parentheses, and the number corresponds to one of the lines (see text and Table 4.8). The line width is the FWHM from a Gaussian fit to the spectral line. The elliptical Gaussian parameters (for line 3 (A1)) are given as minor and major axis ($\pm 0''.1$) and position angle (PA, $\pm 4^\circ$).

Table 4.7: Parameters from fits to the integrated maps and spectra of the different water lines for source A and B. The given errors are the statistical uncertainties and the 20% calibration uncertainty in intensity is not included. The spectral line fits were done toward the continuum peak and integrated intensities deduced from circular Gaussian fits in the uv -plane (203 and 225 GHz) or an elliptical Gaussian fit in the image plane (692 GHz).

temperature of $T_{\text{ex}} = 124 \pm 12$ K for H_2^{18}O . If the 692 GHz line is indeed blended, it would imply that the intensity estimate, and also the excitation temperature, are upper limits. Halving the intensity of the 692 GHz line causes a drop to $T_{\text{ex}} = 107 \pm 9$ K. The extent and peak location of the emission in source A show that the warm water vapor is located at a small projected distance from the center of the protostar. The determined excitation temperature indicates that the distance is also small along the line of sight.

The estimated HDO column density is $4.8 \times 10^{17} \text{ cm}^{-2}$, corrected for beam dilution when assuming that the extent of the emission is that of the 692 GHz H_2^{18}O observations and $T_{\text{ex}} = 124$ K. The gas-phase H_2O column density is $5.3 \times 10^{20} \text{ cm}^{-2}$ assuming the same T_{ex} as for HDO and that the isotopic abundance ratio of $^{16}\text{O}/^{18}\text{O}$ is 560 in the local interstellar medium (Wilson & Rood 1994). Assuming an uncertainty of about 20% for the column densities, originating in the flux calibration, the best estimate of the HDO/ H_2O ratio is $(9.2 \pm 2.6) \times 10^{-4}$.

Given the uncertainty in the determination of the excitation temperature, testing the effect of different temperatures is important. If the excitation temperature is as low as 80 K the HDO/ H_2O ratio becomes $7.8 \pm 2.2 \times 10^{-4}$. Increasing the excitation temperature to 300 K (Jørgensen et al. 2012) increases the ratio to $1.1 \pm 0.3 \times 10^{-3}$. The conclusions in this paper do not change over this wide interval in T_{ex} . In addition, since the 203 GHz H_2^{18}O and 225 GHz HDO observations have comparable beam and sources size, and arise from levels with similar energies, the deduced HDO/ H_2O ratio is robust. However, if the HDO emission were more extended, its column density and the HDO/ H_2O ratio would be lower. In this scenario our inferred ratio is an upper limit.

In contrast with previous estimates based on models of single-dish observations (Parise et al. 2005; Coutens et al. 2012), the deduced HDO/ H_2O ratio in the warm gas of IRAS 16293-2422 is only slightly higher than found in Earth’s oceans and by recent *Herschel* observations of comets. Given the possible systematic errors due to assumptions of the extent, they could be even closer. Within the statistical uncertainties our observed ratio for this protostar agrees with the earlier ratios for Oort cloud comets. Comparing these different ratios for water *directly* assumes that the reservoirs, i.e., comets, Earth (planet) and inner protostellar region are linked and can be related.

The difference with the earlier estimates comes from the fact that those data are sensitive to much larger scales than the high-resolution interferometric observations presented here, which directly image

the water emission on 25 – 280 AU scales. Our interferometric observations provide a strong, model independent constraint on the deuteration of water in the innermost regions of protostars. That the low HDO/H₂O ratio in the warm gas is not much different from the cometary values is an indication that significant processing of the water between these early stages and the emerging solar system is not required.

Further high-resolution interferometric measurements toward larger samples of protostars will reveal whether the warm HDO/H₂O ratio is similar in different protostars. In particular, future high angular resolution observations with ALMA will be able to resolve possible variations in the HDO/H₂O ratio with distance from the central protostar and thereby show whether the slightly different ratios measured in different types of comets potentially could be related to their spatial origin in the protostellar envelope (Robert et al. 2000).

We thank the referee, Al Wootten for insightful comments. The research at Centre for Star and Planet Formation is supported by the Danish National Research Foundation and the University of Copenhagen's programme of excellence. This research was furthermore supported by a Junior Group Leader Fellowship from the Lundbeck Foundation to JKJ. EvD acknowledges the Netherlands Organization for Scientific Research (NWO) grant 614.001.008 and EU FP7 grant 291141 CHEMPLAN. This paper makes use of the following ALMA data: ADS/JAO.ALMA#2011.0.00007.SV. The authors are grateful to JAO CSV team for planning and executing the ALMA data, and to Tim van Kempen and Markus Schmalzl of the Allegro node for help with data reduction. ALMA is a partnership of ESO (representing its member states), NSF (USA) and NINS (Japan), together with NRC (Canada) and NSC and ASIAA (Taiwan), in cooperation with the Republic of Chile. The Joint ALMA Observatory is operated by ESO, AUI/NRAO and NAOJ. The Submillimeter Array is a joint project between the Smithsonian Astrophysical Observatory and the Academia Sinica Institute of Astronomy and Astrophysics and is funded by the Smithsonian Institution and the Academia Sinica.

Line Id ^a	Species	Frequency [GHz]	Transition	Line strength [Debye ²]	E_u [K]	Beam Size (PA)	Resolution [km s ⁻¹]	RMS [b]
1	H ₂ ¹⁸ O	203.40752	3 _{1,3} – 2 _{2,0}	0.34	203.7	3.1'' × 5.0'' (-25.3°)	0.30	208
2	HDO	225.89672	3 _{1,2} – 2 _{2,1}	0.69	167.6	2.3'' × 3.9'' (15.0 °)	0.54	190
3	H ₂ ¹⁸ O	692.07914	5 _{3,2} – 4 _{4,1}	1.26	727.6	0''17 × 0''29 (109.8°)	0.40	82

^a Identifies the lines in Table 4.7.

^b mJy beam⁻¹ channel⁻¹

Table 4.8: Relevant parameters from the molecular line catalogs for the observed lines.

Paper III

The water deuterium fractionation on solar-system scales in three deeply-embedded low-mass protostars *

M. V. Persson^{1,2}, J. K. Jørgensen^{2,1}, E. F. van Dishoeck^{3,4} and D. Harsono³

¹ Centre for Star and Planet Formation, Natural History Museum of Denmark, University of Copenhagen, Øster Voldgade 5-7, DK-1350, Copenhagen K, Denmark

² Niels Bohr Institute, University of Copenhagen, Juliane Maries Vej 30, DK-2100 Copenhagen Ø, Denmark

³ Leiden Observatory, Leiden University, P.O. Box 9513, NL-2300 RA Leiden, The Netherlands

⁴ Max-Planck Institute für extraterrestrische Physik (MPE), Giessenbachstrasse, 85748 Garching, Germany

To be submitted to *Astronomy & Astrophysics*

ABSTRACT

Context Tracing the chemical evolution of water through the different stages of star formation is an important task in astronomy and astrochemistry. The water deuterium fractionation (HDO/H₂O abundance ratio) has traditionally been used to infer the amount of water that was brought to the Earth by comets. Deducing this ratio in deeply-embedded low-mass protostars has the possibility to extend the discussion of the origin of Earth's water.

Aims To measure the water deuterium fractionation in the warm gas toward the three deeply-embedded low-mass protostars NGC 1333-IRAS2A/IRAS4A-NW/IRAS4B using high-resolution interferometric observations, thus increasing the total number of sources this have been determined in to four.

Methods We present sub-arcsecond resolution observations of the 3_{1,2} – 2_{2,1} transition of HDO at 225.89672 GHz from the Plateau de Bure Interferometer in combination with previous observations of the 3_{1,3} – 2_{2,0} transition of H₂¹⁸O at 203.40752 GHz toward three low-mass protostars. The observations have similar angular resolution (0''7 - 1''3), probing scales $R \lesssim 150$ AU. A direct and model independent HDO/H₂O abundance ratio is estimated from the observations. We also run radiative transfer modeling on spherically symmetric physical models for two sources. In addition we present observations of the 2_{1,1} – 2_{1,2} transition of HDO at 241.561 GHz toward IRAS2A.

Results From the two HDO lines observed toward IRAS2A, the excitation temperature is constrained to $T_{\text{ex}} = 124 \pm 60$ K. Assuming that the excitation temperature is the same for H₂¹⁸O, the HDO/H₂O ratio for IRAS2A is $7.4 \pm 2.1 \times 10^{-4}$, for IRAS4A-NW $19.1 \pm 5.4 \times 10^{-4}$ and $5.9 \pm 1.7 \times 10^{-4}$ for IRAS4B. Changing the estimate of the excitation temperature in a reasonable range (e.g., 100 – 300 K) gives abundance ratios roughly within the estimated uncertainties. The radiative transfer modeling shows that while the HDO line at 225.9 GHz is marginally optically thick toward IRAS 16293-2422 and IRAS2A, the H₂¹⁸O line at 203 GHz is not.

Conclusions The small differences in the HDO/H₂O ratio between inner regions (where $T > 100$ K) of four young protostars and, the presumably pristine, comets in our Solar System leads to the conclusion that only little processing of water occurs between the deeply embedded stage and the formation of planetesimals and comets. The abundances derived from the radiative transfer modeling agrees with the directly estimated HDO/H₂O abundance ratio within the 3σ uncertainties. Using radiative transfer modeling to infer a HDO/H₂O ratio is only accurate within a factor of a few. This large uncertainty is only accounting for possible optical thickness and non-LTE effects. The non-spherically symmetric source structure on scales $R < 300$ AU is the biggest uncertainty, and the main conclusion is that a model independent estimate of the HDO/H₂O ratio using high-resolution interferometric observations gives a fractionation that agrees with 1D modeling within the given uncertainties.

*Based on observations carried out with the IRAM Plateau de Bure Interferometer. IRAM is supported by INSU/CNRS(France), MPG (Germany) and IGN (Spain).

4.15 Introduction

Water is a very important molecule through all stages of star and planet formation. In regions of star formation, it is an effective coolant, a significant source of oxygen and the dominant form of ice in the mantle of grains. It also aids in the sticking of grains outside the snow line, and it is crucial for the emergence and continuation of life on Earth. This makes it vital to study the chemical evolution of water during the different stages of star formation, and also to deduce the mechanism by which it was brought to Earth.

One way to gain insights into the chemical evolution of water is to compare the amount of deuterium fractionation in water (the HDO/H₂O ratio) in environments representative of different stages of star formation. In our own solar system, several measurements of the HDO/H₂O ratio⁴ exist for long-period comets from the Oort cloud (Mumma & Charnley 2011). Up until recently the mean value of the HDO/H₂O ratio for these objects was $6.4 \pm 1.0 \times 10^{-4}$ (Villanueva et al. 2009; Jehin et al. 2009), significantly above the value for Earth's oceans $3.114 \pm 0.002 \times 10^{-4}$ (VSMOW⁵, de Laeter et al. 2003, and references therein), and the protosolar nebula $0.42 \pm 0.08 \times 10^{-4}$ (Geiss & Gloeckler 1998; Lellouch et al. 2001). The 2×D/H ratio in the local interstellar medium is determined to $0.4 \pm 0.02 \times 10^{-4}$ (Prodanović et al. 2010b, and references therein). Because of this, it has been argued that only a fraction ($\leq 10\%$) of Earth's water could have its origin in comets (Morbidelli et al. 2000; Drake 2005).

Recently, the Jupiter family comet Hartley 2 was observed with the *Herschel* Space Observatory (Hartogh et al. 2011). They revealed a HDO/H₂O ratio of $3.2 \pm 0.5 \times 10^{-4}$ in this comet, significantly lower than the value for Oort cloud comets, and comparable to VSMOW. In 2012 Bockelée-Morvan et al. observed the Oort cloud comet Garradd, also with the *Herschel* Space Observatory, deducing a HDO/H₂O ratio of $4.12 \pm 0.44 \times 10^{-4}$. This is significantly lower than previous measurements of Oort cloud comets. The Jupiter family comets are short-period comets (period < 200 years) thought to originate in Kuiper belt (Mumma & Charnley 2011). Models suggest that the deuterium fractionation in the protosolar nebula increase with distance from the forming sun (Hersant et al. 2001; Kavelaars et al. 2011) – but whether the ratio is reflected in the different families of comets is thus still unclear.

Attempts at measuring the deuterium fractionation in water in protostars have resulted in differing conclusions. Parise et al. (2003) used ground-based infrared observations of the stretching bands of OH and OD in water ice in the outer parts of the envelope and found *upper limits* ranging from 0.5% to 2% for the HDO/H₂O ratios along the line of sight in four embedded low-mass protostars. In the gas-phase it is possible to detect lines of HDO, but such studies differ on the interpretation with HDO/H₂O ratios ranging from cometary values (2×10^{-4} , Stark et al. 2004), to a few $\times 10^{-2}$ (Parise et al. 2005; Liu et al. 2011). Even more recently, Coutens et al. (2012) deduced a HDO/H₂O ratio in the inner region of the low-mass protostar IRAS 16293-2422 of 3.4×10^{-2} based on analysis of many HDO and water lines. The main issue with these observations is the relatively large beam sizes from single-dish ground-based telescopes and, in particular, problems getting reliable column densities and abundances for H₂O in the gas above 100 K. In particular, Visser et al. (2013) find that the $3_{1,2} - 3_{0,3}$ lines of H₂¹⁶O and H₂¹⁸O observed by the HIFI instrument aboard the *Herschel* Space Observatory likely show optically thick emission on $R \sim 100$ AU scales in one of the well-studied, Class 0 protostars NGC1333-IRAS2A. Taking this into account Visser et al. report a revised HDO/H₂O ratio for this source of 1×10^{-3} .

Jørgensen & van Dishoeck (2010a) derived an HDO/H₂O ratio toward the Class 0 protostar NGC 1333-IRAS4B IRAS4B of $< 6.4 \times 10^{-4}$ from Submillimeter Array (SMA) and PdBI observations. Using Atacama Large Millimeter/submillimeter Array (ALMA) and SMA observations, Persson et al. (2013) estimated the HDO/H₂O ratio for the warm water toward IRAS 16293-2422 A to $9.2 \pm 2.6 \times 10^{-4}$. This value is significantly lower than previous estimates, and indicates that the deuterium fractionation in water may not be as enhanced as previously thought. In light of these results we have obtained

⁴D/H = 0.5 × HDO/H₂O

⁵Vienna Standard Mean Ocean Water

observations of HDO to complement previous data of H_2^{18}O for three sources. The observations are sensitive to scales comparable to the disk ($\sim 1''3$, $R \lesssim 160$ AU), allowing us to determine the HDO/ H_2O ratio in the innermost parts of young protostars where the disk is forming.

This paper presents observations of HDO $3_{1,2} - 2_{2,1}$ at 225.9 GHz toward three deeply-embedded low-mass protostars in the NGC 1333 region of the Perseus molecular cloud (Jennings et al. (1987); Sandell et al. (1991) — IRAS2A, IRAS4A and IRAS4B in the following) at a distance of 250 pc (Enoch et al. 2006). The three sources are ideal to compare because of their similar masses, luminosities and location (Jørgensen et al. 2006). For the same sources we have published observations of H_2^{18}O $3_{1,3} - 2_{2,0}$ at 203.4 GHz (Persson et al. 2012). With these datasets we can deduce a HDO/ H_2O ratio in the warm gas in the inner 125 AU toward three more sources, increasing the total number to four. In addition we have acquired observations of HDO $3_{1,2} - 2_{2,1}$ at 241.6 GHz toward one of the sources to constrain the excitation temperature. The paper is laid out as follow: Sect. 4.16 describes the details of the various observations. Section 4.17 and 4.18 presents the results and analysis – including intensities, column densities, spectra, maps. Line radiative transfer modeling of the observed emission is presented as well. Finally we discuss the deduced HDO/ H_2O ratio in Sect. 4.19.

4.16 Observations

Three low-mass protostars, IRAS2A, IRAS4A and IRAS4B in the embedded cluster NGC 1333 were observed using the PdBI. All sources were observed with two different receiver setups. One setup was tuned to the H_2^{18}O $3_{1,3} - 2_{2,0}$ transition at 203.40752 GHz, for details about those observations see Jørgensen & van Dishoeck (2010b) and Persson et al. (2012). In more recent observations the receivers were tuned to the HDO $3_{1,2} - 2_{2,1}$ transition at 225.89672 GHz. IRAS2A was observed in the C configuration on 27 and 28 November 2011 (8 hours; including calibration) and the B configuration on 12 March 2012 (2 hours). IRAS4A and IRAS4B were observed in track sharing mode in the B configuration on 12 March 2012 (4 hours), and C on 15, 27 and 21 March and on 2 April (3 hours). For IRAS2A the combined dataset covers baselines from 15.8 to 452.0 m (11.9 to 340.5 k λ), for IRAS4A from 15.0 to 452.0 m (11.3 to 340.5 k λ) and for IRAS4B from 16.3 to 451.9 m (12.3 to 340.5 k λ). The correlators were set up with one unit with a bandwidth of 40 MHz (47.6 km s $^{-1}$) centered on the frequency of the HDO line (225.89672 GHz), providing a spectral resolution on 460 channels of 0.087 MHz (0.104 km s $^{-1}$) width.

The data were calibrated and imaged using the CLIC and MAPPING packages, part of the IRAM GILDAS software. Regular observations of the nearby, strong quasars 0333+321, 3C84 and 2200+420 or 1749+096 were used to calibrate the complex gains and bandpass, while MWC349 and 0333+321 were observed to calibrate the absolute flux scale. During the calibration procedure integrations with significantly deviating amplitude and or phases were flagged and the continuum was subtracted before Fourier transformation of the data.

In addition to these observations, the HDO $2_{1,1} - 2_{1,2}$ line at 241.56155 GHz was observed toward IRAS2A on 7 and 17 November 2012 in the C configuration for 8 hours covering baselines from 15.5 to 175.8 m (12.5 to 141.7 k λ). The correlators were set up with one unit covering 80 MHz (89.0 km s $^{-1}$) with a spectral resolution of 0.174 MHz (0.1939 km s $^{-1}$) on 460 channels. The calibration steps and calibrator sources were otherwise the same as described above.

The resulting beam sizes using natural weighting and other parameters for the observations are given in Table 4.9. The field of view is roughly 22'' (HPBW) at 225.9 GHz and the continuum sensitivity is limited by the dynamical range of the interferometer. The uncertainty in fluxes is dominated by the accuracy of the flux calibration, typically about 20%.

Table 4.9: Parameters for the observations tuned to HDO at 225.9 GHz and 241.6 GHz.

Source	Beam ^a [$''$]	PA [$^\circ$]	RMS [$''$]
IRAS2A	1.3×1.0	23.3	16.0
IRAS2A ^c	1.2×0.9	13.3	10.5
IRAS4A	1.1×0.8	11.3	12.5
IRAS4B	1.1×0.8	10.6	10.2

(^a) Major \times minor axis. (^b) Units of mJy beam⁻¹ channel⁻¹. (^c) For the 241.6 GHz observations.

Table 4.10: Parameters of the continuum determined from elliptical Gaussian fits in the (u, v) -plane.

Source	Intensity [Jy]	PA [$^\circ$]	Size [$''$]
IRAS2A	0.4	27.5	1.1×10
IRAS2A ^a	0.5	23.7	1.3×10
IRAS4A-NW	1.7	-	2.2
IRAS4A-SE	2.1	-	1.6
IRAS4B	1.1	6.7	2.2×1.3

(^a) For the 241.6 GHz observations.

4.17 Results

After identifying line free channels the continuum was extracted and subtracted from the data to produce the spectra and subsequent data. Elliptical Gaussian fits to the (u, v) -plane of the continuum are tabulated in Table 4.10. The continuum emission from the sources agrees with previous observations (e.g., Jørgensen et al. 2007; Jørgensen & van Dishoeck 2010b; Persson et al. 2012), falling along a power-law ($F_\nu \propto \nu^\alpha$) with exponents expected from thermal dust continuum emission (i.e., $\alpha \sim 2 - 3$). This shows that the flux calibration for the different observations is accurate to within the usual uncertainties (20%).

To identify the lines, the Jet Propulsion Laboratory (JPL, Pickett et al. 1998) and the Cologne Database for Molecular Spectroscopy (CDMS, Müller et al. 2001) line-lists were queried through the Splatalogue⁶ interface. The molecular parameters for the lines are tabulated in Table 4.13. The continuum subtracted spectra of both the H₂¹⁸O 3_{1,3} – 2_{2,0} and the HDO 3_{1,2} – 2_{2,1} transition extracted toward the continuum peak for all the sources (excluding IRAS4A-SE) are shown in Figure 4.12 (H₂¹⁸O spectra from Jørgensen & van Dishoeck 2010b; Persson et al. 2012). Fig. 4.13 shows the HDO 3_{1,2} – 2_{2,1} and 2_{1,1} – 2_{1,2} for IRAS2A. All lines are detected with high signal-to-noise. In the H₂¹⁸O spectra, the lines seen besides water are due to dimethyl ether (CH₃OCH₃), for more details and information about the line assignment see Jørgensen & van Dishoeck (2010b); Persson et al. (2012). In the new HDO spectra for the 3_{1,2} – 2_{2,1} transition, at $v_{\text{lsr}} \approx 1.5$ km s⁻¹ a line from methyl formate (CH₃OCHO, $E_{\text{u}} = 36.3$ K) is seen toward IRAS4A and IRAS4B (Fig. 4.12). The targeted HDO line is strong in all the sources. Just as with the H₂¹⁸O line, no HDO is detected toward IRAS4A-SE.

⁶<http://splatalogue.net>

As noted in Jørgensen & van Dishoeck (2010b) and (Persson et al. 2012, 2013) the H_2^{18}O lines are not likely to be masing. The $3_{1,3} - 2_{2,0}$ in the main isotopologue, H_2^{16}O is masing in many sources (Cernicharo et al. 1994). In IRAS 16293-2422 the H_2^{18}O $5_{3,2} - 4_{4,1}$ line at 692.07914 GHz, observed with ALMA, was detected in absorption toward IRAS 16293-2422 B (Persson et al. 2013), which is not likely for a masing line. Furthermore, the similar line widths (for all detected lines) in the H_2^{18}O and HDO spectra presented here show that the lines do not have their origin in any outflow, where the lines are generally broader (i.e., $> 5 \text{ km s}^{-1}$ Kristensen et al. 2010).

Fig. 4.14 shows the continuum subtracted intensity maps for all three sources and water lines. For IRAS2A Fig. 4.15 shows the extra HDO line at 241.6 GHz together with the 225.9 GHz line. The intensity maps for each source are plotted on the same scale, i.e., the contour lines indicate the same intensities.

Circular Gaussian profiles were fitted to the emission of each line in the (u,v) -plane after integrating over channels corresponding to $v_{\text{lsr}} \pm \text{FWHM}$. Table 4.11 lists the FWHM of the 1D Gaussian fitted in the spectra, and the size and intensity from fits in the (u,v) -plane of the integrated intensity for all the lines. The line widths roughly agree between the lines, being slightly larger in the HDO spectra.

Source	Intensity [Jy km s ⁻¹]	FWHM [km s ⁻¹]	Size ^a [arcsec]
HDO $3_{1,2} - 2_{2,1}$			
I2A	3.98 ± 0.80	4.1 ± 0.1	$0''.4 \pm 0.1$
I4A-NW	1.97 ± 0.39	3.7 ± 0.2	$1''.6 \pm 0.1$
I4B	0.36 ± 0.07	2.5 ± 0.2	$0''.5 \pm 0.1$
HDO $2_{1,1} - 2_{1,2}$			
I2A	3.88 ± 0.78	4.0 ± 0.1	$0''.5 \pm 0.1$
H_2^{18}O $3_{1,3} - 2_{2,0}$			
I2A	0.98 ± 0.2	4.0 ± 0.2	$0''.8 \pm 0.1$
I4A-NW	0.27 ± 0.05	2.9 ± 0.3	$0''.6 \pm 0.1$
I4B	0.09 ± 0.02	0.9 ± 0.1	$0''.2 \pm 0.1$

^(a) FWHM of circular Gaussian fit in the (u,v) -plane.

Table 4.11: Results from fits to the spectra and the (u,v) -plane. The errors for the FWHM and size are from the statistical fits, while the uncertainty in intensity is assumed to be 20%.

4.18 Analysis

4.18.1 Spectra and maps

The spectra show similar characteristics for most of the observed sources. In IRAS2A, the intensities of the HDO lines are significantly larger than those of H_2^{18}O . The emission is compact and traces the warm water within 150 AU of the central sources. The integrated map for the IRAS4A protobinary shows extended emission, partly aligned with the southern, blue-shifted outflow (Jørgensen et al. 2007). The ratio between the HDO line(s) and the H_2^{18}O line is similar for IRAS2A and IRAS4B, with the intensity for HDO roughly four times stronger than that of H_2^{18}O . In IRAS4A-NW, the HDO $3_{1,2} - 2_{2,1}$

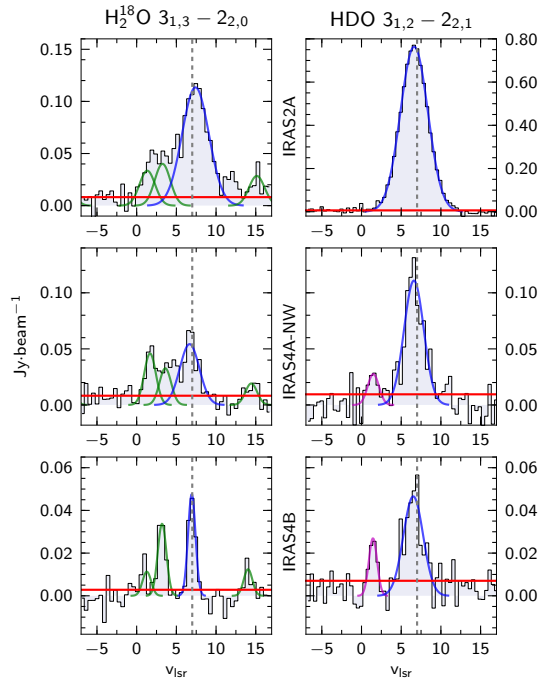


Figure 4.12: Continuum subtracted spectra of the H_2^{18}O $3_{1,3} - 2_{2,0}$ and HDO $3_{1,2} - 2_{2,1}$ lines toward the three sources NGC-1333 IRAS2A, IRAS4A-NW and IRAS4B. The H_2^{18}O spectra are from Jørgensen & van Dishoeck (2010b) and Persson et al. (2012). The green lines shows the CH_3OCH_3 , blue H_2^{18}O . In some of the HDO spectra (bottom two), a second line can be seen (magenta) at 1.5 km s^{-1} , this is from CH_3OCHO . The parental cloud velocity is shown by the dotted line ($v_{\text{lsr}} = 7 \text{ km s}^{-1}$) and the Gaussian fits (green, magenta and blue) to the lines are plotted along with the RMS (red). Note the different scales for the spectra toward IRAS2A.

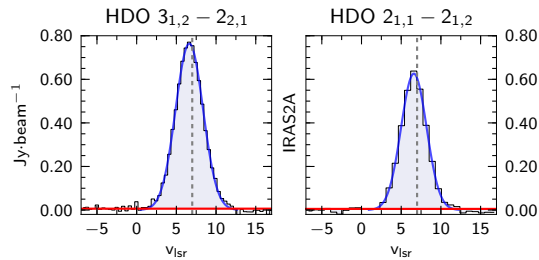


Figure 4.13: Continuum subtracted spectra of the HDO $3_{1,2} - 2_{2,1}$ and $2_{1,1} - 2_{1,2}$ lines toward IRAS2A. The parental cloud velocity is shown by the dotted line ($v_{\text{lsr}} = 7 \text{ km s}^{-1}$) and the Gaussian fits (blue) to the HDO lines are plotted along with the RMS (red).

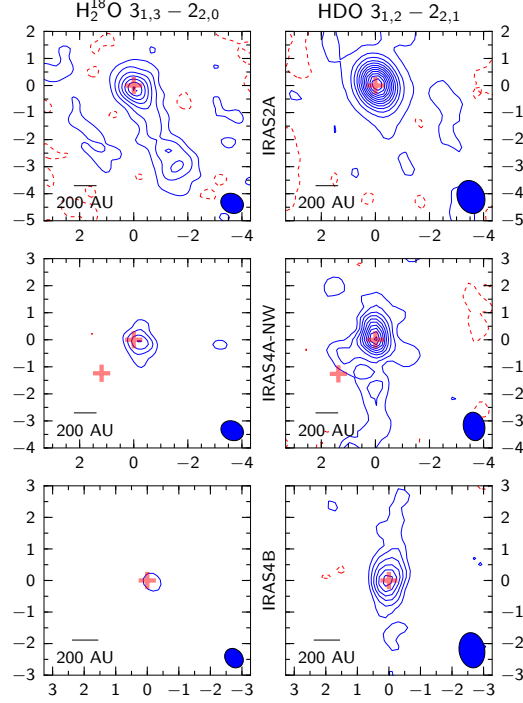


Figure 4.14: Integrated intensity maps for the HDO $3_{1,1} - 3_{3,1}$ and H_2^{18}O $3_{1,3} - 2_{2,1}$ lines calculated from channels $\pm\text{FWHM}$ from the line center. The beam is shown in the lower right corner and the red crosses show the position of continuum peaks from elliptical Gaussian fits. Units on the axes are offset in RA (x-axis) and DEC (y-axis) in arcseconds from the continuum peak. The contours start at the maximum of the 3σ level of both isotopologues. For IRAS2A this is 3×13.7 mJy with steps of 20σ (HDO) and 5σ (H_2^{18}O), 3×16.7 mJy with steps of 2σ (both) for IRAS4A, and 3×9.9 mJy with steps of 2σ for IRAS4B, dashed contours represent negative values.

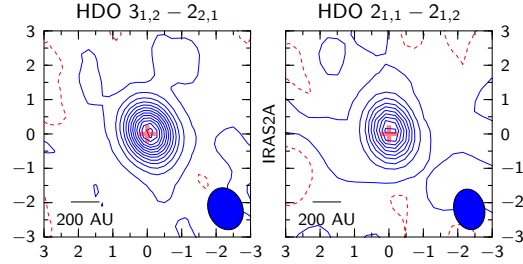


Figure 4.15: Integrated intensity maps for the $3_{1,2} - 2_{2,1}$ and $2_{1,1} - 2_{1,2}$ transition of HDO, observed toward IRAS2A, lines calculated from channels $\pm\text{FWHM}$ from the line center. The beam is shown in the lower right corner and the red crosses show the position of continuum peaks from elliptical Gaussian fits. Units on the axes are offset in arcseconds from the continuum peak. The contours start at the maximum of the 3σ level of both isotopologues (3×13.2 mJy) with steps of 20σ .

line is somewhat brighter - about seven times stronger than the H_2^{18}O line. While the methyl formate (CH_3OCHO) line is clearly seen toward IRAS4A-NW and IRAS4B in the 225 GHz spectra, it is absent in the spectrum toward IRAS2A. All lines toward IRAS4B show very compact emission.

4.18.2 Column densities, excitation temperature and the $\text{HDO}/\text{H}_2\text{O}$ ratio

With two transitions of HDO observed toward IRAS2A with different upper energy levels (E_u), a rough estimate of the excitation temperature (T_{ex}) can be made. One issue is that the energy levels are quite close (167 vs. 95 K), which increases the uncertainty of the determined excitation temperature. Assuming that the HDO is optically thin and in local thermal equilibrium (LTE), and that the emission fills the beams uniformly, the excitation temperature for HDO in IRAS2A is $T_{\text{ex}} = 124 \pm 60$ K, using 20% flux calibration uncertainty. The excitation temperature is therefore just an estimate of an average/bulk temperature of the medium observed over the entire synthesized beam. While the uncertainty in the derived temperature is large, a significant change in the excitation temperature does not affect the derived abundance ratios outside the quoted uncertainties.

Assuming that the excitation temperature for water is $T_{\text{ex}} = 124$ K, as determined for HDO in IRAS2A, in all the three sources and lines, we can estimate the column density of HDO over the observed beam. For IRAS2A this is $11.9 \pm 2.4 \times 10^{15} \text{ cm}^{-2}$, for IRAS4A-NW it is $8.8 \pm 1.8 \times 10^{15} \text{ cm}^{-2}$ and for IRAS4B $1.5 \pm 0.3 \times 10^{15} \text{ cm}^{-2}$. Assuming $T_{\text{ex}} = 124$ K for the H_2^{18}O line as well gives column densities for the three sources consistent with the results of Persson et al. (2012).

Under the assumption of LTE with $T_{\text{ex}} = 124$ K for both species, that the emission fills the beam and is optically thin, we deduced the water deuterium fractionation in all three protostars. In the calculations a $^{16}\text{O}/^{18}\text{O}$ ratio of 560 was assumed, appropriate for the local interstellar medium (Wilson & Rood 1994). For IRAS2A the $\text{HDO}/\text{H}_2\text{O}$ ratio is then $7.4 \pm 2.1 \times 10^{-4}$, for IRAS4A-NW it is $19.1 \pm 5.4 \times 10^{-4}$ and for IRAS4B it is $5.9 \pm 1.7 \times 10^{-4}$.

To investigate the effect of different excitation temperatures, Fig. 4.16 shows the $\text{HDO}/\text{H}_2\text{O}$ ratio in IRAS2A in the T_{ex} range 40 – 400 K. As can be seen in the figure, the $\text{HDO}/\text{H}_2\text{O}$ ratio does not change significantly for typical excitation temperatures: even if $T_{\text{ex}}(\text{H}_2^{18}\text{O})$ is significantly different from $T_{\text{ex}}(\text{HDO})$, the derived abundance ratios only vary by a factor of 3 from $5 - 15 \times 10^{-4}$.

4.18.3 Radiative transfer modeling

Recently, spherically symmetric physical models have been used to interpret the warm water emission lines seen in these protostars by computing the molecular excitation at each position in the envelope and subsequent line radiative transfer. The emission observed in the interferometric data is seen to originate in the inner ~ 100 AU. Previous observations have shown that spherical models break down on scales $\lesssim 300$ AU (Jørgensen et al. 2005; Chiang et al. 2012). The derived abundances in Sect. 4.18.2 assumes that the medium is in local thermodynamic equilibrium (LTE), radiative transfer modeling can test how accurate this assumption is. To assess the validity of the LTE approximation, radiative transfer models were run for the observations of IRAS 16293-2422 (Persson et al. 2013).

First the dust temperature in the envelope as function of radius is calculated self-consistently using the 1-D spherical dust continuum radiative transfer code TRANSPHERE (described in Dullemond et al. 2002). For the typical densities of the protostellar envelopes the gas is expected to be coupled to the dust and we thus assume that the gas and dust temperatures are identical (Jørgensen et al. 2002). This is then used as input to the Monte Carlo radiative transfer code RATRAN (Hogerheijde & van der Tak 2000). The runs were set up for the two protostars IRAS 16293-2422 (Persson et al. 2013) and IRAS2A. Due to the lack of complicated velocity structures in the line profiles the models only include a doppler broadening parameter (the “doppler-b parameter” $0.6 \times \text{FWHM}$). The grid is cut at an outer radius where $T_{\text{dust}} = 10$ K or $n = 10^4 \text{ cm}^{-3}$, whichever comes first. The collisional rate coefficients

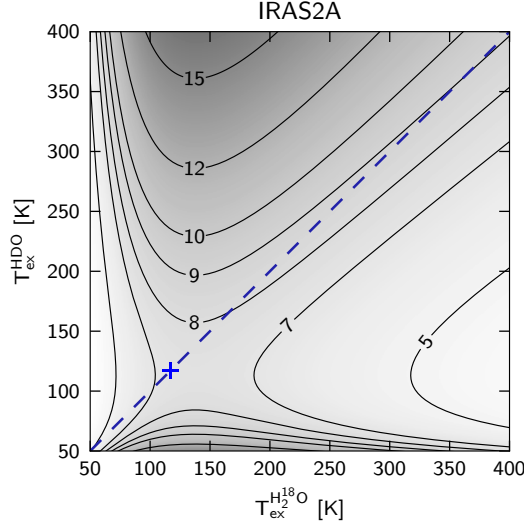


Figure 4.16: The variation of the water deuterium fractionation ($\text{HDO}/\text{H}_2\text{O}$) as a function of excitation temperature (40-400 K) for the observed water isotopologues. Values are $\times 10^{-4}$ and the dashed blue line shows where $T_{\text{ex}}^{\text{H}_2^{18}\text{O}} = T_{\text{ex}}^{\text{HDO}}$, and the cross the value determined for IRAS2A, i.e. at $T_{\text{ex}} = 124$.

used for HDO come from Faure et al. (2012) for $5 < T < 300$ K, and for H_2O from Daniel et al. (2011) for $5 < T < 1500$ K (both from the LAMDA database, Schöier et al. 2005) that were combined with the tabulated levels for H_2^{18}O at JPL (Pickett et al. 1998). The molecular abundance is assumed to follow a “jump” abundance profile (e.g., Schöier et al. 2004), with an inner and outer abundance that changes discontinuously at the point in the envelope where $T_{\text{dust}} = 100$ K, i.e., when water evaporates off the dust grains (Fraser et al. 2001). The radiative transfer modeling gives as output an model image cube with unit Jy/pixel, this was then convolved with a beam corresponding the observations and the integrated intensity compared to those observed in Table 4.11 and Persson et al. (2013).

To compare our results to Coutens et al. (2012), we adopt the same physical structure for the IRAS 16293-2422 envelope developed by Crimier et al. (2010). In the model, the envelope extends from 22 to 6100 AU. In the original model a velocity field describing infall was used, here we set the turbulence doppler-b parameter to 1 km s^{-1} . Unless the lines are strongly optically thick this will only have an effect on the line profile and not the total integrated intensity. The density structure of the envelope is described by (Shu 1977) as

$$n(r) = n(r_0) \left(\frac{r}{r_0} \right)^{-1.5} \quad r \leq r_{\text{inf}} \quad (4.18.1)$$

$$n(r) = n(r_0) \left(\frac{r}{r_0} \right)^{-2} \quad r > r_{\text{inf}} \quad (4.18.2)$$

where $r_{\text{inf}} = 1280$ AU, $r_0 = 76$ AU and $n(r_0) = 2 \times 10^8 \text{ cm}^{-3}$ (the H_2 number density at r_0 where $T_{\text{dust}} = 100$ K).

The dust opacity as a function of the frequency is set to a power-law emissivity model, i.e.,

$$\kappa = \kappa_0 \left(\frac{\nu}{\nu_0} \right)^\beta \quad (4.18.3)$$

where $\beta = 1.8$, $\kappa = 15 \text{ cm}^2 \text{ g}_{\text{dust}}^{-1}$ and $\nu_0 = 10^{12} \text{ Hz}$. The outer abundance was fixed to the best fit value of Coutens et al. (2012) of $X_{\text{out}} = 3 \times 10^{-11}$ for both HDO and H_2^{18}O . Using this model for the observations of IRAS 16293-2422 the best fit relative inner abundance to the 203 GHz H_2^{18}O line is $X_{\text{in}} = 6.9 \pm 2.8 \times 10^{-8}$ ($3.8 \pm 1.5 \times 10^{-5}$ for H_2O), and for the HDO line at 225.9 GHz $X_{\text{in}} = 8.4 \pm 2.1 \times 10^{-8}$. These abundances results in a HDO/ H_2O ratio of $2.2 \pm 1.0 \times 10^{-3}$. The modeling shows that the HDO line at 225.9 GHz is marginally optically thick whereas the H_2^{18}O line is neither masing nor optically thick for the derived abundances with this envelope physical structure and characteristic abundances. With this in mind the derived abundance ratio agrees with the previously stated LTE, optically thin value of $9.2 \pm 2.6 \times 10^{-4}$ at the factor 2–3 level (Persson et al. 2013).

4.19 Discussion and Conclusions

All deduced HDO/ H_2O ratios concur with our previous estimates for the deeply-embedded low-mass protostar IRAS 16293-2422 A (Persson et al. 2013). In IRAS4B the deduced water deuterium fractionation agrees within the uncertainties of the upper limit derived by Jørgensen & van Dishoeck (2010a), using lower sensitivity SMA data. The consistent value for all sources shows that the chemical evolution of these sources is likely to be similar.

The sources show some extended emission in HDO and or H_2^{18}O that would be included in any lower-resolution observations, e.g., single dish, however, these high-resolution observations makes it possible to focus on the compact emission. Furthermore, recent results indicate that the $3_{1,2} - 3_{0,3}$ lines of H_2^{16}O and H_2^{18}O observed with *Herschel* become optically thick, and that at different radii (Visser et al. 2013). Any HDO/ H_2O ratio deduced using *Herschel* observations are likely to be overestimated. The high-frequency lines observed with *Herschel* have significantly higher Einstein A coefficients in comparison to the H_2^{18}O $3_{1,3} - 2_{2,0}$ line studied in this study, so the results does only imply optical thickness for the specific lines. The ratio estimated for IRAS2A by Visser et al. accounting for this fact shows a water deuterium fractionation of 1×10^{-3} , in agreement with our estimates.

The modeling highlights the uncertainties involved in the derivation of the HDO/ H_2O ratio. However, the ratios deduced in the model independent way used in this paper and Persson et al. (2013) is direct, and agrees with the modeling within the uncertainties. Until the physical structure on small scales can be constrained, running radiative transfer modeling can not yield a more accurate HDO/ H_2O ratio in the warm gas in the inner region of deeply-embedded low-mass protostars.

In Fig. 4.17 the deuterium fractionation of water for all four low-mass protostars (IRAS2A, IRAS4A-NW, IRAS4B and IRAS 16293-2422) is plotted together with comets, the Earth, interstellar medium (ISM) and protosolar value. The small differences in the amount of deuteration seen toward the inner regions of protostars and the comets in our solar system suggests that only small amounts of processing of water takes place between the deeply embedded stages and the formation of comets and planetesimals.

4.20 Summary and Outlook

In this paper high-resolution interferometric observations of the HDO $3_{1,2} - 2_{2,1}$ line at 225.9 GHz toward three deeply embedded protostars have been presented. In addition, the HDO $2_{1,1} - 2_{1,2}$ line was observed toward one of the sources. With previous observations of H_2^{18}O (Persson et al. 2012), we deduced a largely model independent HDO/ H_2O ratio.

- High-resolution interferometric observations make it possible to deduce the HDO/ H_2O ratio in a model independent way with an accuracy of a factor of 2–3.
- The amount water deuterium fractionation deduced for deeply-embedded protostars using interferometric observations are consistent. The ratios are close to those observed in solar system

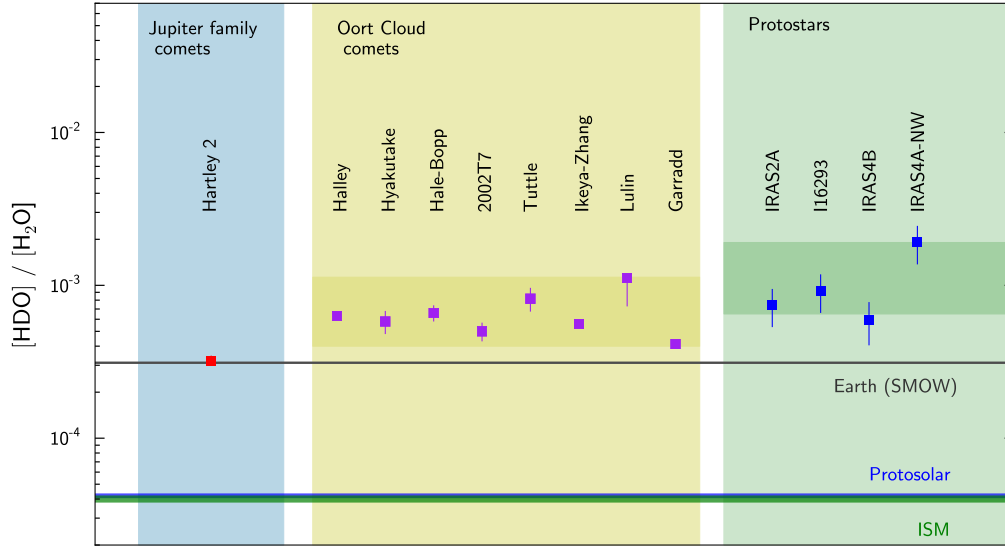


Figure 4.17: Values of the HDO/H₂O ratio, for different objects. For references, see Table 4.12. For ISM, 2×D/H is plotted.

comets. The small difference between these reservoirs indicates little processing of material between the deeply-embedded, collapsing stage and the formation of comets/planetesimals.

The current physical models assuming spherical symmetry are not representative of the structure on scales of a few hundred AUs. Future high-resolution observations have the possibility to shed light on this, and trace the origin of the warm water emission lines presented here. Another question that future observations may be able to answer is the radial dependence of the D/H ratio. Chemical models of isotopic exchange with H₂ of turbulent nebulae show a strong radial dependence of the D/H ratio (Hersant et al. 2001; Kavelaars et al. 2011).

The time scales for the early, deeply-embedded stages are too short for any chemical processing of water to take place, therefore the gaseous water observed originates in ice formed earlier in the evolution. The D/H ratios for different molecules change as the protostar evolves beyond these early stages (e.g., Aikawa et al. 2012). New high-resolution interferometric observations have the potential to derive abundances for the inner regions of more evolved sources and constrain the time dependent chemical models.

We wish to thank the IRAM staff, in particular Arancha Castro-Carrizo and Chin Shin Chang, for their help with the observations and reduction of the data. IRAM is supported by INSU/CNRS(France), MPG (Germany) and IGN (Spain). The research at Centre for Star and Planet Formation is supported by the Danish National Research Foundation and the University of Copenhagen's programme of excellence. This research was furthermore supported by a Junior Group Leader Fellowship from the Lundbeck Foundation to J.K.J. EvD acknowledges the Netherlands Organization for Scientific Research (NWO) grant 614.001.008 and EU FP7 grant 291141 CHEMPLAN. This work has benefited from research funding from the European Community's sixth Framework Programme under RadioNet R113CT 2003 5058187.

4.21 Tables

Type	Object	Origin	HDO/H ₂ O [$\times 10^{-4}$]	Tracers (Proxy)	Ref.
Comet	1/P Halley	(OCC)	6.3 ± 0.7	H ₂ O, H ₃ O ⁺ ^a	1
Comet	C/1996 B2 Hyakutake	(OCC)	5.8 ± 2.0	H ₂ O, HDO	2
Comet	C/1995 O1 Hale-Bopp	(OCC)	6.6 ± 1.6	HDO, OH	3
Comet	8P/Tuttle	(OCC)	8.2 ± 2.9	H ₂ O, HDO	4
Comet	C/2007 N3 Lulin	(OCC)	< 11.2	H ₂ , HDO	5
Comet	C/2002 T7 LINEAR	(OCC)	5 ± 1.4^b	OH, OD	6
Comet	153P Ikeya-Zhang	(OCC)	$< 5.6 \pm 0.6$	H ₂ O, H ₂ ¹⁸ O, HDO	7
Comet	C/2009 P1 Garradd	(OCC)	2.06 ± 0.22	H ₂ ¹⁸ O, H ₂ O, HDO	8
	OCC Mean ^c		6.4 ± 1.0		
Comet	103P Hartley 2	(JFC)	3.2 ± 0.5	H ₂ ¹⁸ O, HDO	9
Planet	Earth (SMOW)		3.114 ± 0.002		10
	Protosolar		0.42 ± 0.08^c	³ He, ⁴ He	11
	(L)ISM ^d		$\geq 0.40 \pm 0.02$	H, D	12
Protostar	IRAS 16293-2422	< 50 AU	9.2 ± 2.6	H ₂ ¹⁸ O, HDO	13
Protostar			340	H ₂ ¹⁸ O, HDO	14
Protostar			300	H ₂ O, HDO	15
Protostar	NGC 1333-IRAS2A	$\lesssim 300$ AU	7.4 ± 2.1	H ₂ ¹⁸ O, HDO	16
Protostar			≥ 100	H ₂ ¹⁸ O, HDO	17
Protostar	NGC 1333-IRAS4A-NW	$\lesssim 300$ AU	19.1 ± 5.4	H ₂ ¹⁸ O, HDO	16
Protostar	NGC 1333-IRAS4B	$\lesssim 300$ AU	5.9 ± 1.7	H ₂ ¹⁸ O, HDO	16
Protostar			< 6.4	H ₂ ¹⁸ O, HDO	18

(^a) H_x^yO with $x = 2, 3$, and $y = 16, 17, 18$ and also HD^yO was measured (^b) Value is $2 \times D/H$. (^c) No upper limits included (^d) Local Interstellar Medium, i.e. $\sim 1 - 2$ kpc from the Sun

(**1**) Eberhardt et al. (1995); (**2**) Bockelee-Morvan et al. (1998); (**3**) Meier et al. (1998); (**4**) Villanueva et al. (2009); (**5**) Gibb et al. (2012); (**6**) Hutsemékers et al. (2008); (**7**) Biver et al. (2006); (**8**) Bockelee-Morvan et al. (2012); (**9**) Hartogh et al. (2011); (**10**) de Laeter et al. (2003, and ref. therein); (**11**) Geiss & Gloeckler (1998); Lellouch et al. (2001); (**12**) Prodanović et al. (2010b, and ref. therein); (**13**) Persson et al. (2013); (**14**) Coutens et al. (2012); (**15**) Parise et al. (2005); (**16**) This work; (**17**) Liu et al. (2011); (**18**) Jørgensen & van Dishoeck (2010a)

Table 4.12: The HDO/H₂O abundance ratios for different objects. OCC - Oort Cloud Comet, JFC - Jupiter Family Comet. Note that some values are $2 \times$ the D/H ratio and that the ratio in protostars refers to the warm gas in the inner regions.

Molecule	Transition	Rest Freq. [GHz]	E_u [K]	Strength [$\log_{10} A_{ul}$]
H_2^{18}O	$3_{1,3} - 2_{2,0}$	203.40752	203.7	-5.3177
HDO	$3_{1,2} - 2_{2,1}$	225.89672	167.6	-4.8799
HDO	$2_{1,1} - 2_{1,2}$	241.56155	95.2	-4.9256

Table 4.13: Molecular data for the different lines, from JPL (Pickett et al. 1998) and CDMS (Müller et al. 2001).

Bibliography

- Aikawa, Y., Wakelam, V., Hersant, F., Garrod, R. T., & Herbst, E. 2012, *ApJ*, 760, 40
- Alves, F. O., Vlemmings, W. H. T., Girart, J. M., & Torrelles, J. M. 2012, *A&A*, 542, A14
- Arce, H. G., Santiago-García, J., Jørgensen, J. K., Tafalla, M., & Bachiller, R. 2008, *ApJ*, 681, L21
- Arce, H. G., Shepherd, D., Gueth, F., et al. 2007, *Protostars and Planets V*, 245
- Arzoumanian, D., André, P., Didelon, P., et al. 2011, *A&A*, 529, L6
- Attard, M., Houde, M., Novak, G., et al. 2009, *ApJ*, 702, 1584
- Bachiller, R. & Perez Gutierrez, M. 1997, *ApJ*, 487, L93
- Bate, M. R. 1998, *ApJ*, 508, L95
- Bate, M. R. 2010, *MNRAS*, 404, L79
- Beckwith, S. V. W. & Sargent, A. I. 1991, *ApJ*, 381, 250
- Bergin, E. A., Kaufman, M. J., Melnick, G. J., Snell, R. L., & Howe, J. E. 2003, *ApJ*, 582, 830
- Bergin, E. A., Melnick, G. J., Stauffer, J. R., et al. 2000, *ApJ*, 539, L129
- Bergin, E. A. & Snell, R. L. 2002, *ApJ*, 581, L105
- Bisschop, S. E., Jørgensen, J. K., Bourke, T. L., Bottinelli, S., & van Dishoeck, E. F. 2008, *A&A*, 488, 959
- Biver, N., Bockelée-Morvan, D., Crovisier, J., et al. 2006, *A&A*, 449, 1255
- Bjerkeli, P., Liseau, R., Olberg, M., et al. 2009, *A&A*, 507, 1455
- Blake, G. A., Sandell, G., van Dishoeck, E. F., et al. 1995, *ApJ*, 441, 689
- Blake, G. A., van Dishoeck, E. F., Jansen, D. J., Groesbeck, T. D., & Mundy, L. G. 1994, *ApJ*, 428, 680
- Bockelée-Morvan, D., Biver, N., Swinyard, B., et al. 2012, *A&A*, 544, L15
- Bockelée-Morvan, D., Gautier, D., Lis, D. C., et al. 1998, *Icarus*, 133, 147
- Boogert, A. C. A., Pontoppidan, K. M., Knez, C., et al. 2008, *ApJ*, 678, 985
- Bottinelli, S., Ceccarelli, C., Lefloch, B., et al. 2004a, *ApJ*, 615, 354
- Bottinelli, S., Ceccarelli, C., Neri, R., et al. 2004b, *ApJ*, 617, L69
- Bottinelli, S., Ceccarelli, C., Williams, J. P., & Lefloch, B. 2007, *A&A*, 463, 601
- Brinch, C., Jørgensen, J. K., & Hogerheijde, M. R. 2009, *A&A*, 502, 199
- Butner, H. M., Charnley, S. B., Ceccarelli, C., et al. 2007, *ApJ*, 659, L137
- Caselli, P. & Ceccarelli, C. 2012, *A&A Rev.*, 20, 56
- Caselli, P., Hasegawa, T. I., & Herbst, E. 1993, *ApJ*, 408, 548
- Caselli, P., Keto, E., Bergin, E. A., et al. 2012, *ApJ*, 759, L37
- Caux, E., Kahane, C., Castets, A., et al. 2011, *A&A*, 532, A23
- Cazaux, S., Caselli, P., & Spaans, M. 2011, *ApJ*, 741, L34
- Cazaux, S., Tielens, A. G. G. M., Ceccarelli, C., et al. 2003, *ApJ*, 593, L51
- Ceccarelli, C., Caux, E., Loinard, L., et al. 1999, *A&A*, 342, L21
- Ceccarelli, C., Caux, E., White, G. J., et al. 1998, *A&A*, 331, 372
- Ceccarelli, C., Hollenbach, D. J., & Tielens, A. G. G. M. 1996, *ApJ*, 471, 400
- Cernicharo, J., Gonzalez-Alfonso, E., Alcolea, J., Bachiller, R., & John, D. 1994, *ApJ*, 432, L59
- Chandler, C. J., Brogan, C. L., Shirley, Y. L., & Loinard, L. 2005, *ApJ*, 632, 371
- Charnley, S. B. 1997, *ApJ*, 481, 396
- Charnley, S. B., Tielens, A. G. G. M., & Millar, T. J. 1992, *ApJ*, 399, L71
- Cheung, A. C., Rank, D. M., Townes, C. H., Thornton, D. D., & Welch, W. J. 1969, *Nature*, 221, 626
- Chiang, H.-F., Looney, L. W., Tassis, K., Mundy, L. G., & Mouschovias, T. C. 2008, *ApJ*, 680, 474

- Chiang, H.-F., Looney, L. W., & Tobin, J. J. 2012, *ApJ*, 756, 168
- Choi, M., Kang, M., Byun, D.-Y., & Lee, J.-E. 2012, *ApJ*, 759, 136
- Choi, M., Tatematsu, K., & Kang, M. 2010, *ApJ*, 723, L34
- Coutens, A., Vastel, C., Caux, E., et al. 2012, *A&A*, 539, A132
- Crimier, N., Ceccarelli, C., Maret, S., et al. 2010, *A&A*, 519, A65
- D'Alessio, P., Calvet, N., & Hartmann, L. 2001, *ApJ*, 553, 321
- D'Alessio, P., Calvet, N., Hartmann, L., Lizano, S., & Cantó, J. 1999, *ApJ*, 527, 893
- Dalgarno, A. & Black, J. H. 1976, *Reports on Progress in Physics*, 39, 573
- Daniel, F., Dubernet, M.-L., & Grosjean, A. 2011, *A&A*, 536, A76
- de Jong, T., Boland, W., & Dalgarno, A. 1980, *A&A*, 91, 68
- de Laeter, J. R., Böhlke, J. K., De Bièvre, P., et al. 2003, *Pure and Applied Chemistry*, 75, 683
- Delsemme, A. H. 1992, *Advances in Space Research*, 12, 5
- Delsemme, A. H. 1998, *Planet. Space Sci.*, 47, 125
- Desmurs, J. F., Codella, C., Santiago-García, J., Tafalla, M., & Bachiller, R. 2006, *Proceedings of the 8th European VLBI Network Symposium*. September 26-29
- Desmurs, J.-F., Codella, C., Santiago-García, J., Tafalla, M., & Bachiller, R. 2009, *A&A*, 498, 753
- Di Francesco, J., Myers, P. C., Wilner, D. J., Ohashi, N., & Mardones, D. 2001, *ApJ*, 562, 770
- Draine, B. T., Roberge, W. G., & Dalgarno, A. 1983, *ApJ*, 264, 485
- Drake, M. J. 2005, *Meteoritics and Planetary Science*, 40, 519
- Dullemond, C. P., van Zadelhoff, G. J., & Natta, A. 2002, *A&A*, 389, 464
- Eberhardt, P., Reber, M., Krankowsky, D., & Hodges, R. R. 1995, *A&A*, 302, 301
- Elitzur, M., ed. 1992, *Astrophysics and Space Science Library*, Vol. 170, Astronomical masers
- Elitzur, M. 1998, *ApJ*, 504, 390
- Enoch, M. L., Young, K. E., Glenn, J., et al. 2006, *ApJ*, 638, 293
- Evans, N. J., Dunham, M. M., Jørgensen, J. K., et al. 2009, *ApJ Suppl.*, 181, 321
- Faure, A., Wiesenfeld, L., Scribano, Y., & Ceccarelli, C. 2012, *MNRAS*, 420, 699
- Felli, M., Brand, J., Cesaroni, R., et al. 2007, *A&A*, 476, 373
- Franklin, J., Snell, R. L., Kaufman, M. J., et al. 2008, *ApJ*, 674, 1015
- Fraser, H. J., Collings, M. P., McCoustra, M. R. S., & Williams, D. A. 2001, *MNRAS*, 327, 1165
- Furuya, R. S., Kitamura, Y., Wootten, A., Claussen, M. J., & Kawabe, R. 2003, *ApJ Suppl.*, 144, 71
- Garrod, R. T. & Herbst, E. 2006, *A&A*, 457, 927
- Geiss, J. & Gloeckler, G. 1998, *Space Sci. Rev.*, 84, 239
- Gensheimer, P. D., Mauersberger, R., & Wilson, T. L. 1996, *A&A*, 314, 281
- Gibb, E. L., Bonev, B. P., Villanueva, G., et al. 2012, *ApJ*, 750, 102
- Gibb, E. L., Whittet, D. C. B., Boogert, A. C. A., & Tielens, A. G. G. M. 2004, *ApJ Suppl.*, 151, 35
- Girart, J. M., Rao, R., & Marrone, D. P. 2006, *Science*, 313, 812
- Gutermuth, R. A., Myers, P. C., Megeath, S. T., et al. 2008, *ApJ*, 674, 336
- Haro, G. 1952, *ApJ*, 115, 572
- Hartigan, P., Edwards, S., & Ghandour, L. 1995, *ApJ*, 452, 736
- Hartmann, L. & Kenyon, S. J. 1996, *ARA&A*, 34, 207
- Hartogh, P., Lis, D. C., Bockelée-Morvan, D., et al. 2011, *Nature*, 478, 218
- Harwit, M., Neufeld, D. A., Melnick, G. J., & Kaufman, M. J. 1998, *ApJ*, 497, L105
- Herbig, G. H. 1951, *ApJ*, 113, 697
- Herbst, E. & Klemperer, W. 1973, *ApJ*, 185, 505
- Herbst, E. & van Dishoeck, E. F. 2009, *ARA&A*, 47, 427
- Herczeg, G. J., Karska, A., Bruderer, S., et al. 2012, *A&A*, 540, A84
- Hersant, F., Gautier, D., & Huré, J.-M. 2001, *ApJ*, 554, 391
- Högbom, J. A. 1974, *A&AS*, 15, 417
- Hogerheijde, M. R., Bergin, E. A., Brinch, C., et al. 2011, *Science*, 334, 338
- Hogerheijde, M. R. & van der Tak, F. F. S. 2000, *A&A*, 362, 697
- Hollenbach, D., Kaufman, M. J., Bergin, E. A., & Melnick, G. J. 2009, *ApJ*, 690, 1497
- Hutsemékers, D., Manfroid, J., Jehin, E., Zucconi,

- J.-M., & Arpigny, C. 2008, *A&A*, 490, L31
- Ioppolo, S., Cuppen, H. M., Romanzin, C., van Dishoeck, E. F., & Linnartz, H. 2008, *ApJ*, 686, 1474
- Ioppolo, S., Cuppen, H. M., Romanzin, C., van Dishoeck, E. F., & Linnartz, H. 2010, *Physical Chemistry Chemical Physics (Incorporating Faraday Transactions)*, 12, 12065
- Jacq, T., Henkel, C., Walmsley, C. M., Jewell, P. R., & Baudry, A. 1988, *A&A*, 199, L5
- Jehin, E., Manfroid, J., Hutsemékers, D., Arpigny, C., & Zucconi, J.-M. 2009, *Earth Moon and Planets*, 105, 167
- Jennings, R. E., Cameron, D. H. M., Cudlip, W., & Hirst, C. J. 1987, *MNRAS*, 226, 461
- Jørgensen, J. K., Bourke, T. L., Myers, P. C., et al. 2007, *ApJ*, 659, 479
- Jørgensen, J. K., Bourke, T. L., Myers, P. C., et al. 2005, *ApJ*, 632, 973
- Jørgensen, J. K., Bourke, T. L., Nguyen Luong, Q., & Takakuwa, S. 2011, *A&A*, 534, A100
- Jørgensen, J. K., Favre, C., Bisschop, S. E., et al. 2012, *ApJ*, 757, L4
- Jørgensen, J. K., Harvey, P. M., Evans, II, N. J., et al. 2006, *ApJ*, 645, 1246
- Jørgensen, J. K., Hogerheijde, M. R., van Dishoeck, E. F., Blake, G. A., & Schöier, F. L. 2004, *A&A*, 413, 993
- Jørgensen, J. K., Schöier, F. L., & van Dishoeck, E. F. 2002, *A&A*, 389, 908
- Jørgensen, J. K. & van Dishoeck, E. F. 2010a, *ApJ*, 725, L172
- Jørgensen, J. K. & van Dishoeck, E. F. 2010b, *ApJ*, 710, L72
- Jørgensen, J. K., van Dishoeck, E. F., Visser, R., et al. 2009, *A&A*, 507, 861
- Kavelaars, J. J., Mousis, O., Petit, J.-M., & Weaver, H. A. 2011, *ApJ*, 734, L30
- Kessler, M. F., Steinz, J. A., Anderegg, M. E., et al. 1996, *A&A*, 315, L27
- Knude, J. & Hog, E. 1998, *A&A*, 338, 897
- Kristensen, L. E., van Dishoeck, E. F., Bergin, E. A., et al. 2012, *A&A*, 542, A8
- Kristensen, L. E., Visser, R., van Dishoeck, E. F., et al. 2010, *A&A*, 521, L30
- Kuan, Y.-J., Huang, H.-C., Charnley, S. B., et al. 2004, *ApJ*, 616, L27
- Larson, R. B. 1969, *MNRAS*, 145, 271
- Larson, R. B. 1972, *MNRAS*, 157, 121
- Lécuyer, C., Gillet, P., & Robert, F. 1998, *Chemical Geology*, 145, 249
- Lellouch, E., Bézard, B., Fouchet, T., et al. 2001, *A&A*, 370, 610
- Linsky, J. L. 2003, *Space Sci. Rev.*, 106, 49
- Liseau, R., Ceccarelli, C., Larsson, B., et al. 1996, *A&A*
- Liseau, R., Sandell, G., & Knee, L. B. G. 1988, *A&A*, 192, 153
- Liu, F.-C., Parise, B., Kristensen, L., et al. 2011, *A&A*, 527, A19
- Loinard, L., Torres, R. M., Mioduszewski, A. J., & Rodríguez, L. F. 2008, *ApJ*, 675, L29
- Loinard, L., Zapata, L. A., Rodríguez, L. F., et al. 2013, *MNRAS*, 430, L10
- Looney, L. W., Mundy, L. G., & Welch, W. J. 2000, *ApJ*, 529, 477
- Machida, M. N., Inutsuka, S.-i., & Matsumoto, T. 2010, *ApJ*, 724, 1006
- Maret, S., Ceccarelli, C., Caux, E., Tielens, A. G. G. M., & Castets, A. 2002, *A&A*, 395, 573
- Marvel, K. B., Wilking, B. A., Claussen, M. J., & Wootten, A. 2008, *ApJ*, 685, 285
- McMullin, J. P., Waters, B., Schiebel, D., Young, W., & Golap, K. 2007, in *Astronomical Society of the Pacific Conference Series*, Vol. 376, *Astronomical Data Analysis Software and Systems XVI*, ed. R. A. Shaw, F. Hill, & D. J. Bell, 127
- Meier, R., Owen, T. C., Matthews, H. E., et al. 1998, *Science*, 279, 842
- Melnick, G. J., Stauffer, J. R., Ashby, M. L. N., et al. 2000, *ApJ*, 539, L77
- Miyake, K. & Nakagawa, Y. 1993, *Icarus*, 106, 20
- Morbidelli, A., Chambers, J., Lunine, J. I., et al. 2000, *Meteoritics and Planetary Science*, 35, 1309
- Müller, H. S. P., Thorwirth, S., Roth, D. A., & Winnewisser, G. 2001, *A&A*, 370, L49
- Mumma, M. J. & Charnley, S. B. 2011, *ARA&A*, 49, 471
- Neufeld, D. A. & Kaufman, M. J. 1993, *ApJ*, 418, 263
- Nisini, B. 2003, *Ap&SS*, 287, 207
- Nisini, B., Benedettini, M., Codella, C., et al. 2010, *A&A*, 518, L120
- Nisini, B., Benedettini, M., Giannini, T., et al. 1999, *A&A*, 350, 529
- Nordh, H. L., von Schéele, F., Frisk, U., et al. 2003, *A&A*, 402, L21
- Osterbrock, D. E. 1989, *Astrophysics of gaseous nebulae and active galactic nuclei*

- Parise, B., Caux, E., Castets, A., et al. 2005, *A&A*, 431, 547
- Parise, B., Simon, T., Caux, E., et al. 2003, *A&A*, 410, 897
- Peretto, N., André, P., Könyves, V., et al. 2012, *A&A*, 541, A63
- Persson, C. M., Olofsson, A. O. H., Koning, N., et al. 2007, *A&A*, 476, 807
- Persson, M. V., Jørgensen, J. K., & van Dishoeck, E. F. 2012, *A&A*, 541, A39
- Persson, M. V., Jørgensen, J. K., & van Dishoeck, E. F. 2013, *A&A*, 549, L3
- Pickett, H. M., Poynter, R. L., Cohen, E. A., et al. 1998, *JQSRT*, 60, 883
- Pineda, J. E., Maury, A. J., Fuller, G. A., et al. 2012, *A&A*, 544, L7
- Pontoppidan, K. M., van Dishoeck, E. F., & Dartois, E. 2004, *A&A*, 426, 925
- Prodanović, T., Steigman, G., & Fields, B. D. 2010a, *MNRAS*, 406, 1108
- Prodanović, T., Steigman, G., & Fields, B. D. 2010b, *MNRAS*, 406, 1108
- Przybilla, N., Nieva, M.-F., & Butler, K. 2008, *ApJ*, 688, L103
- Qi, C. 2008, *The MIR Cookbook, The Submillimeter Array, Harvard-Smithsonian Center* (<http://cfa-www.harvard.edu/~cqi/mircook.html>)
- Reipurth, B., Rodríguez, L. F., Anglada, G., & Bally, J. 2002, *AJ*, 124, 1045
- Robert, F., Gautier, D., & Dubrulle, B. 2000, *Space Sci. Rev.*, 92, 201
- Roberts, H., Herbst, E., & Millar, T. J. 2003, *ApJ*, 591, L41
- Rodgers, S. D. & Charnley, S. B. 2001, *ApJ*, 546, 324
- Rybicki, G. B. & Lightman, A. P. 2004, *Radiative Processes in Astrophysics* (Wiley-VCH), 400
- Sandell, G., Aspin, C., Duncan, W. D., Russell, A. P. G., & Robson, E. I. 1991, *ApJ*, 376, L17
- Sandell, G., Knee, L. B. G., Aspin, C., Robson, I. E., & Russell, A. P. G. 1994, *A&A*, 285, L1
- Sault, R. J., Teuben, P. J., & Wright, M. C. H. 1995, in *Astronomical Society of the Pacific Conference Series, Vol. 77, Astronomical Data Analysis Software and Systems IV*, ed. R. A. Shaw, H. E. Payne, & J. J. E. Hayes, 433
- Schöier, F. L., Jørgensen, J. K., van Dishoeck, E. F., & Blake, G. A. 2004, *A&A*, 418, 185
- Schöier, F. L., van der Tak, F. F. S., van Dishoeck, E. F., & Black, J. H. 2005, *A&A*, 432, 369
- Shakura, N. I. & Sunyaev, R. A. 1973, *A&A*, 24, 337
- Shu, F. H. 1977, *ApJ*, 214, 488
- Shu, F. H., Adams, F. C., & Lizano, S. 1987, *ARA&A*, 25, 23
- Sobolev, V. V. 1960, *Moving envelopes of stars*
- Stark, R., Sandell, G., Beck, S. C., et al. 2004, *ApJ*, 608, 341
- Szymczak, M., Pillai, T., & Menten, K. M. 2005, *A&A*, 434, 613
- Tafalla, M., Liseau, R., Nisini, B., et al. 2013, *A&A*, 551, A116
- Tafalla, M., Santiago, J., Johnstone, D., & Bachiller, R. 2004, *A&A*, 423, L21
- Taquet, V., Peters, P. S., Kahane, C., et al. 2013, *A&A*, 550, A127
- Terebey, S., Shu, F. H., & Cassen, P. 1984, *ApJ*, 286, 529
- Tielens, A. G. G. M. & Hagen, W. 1982, *A&A*, 114, 245
- Tobin, J. J., Hartmann, L., Looney, L. W., & Chiang, H.-F. 2010, *ApJ*, 712, 1010
- Tomida, K., Tomisaka, K., Matsumoto, T., et al. 2013, *ApJ*, 763, 6
- Ulrich Käuff, H. 2008, in *Precision Spectroscopy in Astrophysics*, ed. N. Santos, L. Pasquini, A. Correia, & M. Romaniello, *ESO Astrophysics Symposia* (Springer Berlin Heidelberg), 227–230
- van der Tak, F. F. S., Black, J. H., Schöier, F. L., Jansen, D. J., & van Dishoeck, E. F. 2007, *A&A*, 468, 627
- van der Tak, F. F. S., Walmsley, C. M., Herpin, F., & Ceccarelli, C. 2006, *A&A*, 447, 1011
- van Dishoeck, E. F. & Blake, G. A. 1998, *ARA&A*, 36, 317
- van Dishoeck, E. F., Blake, G. A., Jansen, D. J., & Groesbeck, T. D. 1995, *ApJ*, 447, 760
- van Dishoeck, E. F., Kristensen, L. E., Benz, A. O., et al. 2011, *PASP*, 123, 138
- Villanueva, G. L., Mumma, M. J., Bonev, B. P., et al. 2009, *ApJ*, 690, L5
- Visser, R., Doty, S. D., & van Dishoeck, E. F. 2011, *A&A*, 534, A132
- Visser, R., Jørgensen, J. K., Kristensen, L. E., van Dishoeck, E. F., & Bergin, E. A. 2013, "Accepted for publication by *A&A*"
- Visser, R., van Dishoeck, E. F., Doty, S. D., & Dullemond, C. P. 2009, *A&A*, 495, 881
- Wakelam, V., Ceccarelli, C., Castets, A., et al.

- 2005, *A&A*, 437, 149
- Watson, D. M., Bohac, C. J., Hull, C., et al. 2007, *Nature*, 448, 1026
- Whittet, D. C. B. 1993, *Observations of Molecular Ices*, ed. T. J. Millar & D. A. Williams, 9
- Whittet, D. C. B., ed. 2003, *Dust in the galactic environment* (Institute of Physics (IOP) Publishing)
- Williams, J. P. & Cieza, L. A. 2011, *ARA&A*, 49, 67
- Wilson, T. L. & Rood, R. 1994, *ARA&A*, 32, 191
- Woodall, J., Agúndez, M., Markwick-Kemper, A. J., & Millar, T. J. 2007, *A&A*, 466, 1197

